Surface and Interface Electronic Structure in Ferroelectric $BaTiO_3$

Dissertation

zur Erlangung des naturwissenschaftlichen Doktorgrades der Julius-Maximilians-Universität Würzburg

vorgelegt von

Peter Lutz

aus Neumarkt i.d.Opf.

Würzburg 2017

Eingereicht am: 31.08.2017
bei der Fakultät für Physik und Astronomie

1. Gutachter: Prof. Dr. Friedrich Reinert
2. Gutachter: Prof. Dr. Vladimir Hinkov
der Dissertation

Vorsitzende(r): Prof. Dr. Matthias Bode
1. Prüfer: Prof. Dr. Friedrich Reinert
2. Prüfer: Prof. Dr. Vladimir Hinkov
3. Prüfer: PD Dr. Martin Greiter
im Promotionskolloquium

Tag des Promotionskolloquiums: 09.03.2018

Doktorurkunde ausgehändigt am: .....

"Pay attention
to where you are going
because without meaning
you might get nowhere."

A. A. Milne

ZUSAMMENFASSUNG

Übergangsmetalloxide stellen eine hochinteressante Materialklasse dar, da sie eine Vielzahl neuartiger Phänomene, wie z.B. multiferroische Eigenschaften und Supraleitung, aufweisen. Diese Effekte sind die Folge eines komplexen Zusammenspiels zwischen den Freiheitsgraden von Ladung, Spin und der orbitalen Komponente innerhalb eines korrelierten d-Elektronensystems. Sauerstoffstörstellen an der Oberfläche von einigen dieser Systeme führen zu der Ausbildung freier Ladungsträger und der damit verbundenen Erzeugung eines 2-dimensionalen Elektronengases (2DEG). Das in dieser Arbeit untersuchte Bariumtitanat ($BaTiO_3$) ist ein typisches und sehr vielversprechendes d^0-Übergangsmetalloxid. Zum einen ist es ferroelektrisch bei Raumtemperatur und zum anderen weist es mehrere strukturelle Phasenübergänge auf, von kubisch über tetragonal (bei Raumtemperatur) und orthorhombisch zu rhomboedrisch. Die spontane elektrische Polarisation in $BaTiO_3$ kann dazu verwendet werden um physikalische Eigenschaften angrenzender Materialsysteme, z.B. von Dünnfilmen, zu beeinflussen. Obwohl vor allem die makroskopischen ferroelektrischen Eigenschaften von $BaTiO_3$ bereits detailliert untersucht wurden, ist die mikroskopische elektronische Struktur in $BaTiO_3$ und in $BaTiO_3$-Grenzflächen noch nicht vollständig verstanden. Der Grund hierfür ist ein komplexes Wechselspiel zwischen elektronischen Korrelationseffekten, Sauerstoffstörstellen, Ferroelektrizität und strukturellen Aspekten.

Diese Dissertation befasst sich mit der elektronischen Struktur von verschiedenen $BaTiO_3$-Systemen, unter Verwendung der winkelaufgelösten Photoelektronenspektroskopie (PES). Zum einen wurde das Valenzband von $BaTiO_3$-Einkristallen systematisch untersucht und mit theoretischen Rechnungen verglichen. Dabei konnte eine endliche p-d-Hybridisierung von Titan- mit Sauerstoff-Zuständen im Valenzband festgestellt werden. Weiterhin wurde in $BaTiO_3$-Dünnfilmen das Auftreten von spektralem Gewicht nahe des Ferminiveaus beobachtet. Diese metallischen Zustände sind auf eine erhöhte Dichte von Sauerstoffstörstellen an der Oberfläche zurückzuführen, wodurch das System effektiv dotiert wird. Die systematische Untersuchung der elektronischen Struktur in Abhängigkeit von Temperatur und Sauerstoff-Partialdruck wurde erfolgreich durch ein Modell beschrieben, das eine Instabilität der metallischen Zustände bei $T \approx 285\,\mathrm{K}$ aufzeigt.

Die ferroelektrische Eigenschaft von $BaTiO_3$ kann in Heterostrukturen dazu verwendet werden, um die elektronische Struktur an der Grenzfläche zu kontrollieren. Zu diesem Zweck wurde in dieser Arbeit die mikroskopische elektronische Struktur an der Grenzfläche von Bi/$BaTiO_3$ bedeckungsabhängig charakterisiert und im Hinblick auf die spin-polarisierten Zustände in Bi untersucht. So konnten Rashba-spinaufgespaltene elektronische Zustände in der Volumenbandlücke des ferroelektrischen Substrates nachgewiesen werden. Eine Variation der Filmdicke in Bi/$BaTiO_3$ führte zu einer energetischen Verschiebung und zu einer Änderung des Fermivektors der spinaufgespaltenen Zustände. Diese Beobachtung hängt stark mit dem Ausbilden eines Grenzflächenzustandes zusammen, der für sehr niedrige Bedeckungen beobachtet wurde. Beide Effekte weisen zudem auf eine Wechselwirkung zwischen den Bi-Filmen und $BaTiO_3$ hin.

Abstract

Transition metal oxides (TMO) represent a highly interesting material class as they exhibit a variety of different emergent phenomena including multiferroicity and superconductivity. These effects result from a significant interplay of charge, spin and orbital degrees of freedom within the correlated d-electrons. Oxygen vacancies (OV) at the surface of certain d^0 TMO release free charge carriers and prompt the formation of a two-dimensional electron gas (2DEG). Barium titanate ($BaTiO_3$) is a prototypical and promising d^0 TMO. It displays ferroelectricity at room temperature and features several structural phase transitions, from cubic over tetragonal (at room temperature) and orthorhombic to rhombohedral. The spontaneous electric polarization in $BaTiO_3$ can be used to manipulate the physical properties of adjacent materials, *e.g.* in thin films. Although the macroscopic properties of $BaTiO_3$ are studied in great detail, the microscopic electronic structure at the surface and interface of $BaTiO_3$ is not sufficiently understood yet due to the complex interplay of correlation within the d states, oxygen vacancies at the surface, ferroelectricity in the bulk and the structural phase transitions in $BaTiO_3$.

This thesis investigates the electronic structure of different $BaTiO_3$ systems by means of angle-resolved photoelectron spectroscopy (ARPES). The valence band of $BaTiO_3$ single crystals is systematically characterized and compared to theoretical band structure calculations. A finite p-d hybridization of titanium and oxygen states was inferred at the high binding energy side of the valence band. In $BaTiO_3$ thin films, the occurrence of spectral weight near the Fermi level could be linked to a certain amount of OV at the surface which effectively dopes the host system. By a systematic study of the metallic surface states as a function of temperature and partial oxygen pressure, a model was established which reflects the depletion and accumulation of charge carriers at the surface of $BaTiO_3$. An instability at $T \approx 285\,\mathrm{K}$ assumes a volatile behavior of these surface states.

The ferroelectricity in $BaTiO_3$ allows a control of the electronic structure at the interface of $BaTiO_3$-based heterostructures. Therefore, the interface electronic structure of Bi/$BaTiO_3$ was studied with respect to the strongly spin-orit coupled states in Bi by also including a thickness dependent characterization. The ARPES results, indeed, confirm the presence of Rashba spin-split electronic states in the bulk band gap of the

ferroelectric substrate. By varying the film thickness in Bi/$BaTiO_3$, it was able to modify the energy position and the Fermi vector of the spin-split states. This observation is associated with the appearance of an interface state which was observed for very low film thickness. Both spectral findings suggest a significant coupling between the Bi films and $BaTiO_3$.

TABLE OF CONTENTS

CHAPTER 1

INTRODUCTION AND MOTIVATION

Conventional electronic devices, nowadays, are mainly based on semiconductors and semiconductor heterostructures. On the one hand, the conductivity properties of semiconductors can be easily manipulated and varied by doping, gating and temperature. On the other hand, the combination of semiconducting layers in a heterostructure can result in the formation of a two-dimensional electron gas (2DEG) at the interfaces. This conducting channel represents the starting point for the development of high-electron-mobility transistors as in GaN-based systems [1]. The presence of a 2DEG in semiconducting interfaces has been an important prerequisite for the discovery of the integer [2] and fractional [3] quantum Hall effect. In general, conventional semiconductor electronic devices exhibit a wide range of applicability, *e.g.* in transistors, light-emitting diodes, etc. The performance and reliability of these devices, however, is strongly restricted to their size due to self-heating effects [4]. These limitations have promoted the search for other alternative materials with additional physical properties.

In the last years, there has been considerable effort to realize similar concepts in the field of oxide heterostructures [5–11]. These materials have distinct advantages over the use of conventional semiconductors. Almost every naturally occurring compound on earth's surface is an oxide. As these oxides usually are quite inert and chemically stable under standard conditions, they can be easily processed with respect to practical applications [12]. In addition, the class of oxides contains metallic conductors, semiconductors as well as insulators. These electric properties allow oxides to serve as *e.g.* source, drain and gate in a field effect transistor [13]. Today, even an atomic-layer precision between two different oxide layers is achieved since the fabrication of oxide superlattices and heterostructures has tremendously improved

in the last two decades [7]. All these properties represent important prerequisites in order to implement future oxide devices.

The class of transition metal oxides (TMO) has a further advantage with respect to conventional semiconductors. In these systems, strongly correlated d electrons from the transition metal are embedded in an oxygen environment. A finite correlation between these d electrons restricts a complete filling of d states per transition metal lattice site and, hence, enables a local interaction of spin, charge and orbital degrees of freedom [11]. The entanglement of these individual degrees of freedom varies among the different TMO so that each TMO possess slightly different and unique physical properties, namely magnetism, electrical transport, thermal conductivity, optical response and superconductivity.

A first groundbreaking step towards a possible realization of oxide devices has been the observation of a high mobility electron gas at the interface of the two TMO $LaAlO_3$ and $SrTiO_3$ (LAO/STO) [14]. The microscopic origin of the 2DEG at oxide heterostructures, in contrast to the semiconducting material class, can not be explained by a simple band picture but comprises three crucial aspects [15]: i) the occurrence of a 2DEG might be attributed to an electronic reconstruction at the interface [14]. Other studies, moreover, stated that also ii) electrically active defects in the vicinity of the interface [16, 17] and iii) deviations in the stoichiometry of the individual compounds play an important role [18]. A crucial property of the 2DEG at the LAO/STO interface is its superconductivity [19] which might enable the coexistence of superconductivity and ferromagnetism in oxides [20, 21].

The formation of a 2DEG, however, is not restricted to the LAO/STO interface but has also been observed on oxide surfaces, as on $SrTiO_3(001)$ [22, 23], $TiO_2(001)$ [24] or $KTaO_3(001)$ [25, 26]. For STO, a lot of electronic properties have been proposed to arise from the entanglement of spin, charge, orbital and lattice degrees of freedom in the 2DEG, as *e.g.* Rashba-like spin splitting, quantum Hall effect, coherent polaronic liquid, electron dichotomy, magnetism etc. [27–31]. In both cases, *i.e.* at the TMO surface and interface, the existence of the 2DEG is strongly linked to the presence of oxygen vacancies (OV) [16, 32–34]. The formation of a 2DEG due to OV, however, is a delicate matter. In this respect, it is crucial to understand the equilibrium distribution and diffusion kinetics of the OV as these quantities affect the properties of the 2DEG [35, 36].

Among these TMO, Barium titanate ($BaTiO_3$) possesses the interesting characteristic of being ferroelectric at room temperature [37]. In addition to ferroelectricity, $BaTiO_3$ develops large polarized domains and has excellent dielectric and piezoelectric properties [38]. By analogy with $SrTiO_3$, $BaTiO_3$ displays metallic states at its surface [39] and at charged domain walls [40]. The ferroelectric property in bulk $BaTiO_3$ as well as in $BaTiO_3$ films and heterostructures, however, is of greatest interest. Recent

progress in the growth of oxide films allows also to fabricate high-quality superlattices consisting of, *e.g.*, alternating $BaTiO_3$ and $SrTiO_3$ layers [41]. This makes $BaTiO_3$ heterostructures promising for applications. A change in the period of the superlattice or in the ratio of the individual components affects the ferroelectric properties of $BaTiO_3$ [42]. Additional strain in thin $BaTiO_3$ films, generated due to a certain degree of lattice mismatch with the underlying substrate, leads to similar effects [43]. In that way, the strength of the remanent polarization in $BaTiO_3$ could be enhanced by values up to 250 % in combination with elevated transition temperatures [44]. In addition, highly strained $BaTiO_3$ films exhibit an electroresistance large enough in order to realize ferroelectric tunnel junctions [45, 46].

The discovery of the ferroelectric field effect in thin film oxide heterostructures allows the realization of novel oxide materials in electronic devices [47]. The main concept is based on the modification of the carrier concentration at the interface of two oxide materials induced by the switching of the ferroelectric polarization [48, 49]. Recently, this effect has also been observed in the heterostructure $BaTiO_3$/Ge(001) [50] promoting ferroelectric field-effect transistors based on $BaTiO_3$ thin films. A further or actually the ultimate step regarding the implementation of $BaTiO_3$ in heterostructures is the coupling of its ferroelectricity to physical quantities of adjacent materials. For instance, the magneto-electric coupling in Fe/$BaTiO_3$ enables a direct control of the magnetism in Fe by means of proximity effects [51, 52]. In that regard, also a ferroelectric control of the 2DEG at an oxide heterointerface might be achieved [53].

The ferroelectric behavior of $BaTiO_3$ at room temperature has been known for almost 70 years [54]. A large variety of subsequent studies improved the knowledge of the macroscopic properties of ferroelectricity [38]. In addition, a ferroelectric response of $BaTiO_3$ has already been successfully applied in oxide heterointerfaces [55, 56]. However, a lot of open questions remain to be addressed, in particular, concerning the microscopic electronic structure of $BaTiO_3$ at its surface and interface. The main difficulty is that several complex aspects collectively shape the low-energy electronic structure of $BaTiO_3$: the ferroelectricity in $BaTiO_3$ accompanied by the formation of domains, the different structural phases of $BaTiO_3$ and the respective phase transitions, a possible electronic correlation due to the Ti 3*d* states and the formation of oxygen vacancies at the $BaTiO_3$ surface.

The goal of this thesis is to investigate the electronic properties of $BaTiO_3$ systems by angle-resolved photoelectron spectroscopy (ARPES). ARPES, in general, allows to directly map the electronic band structure of a material and is sensitive to many-body effects. Thereby, the microscopic electronic structure of $BaTiO_3$ single crystals and $BaTiO_3$ thin films in the bulk and at the surface shall be unveiled. An additional objective of this thesis is to explore ferroelectric proximity effects on strongly spin-orbit

coupled states at the interface of a $BaTiO_3$-based heterostructure, namely the Rashba Ferroelectric Heterostructure Bi/$BaTiO_3$(001).

In particular, the following questions are raised: i) is the band dispersion of the O $2p$ valence band resolvable by ARPES, can the experimental result be compared to band calculations and to what extent does p-d hybridization of conduction and valence band states play a role in the spectral weight of O $2p$? ii) does a 2DEG exist at the surface of $BaTiO_3$, what is its microscopic origin and how do oxygen vacancies affect this 2DEG or the electronic structure at the surface in general? iii) do spin split surface states appear in a Bi/$BaTiO_3$ heterostructure, what happens to the electronic structure when the thickness of the Bi films is decreased and is a coupling of ferroelectricity and spin-orbit split states observable?

In order to address these questions the thesis is structured as follows. Chapter 2 introduces the two materials of interest, $BaTiO_3$ and Bismuth (Bi), by presenting profound concepts of the respective material. Starting with their structure and characteristic physical properties, their electronic structure in the bulk and at the surface is derived. Chapter 3 introduces the experimental technique which has been used to determine the electronic structure, namely photoelectron spectroscopy in general and also states some specific methods which have been used. In addition, the experimental setup and the sample preparation are presented. Chapter 4 covers some basic results on the bulk electronic structure of $BaTiO_3$ measured by ARPES. On the one hand, the band structure of the O $2p$ valence band is compared to band structure calculations and investigated in dependence on the surface condition and temperature. On the other hand, the insulating nature and the hybridization in pure $BaTiO_3$ is determined by means of the Ti $2p$ core-levels.

Chapter 5 studies the surface electronic structure of $BaTiO_3$ thin films via ARPES. A quasi-particle state and an incoherent spectral contribution are observed at the Fermi level of $BaTiO_3$. Their orbital character is deduced from the results of a photon energy, polarization and resonance study. In addition, the occurrence of the surface electronic states at the Fermi level is linked to the formation of oxygen vacancies at the surface of $BaTiO_3$. Thereby, the density of oxygen vacancies can be controlled by the illumination of the sample with synchrotron light, by the partial oxygen pressure in the chamber and by the sample temperature. The integrated spectral weight of the quasi-particle state and the incoherent spectral contribution as a function of temperature is described by an appropriate theoretical model for the electron density of a 2DEG. In addition, the charge state of the oxygen vacancy is determined which provides information about the number of itinerant and trapped electrons in the system.

Another relevant topic in this thesis is the interface electronic structure of $BaTiO_3$ in a particular heterostructure, Bi/$BaTiO_3$(001). Beside the magneto-electric coupling,

a direct control of the ferroelectric polarization in $BaTiO_3$ on spin-polarized carries has been demonstrated [57]. Further studies reveal that the Rashba-type spin-orbit coupling [58, 59], in general, can be manipulated by means of ferroelectricity [60–62]. Possible application which result from a well-controlled engineering of the spin-splitting in electronic states can be summed up under the concept of spintronics [63, 64]. The spin field-effect transistor [65], thereby, is probably the most important example. Referring to this exploratory work, in particular to the theoretical study on a monolayer of Bi on $BaTiO_3$(001) [60], the surface structure of the Bi films in Bi/$BaTiO_3$(001) as well as the electronic structure at the interface is investigated in Chapter 6. The results demonstrate the realization of large spin split surface state on a ferroelectric substrate and the appearance of a peculiar interface state in Bi/$BaTiO_3$(001).

All the outcome obtained in Chapter 4 – 6 is summarized in Chapter 7. The results from the respective chapters allow to draw conclusions which address a possible implementation of future devices based on $BaTiO_3$. At the end of Chapter 5 and 6 a short outlook in the field of oxide heterostructures is given.

CHAPTER 2

MATERIALS OF INTEREST

Within the wide range of solid state materials there are two specific types of electronic systems which are addressed in this thesis. The class of d^0 TMO range from narrow- to wide-band gap insulators for binary and ternary compounds, respectively [66]. The detailed electronic structure depends on the crystal structure of the TMO and on the configuration of bonding orbitals between the transition metal and the oxygen ligands [12]. Electron correlation, defects and changes in the (surface) stoichiometry, however, can tremendously influence the electronic properties of the TMO [67]. The perovskite $BaTiO_3$ (BTO) represents one special case among the different TMO as it displays ferroelectrically polarized domains at room temperature.

The other class of material can be classified by the presence of strong spin-orbit coupling (SOC). This physical property contributes to the total energy of electronic states and, thereby, influences the electronic structure of the material. Under certain conditions, SOC can even lead to a spin splitting in electronic states. In the group-V semimetal Bi, the SOC is rather strong which slightly affects the dispersion of the bulk bands but most prominently changes the electronic properties of the surface states.

2.1 d^0 Transition Metal Oxides

The unique structure inherent to TMO allows the interplay of charge, spin and orbital degrees of freedom at a given lattice site [11] which might lead to novel phenomena in the field of condensed matter physics. For instance, manganese oxide compounds exhibit the colossal magnetoresistance (CMR) [68] while high T_C systems are realized

in doped oxide-based superconductors [69]. Thereby, the physical properties strongly depend on the configuration of the d orbital of the transition metal [70]. Recently, the $3d^0$ system based on the transition metal Titanium became a topic of increasing interest. The most studied example is $SrTiO_3$ (STO) which shows electronic states of two dimensional character at its bare surface [22, 23] as well as superconducting carriers at the interface with $LaAlO_3$ [19].

2.1.1 Perovskite crystal structure

A very prominent structure among the TMO is the class of ABO_3 perovskite crystals. Its cubic structure is depicted in Figure 2.1:

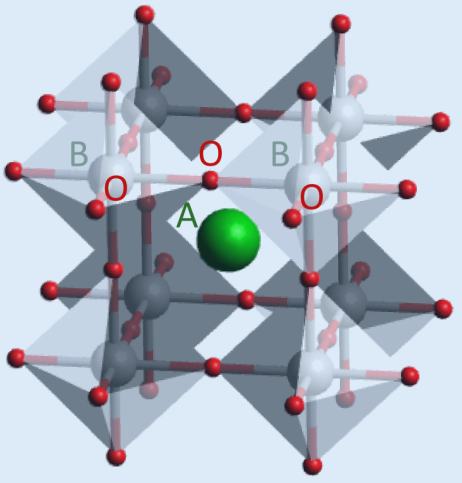

Figure 2.1: Crystal structure of a general ABO_3 perovskite. The transition metal B (gray) is situated in the center of an oxygen octahedron $[BO_6]^{n-}$ (red). Eight of these octahedrons located at the corner of a cubic system provide the surrounding of the alkaline earth metal A (green).

In the perovskite structure the alkaline earth metal A ideally has a coordination number of twelve. This means that it is surrounded by twelve identical oxygen atoms O. The transition metal B has a six-fold coordination and is located at the center of an oxygen octahedron. From a different point of view the perovskite crystal can be regarded as alternating AO and BO_2 stacking layers. In the case of STO and BTO, which are prominent representatives of d^0 TMO, the bonding nature between the alkali metal Sr^{2+} or Ba^{2+} (green) and the $[TiO_6]^{8-}$ octahedron is supposed to be mainly ionic (Figure 2.1). Within the octahedron, however, there also exists a certain amount of covalency between the transition metal Ti^{4+} (gray) and the oxygen atoms O^{2-} (red) [71, 72]. In general, the physical properties of a TMO are to a large extent determined by the transition metal, more precisely by the energetic situation of the transition metal d-states. In our case this involves the energy position of the Ti $3d$ states and their occupation.

The oxygen ligands which bond to the transition metal and form the $[TiO_6]^{8-}$ octahedron produce an external field. This so called crystal field lifts the degeneracy

of the Ti $3d$ orbitals and the energy of the e_g and t_{2g} states is increased and lowered, respectively (see Figure 2.2). Depending on their orientation with respect to the ligands the electrostatic repulsion between the O $2p$ states and the respective Ti $3d$ orbitals varies. For instance, the $d_{x^2-y^2}$ - e_g orbital which is directed along the lobes of the p_x and p_y states is energetically less favorable than the d_{xy} - t_{2g} orbital which points along the plane diagonal due to orbital overlap [73]. A distortion of the $[TiO_6]^{8-}$ octahedron itself, *e.g.* by a compression or extension along one axis, leads to a further splitting of the Ti $3d$ states and additionally affects the degeneracy of the O $2p$ valence states. Both effects are accurately described within the Jahn-Teller theory.

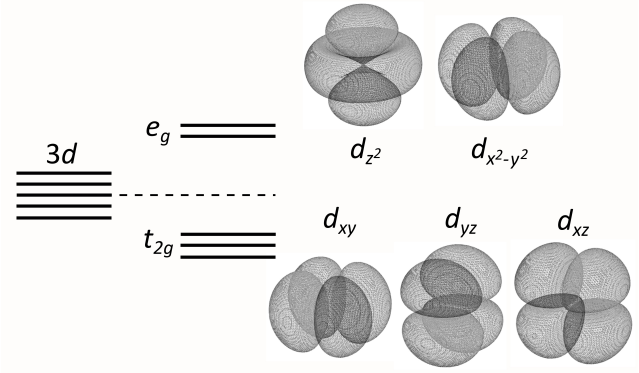

Figure 2.2: Crystal field splitting of d orbitals. The oxygen octahedron lifts the degeneracy of the d orbitals into e_g and t_{2g} states.

2.1.2 Jahn-Teller Effect

The Jahn-Teller effect (JTE), in general, determines the equilibrium geometry of any material system (*e.g.* in molecules, in crystals, etc.) by considering its energy landscape as a function of all possible distortions Q. Certain displacements, however, might also induce the formation of new covalent bonds which stabilize low-symmetric configurations [74]. As already mentioned, the bonding within the $[TiO_6]^{8-}$ octahedron is not entirely ionic but includes additional covalency between valence and conduction electrons. Hence, the high-symmetry structure of the $[TiO_6]^{8-}$ octahedron (without distortion) might not be the energetically most stable configuration. A detailed consideration by means of the Jahn-Teller effect, however, clarifies the situation in the $[TiO_6]^{8-}$ octahedron. Thereby, the energy of the electronic ground state is expanded as a function of the distortion Q according to the concept of perturbation theory [75]:

$$E(Q) = E(0) + \langle 0|(\delta H/\delta Q)_0|0\rangle Q + \frac{1}{2}\left(\langle 0|(\delta^2 H/\delta Q^2)_0|0\rangle - 2\sum_n \frac{\left|\langle 0|(\delta H/\delta Q)_0|n\rangle\right|^2}{E_n - E(0)}\right)Q^2 + \ldots \tag{2.1}$$

with the energy of the undistorted ground state $E(0)$ and of the excited states E_n and their corresponding wavefunctions $|0\rangle$ and $|n\rangle$.

In the following, only the first excited state $|1\rangle$, which reflects the displacement of the Ti^{4+} ion from the center, is regarded. This reduction of the system to a two-level problem actually leads to the representation of the so-called pseudo Jahn-Teller effect. For non-degenerate states, as in our case, the term linear in Q is zero. The first quadratic term stabilizes the ground state energy due to Coulomb repulsion between electron clouds, *i.e.* the undistorted system is energetically favorable [75]. In contrast, the second quadratic term stabilizes the off-centering of the Ti^{4+} ion within the octahedron. This distortion results from vibronic coupling between the ground and the first excited state [74]. Three important criteria result in a reduction in energy upon distortion of the system: first, the configuration of closed-shell ions reduces the spacial extension of the involved orbitals. Hence, the Coulomb repulsion is minimized and the first quadratic term becomes smallest. Second, low-lying excited states lead to an enhanced mixing with the ground state. The small energy difference E_n - $E(0)$ enlarges the magnitude of the second quadratic term. Third, the excited states have to satisfy strong symmetry restrictions [74]. The case of a noncentrosymmetric distortion for a given centrosymmetric ground state implies that the lowest excited state has to be noncentrosymmetric in order to have a non-vanishing contribution of the second quadratic term [75].

In the Ti-based d^0 TMO (as in STO and BTO) these requirements are fulfilled. The shell of the Ti^{4+} ion is closed and the symmetry of the excited system with an off-center displacement (noncentrosymmetric) differs from the unperturbed crystal structure (centrosymmetric). Thus, the displacement of the Ti^{4+} ion from the center of the octahedron is energetically stable and the energy minima within the octahedron are each situated along the eight [1 1 1] directions [74]. A displacement of the Ti^{4+} ion also affects the electronic structure, *i.e.* distinct O $2p$ and Ti $3d$ energy levels in the density of states (DOS) are shifted with respect to the undistorted case [72]. However, already the unperturbed perovskite structure decisively determines the electronic structure of Ti-based d^0 TMO.

2.1.3 Electronic structure in TMO

The energy levels of electronic states (mainly valence and conduction band) crucially depends on the symmetry of the system and of its individual components. Changing the point of origin in the perovskite structure displayed in Figure 2.1 essentially facilitates the symmetry consideration. In the new basis the B atom is situated at the origin, the A atoms at the corners and the O atoms at the face centers of a simple

cubic cell. The Bravais lattice of a perovskite, hence, is simple cubic and belongs to the space group O_h^1 in the Schönflies notation ($Pm\bar{3}m$) [76]. For the respective atoms this implies that also A and B are located at sites with full cubic point symmetry (O_h) while the oxygen atoms O have tetragonal symmetry (D_{4h}) [76]. All high-symmetry points and lines in k-space are illustrated in the corresponding Brillouin zone (BZ) of Figure 2.3.

There are several different approaches to describe the band structure of a given system. Here, a quite simple but very intuitive electronic structure calculation for the perovskite STO is presented. It involves the linear combination of atomic orbitals (LCAO) or tight binding method by using Bloch functions [77–79]. Thereby, point-ion or Madelung potentials [79] are incorporated into the LCAO ansatz. Later methods mainly use a different choice of potentials, namely the muffin-tin potentials [76]. Now-a-days, also completely different approaches including density functional theory are employed [80, 81]. However, this approach which is presented here already qualitatively covers the main electronic features of the system. Figure 2.4 displays the band structure of STO for selected high-symmetry lines taken from Ref. [79].

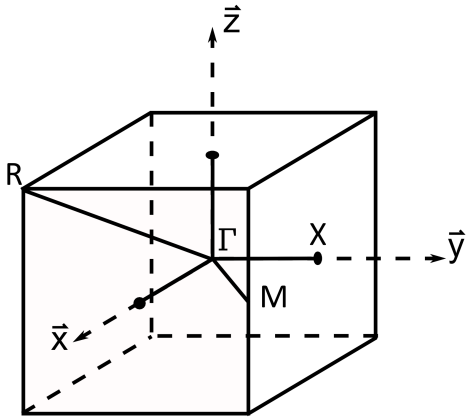

Figure 2.3: Brillouin zone of ABO_3. The primitive cell is simple cubic with the high-symmetry points Γ, X, M and R.

The high-symmetry points Δ, Σ and Λ are located in the middle of the corresponding high-symmetry lines Γ - X, Γ - M and Γ - R. In a d^0 TMO only the Ti $3d$ and O $2p$ states are taken into account since the next neighboring energy levels (O $2s$ and A $5s/6s$) are significantly below or above the considered energies [79]. The O $2p$ - Ti $3d$ energy gap in the calculation was adjusted to the optical gap [82] by varying the oxygen charge. In addition to the ionic charges and the crystal field splitting, the LCAO method includes also nearest neighbor O - O and Ti - O overlap integrals (no Ti - Ti). The O - O bonds have either σ ($pp\sigma$) or π ($pp\pi$) character. Same notation applies for the Ti - O terms which are ($pd\sigma$) and ($pd\pi$), respectively, with $(pd\pi) \approx 0.4\,(pd\sigma)$ [79].

The band structure in Figure 2.4 reflects important properties of a d^0 TMO. First, this material system is a band insulator due to the p - d band gap of ≈ 3 eV. However, one has to keep in mind that this value was indirectly chosen as an input parameter.

Second, at the Γ-point ($k = 0$) the energy separation of the conduction band into E_g (Γ_{12}) and T_{2g} ($\Gamma_{25'}$) in Mulliken (Bethe) notation is solely due to the crystal field splitting of Ti $3d$ states [73]. In the case of the valence band a similar splitting of the states at $k = 0$ into E_u (Γ_{15}), A_{2u} (Γ_{25}) and E_u (Γ_{15}) in Mulliken (Bethe) notation occurs [73]. This fact is due to the $(pp\sigma)$ and $(pp\pi)$ interaction and the axial crystalline field. Third, $(pd\sigma)$ and $(pd\pi)$ terms contribute to the band structure for nonzero k values. Thereby, the intermixing of p and d orbitals increases towards the zone boundaries and enhances the band splitting and, hence, the band width. In addition, the degeneracy of the particular states is further lifted. Its large contribution at the edge of the BZ increases the bandwidth of both valence and conduction bands dramatically (≈ 4 eV) [79]. Although the total energy eigenvalues in this LCAO approach might not be completely accurate the general trends in the dispersion are nicely reflected. In general, the interplay of O $2p$ and Ti $3d$ states tremendously influences the electronic structure of a d^0 TMO, in this case STO.

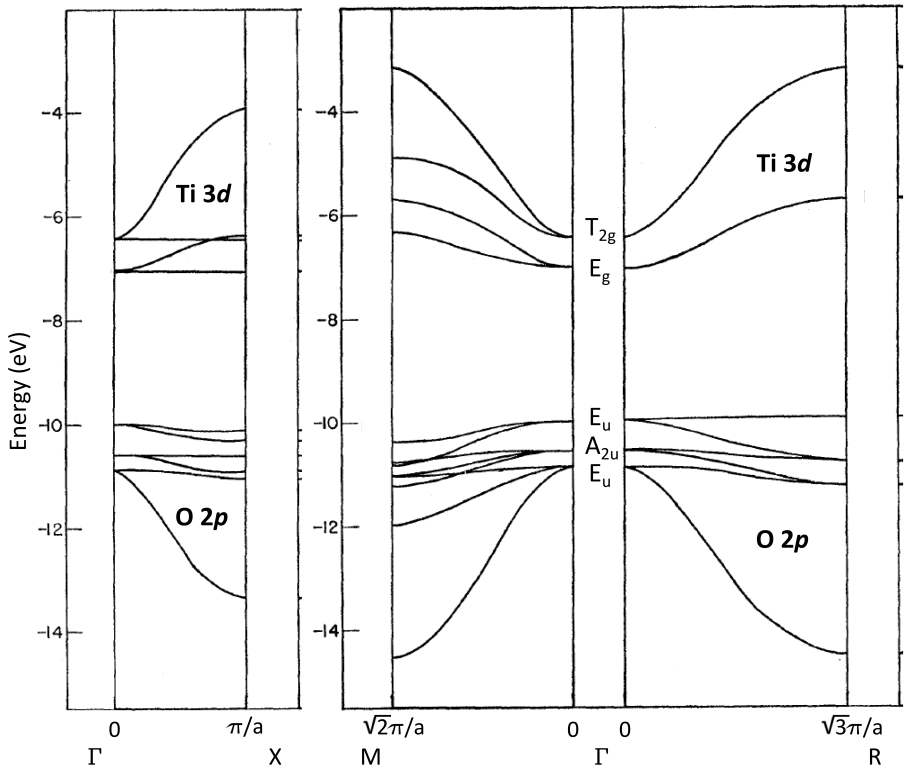

Figure 2.4: Band structure of $SrTiO_3$ along Γ - X, Γ - M and Γ - R direction taken from Ref. [79].

2.1.4 Correlation effects in early-3d-TMO

So far we assumed that in the nominally d^0 TMO, as STO and BTO, the Ti ion actually has d^0 configuration (Ti^{4+}). In this purely ionic approximation the mentioned perovskite materials are band insulators as shown in the previous subsection. Charge

or electron density maps in various theoretical calculations exhibit a Ti static charge which is significantly smaller (between 3+ and 2+) in both STO and BTO than in the pure ionic case (nominally 4+) [71, 80, 83]. This also results in a finite occupation of the Ti $3d$ states (between zero and one).

A system with one electron per lattice site is treated by the Hubbard model [84]. Thereby, the Hamiltonian $\hat{H}$ is determined by a hopping term t between neighboring lattice sites and a Coulomb energy U which accounts for the energy cost of two electrons situated at the same lattice site. In the case of $U \ll t$, the Coulomb interaction term is negligible and the system is described by the tight-binding Hamiltonian for simple metals; for $U \gg t$ the system is in the regime of a Mott-Hubbard insulator [67]. Both situations are illustrated schematically in Figure 2.5 by their corresponding DOS in the vicinity of E_F:

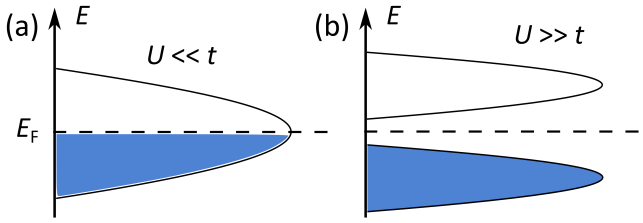

Figure 2.5: Representation of the DOS near E_F for a metal in (a) and a Mott-Hubbard insulator in (b) adapted from [85].

In a simple metal, electrons can be excited into the conduction band since a respective band crosses E_F. As the Coulomb energy U is dramatically increased, the single band splits up into two while forming a energy gap around E_F (Mott-Hubbard insulator).

The description of a Mott-Hubbard model partly can be applied to the titanium-based perovskite systems when the Ti $3d$ conduction band is filled by exactly one electron. The d-d Coulomb interaction U in a d^1 TMO as $LaTiO_3$ and $YTiO_3$ is fairly large [86]. In a perovskite, however, no direct hopping between two titanium atoms is possible as an oxygen atom lies in between (see Figure 2.1). Besides the hopping term between two Ti $3d$ atoms also the O $2p$ orbitals have to be included in the description of a TMO system. The problem is then given by the following Hamiltonian [67]:

$$\begin{aligned}\hat{H} = \sum_{i,j} \left\{ \epsilon_d d^+_{i\sigma} d_{i\sigma} + \epsilon_p p^+_{j\sigma} p_{j\sigma} - t_{pd} \left(d^+_{i\sigma} p_{j\sigma} + \text{h. c.} \right) \right\} \\ + U_{dd} \sum_i n_{d_i\uparrow} n_{d_i\downarrow} + V_{pd} \sum_{\langle ij \rangle} n_{p_i} n_{d_j},\end{aligned} \tag{2.2}$$

where U_{dd} is the d-d Coulomb interaction, V_{pd} represents the intersite repulsion of $3d$ and $2p$ electrons, ϵ_d,ϵ_p are the energies of the $3d$ and the $2p$ states, respectively, t_{pd} describes the hopping amplitude and i, j are the site indices. $d^+_{i\sigma}$ and $d_{i\sigma}$ or $p^+_{j\sigma}$

and $p_{j\sigma}$ are the creation and annihilation operators of the respective orbitals and $n_{d_i\uparrow}$, $n_{d_i\downarrow}$ are the number operators defined by $n_{d_i\sigma} \equiv d^+_{i\sigma} d_{i\sigma}$. The term "h. c." stands for hermitian conjugate. In this description the p - p Coulomb interaction and the hopping term between two O $2p$ orbitals was neglected as their contributions are significantly smaller than the other terms.

The Hamiltonian $\hat{H}$, in general, considers electronic interactions within and in between single lattice sites. Thereby, the electronic structure of the system is described in a "local" picture, in contrast to the common band picture. Another important parameter in this "local" description of $\hat{H}$, besides the Coulomb energy U, is the charge transfer energy Δ. It describes the energy difference between the d- and p-band represented by $\Delta \equiv \epsilon_d$ - ϵ_p. By relating U to Δ two cases can be distinguished: for $\Delta \gg U$, the system is in the regime of a Mott-Hubbard insulator which features an insulating ground state. In this case, hopping between the particular Ti atoms is prohibited due to the Coulomb repulsion U. If $\Delta \ll U$ the charge transfer energy Δ is the reference parameter. The gap size determines the charge excitation from the O $2p$ to the Ti $3d$ state and the insulating ground state is called charge transfer insulator. However, in the case of a comparable large t_{pd} or t, *i.e.* $t \geq U$ or $t \geq \Delta$, electrons can smoothly hop in between lattice sites and the system is considered to be a simple metal. An illustration of all regimes with respect to the corresponding parameters is shown in Figure 2.6 [87]:

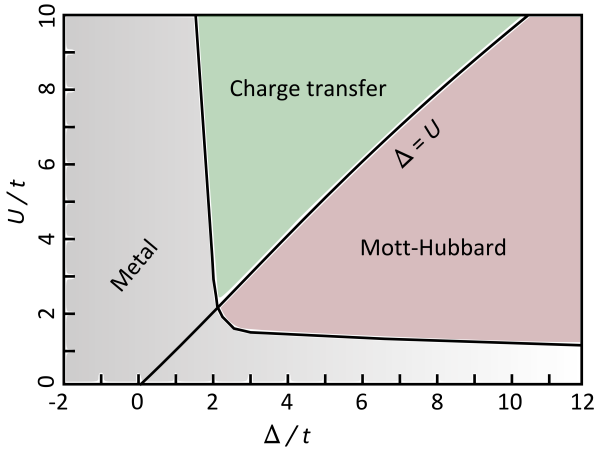

Figure 2.6: Phase diagram illustrating the regimes for a Mott-Hubbard and a charge transfer insulator following the diagram of *Zaanen-Sawatzky-Allen* (adapted from Ref. [87]).

Most of the TMO are situated in either one of both regimes according to this "local" description [88, 89]. STO and TiO_2, for instance, are situated in the intermediate regime ($\Delta \approx U$) but slightly more on the charge transfer side [89]. For BTO, however, a classification according to the *Zaanen-Sawatzky-Allen* phase diagram is missing.

2.1.5 Effects of defects and oxygen vacancies

Up to here the theoretical considerations include only a perfect crystal structure without any imperfections like defects or impurities. However, the upper most layers of TMO surfaces tend to create oxygen vacancies (OV) under certain conditions (for details see Section 3.8). These defects or vacancies additionally influence the electronic structure of the presented TMO.

Such a situation can be described by an impurity situated in a host electron system which is treated within the Anderson impurity Hamiltonian $\hat{H} = \hat{H}_{\text{Fermi}} + \hat{H}_{\text{OV}}$ [90]. The first term $\hat{H}_{\text{Fermi}}$ represents the "kinetic" part of Equation (2.2) neglecting the Coulomb energy U. Here, besides the hopping t_{pd} between the neighboring p and d orbitals also hopping t_{pp} between two next-nearest neighbor p orbitals is considered. In the 2D representation within the x-z plane $\hat{H}_{\text{Fermi}}$ yields [34]:

$$\begin{aligned}\hat{H}_{\text{Fermi}} = &\sum_{i,j,o=x,z} \left\{\epsilon_d d_i^+ d_i + \epsilon_p p_{j,o}^+ p_{j,o}\right\} \\ &- \sum_{i,j} \left\{t_{pd}\left[d_i^+ p_{j,x} + d_i^+ p_{j-\hat{x},x} + d_i^+ p_{j,z} + d_i^+ p_{j-\hat{z},z} + \text{h. c.}\right]\right\} \\ &- \sum_{i,j} \left\{t_{pp}\left[p_{j,x}^+ p_{j,z} + p_{j,x}^+ p_{j+\hat{x},z} + p_{j,x}^+ p_{j-\hat{z},z} + p_{j,x}^+ p_{j+\hat{x}-\hat{z},z} + \text{h. c.}\right]\right\},\end{aligned} \tag{2.3}$$

where $\hat{x}$ and $\hat{z}$ are displacements from the lattice site j in direction of x or z, respectively, and $o = x, z$ represent the direction of the p_o orbitals. All other parameters are already explained in connection with Equation (2.2). The interaction of the itinerant electrons with the OV is given by the correlation term $\hat{H}_{\text{OV}}$ [34]:

$$\hat{H}_{\text{OV}} = \sum_{\sigma} \left\{\epsilon_{\text{imp}} c_{b\sigma}^+ c_{b\sigma} + E_{\text{OV}} p_{j,z}^+ p_{j,z} - g\left[c_{b\sigma}^+ d_{i\sigma} + c_{b\sigma}^+ d_{i+\hat{z}\sigma} + \text{h. c.}\right]\right\}, \tag{2.4}$$

where $c_{b\sigma}^+$ is the creation operator of a bonding orbital associated with the impurity site, E_{OV} is a large on-site potential in order to model an oxygen vacancy and g represents the coupling between two Ti $3d$ orbitals and the bonding orbital.

Figure 2.7 displays the schematic picture of the band structure and of the individual orbital contributions as well as coupling or hopping terms discussed in Equations (2.3) and (2.4). Through the creation of an OV (*e.g.* at the surface of a TMO) two electrons are released into the host system. These electrons might be either itinerant and occupy a delocalized bath level, *i.e.* the formerly empty Ti $3d$ conduction band, or are trapped in a localized level, the bonding state $|\text{b}\rangle$ illustrated in Figure 2.7 (a) [34]. Moreover, the system is reduced to the 2D representation of the $x-z$ plane so that only O $2p_x$ and O $2p_z$ as well as Ti $3d_{xz}$ orbitals are considered as shown in Figure 2.7 (b). The

bonding orbital (blue) between the two Ti $3d$ states and the OV is a hybrid state based on Ti $3d_{3z^2-r^2}$. Its origin is a local mixing of Ti $3d_{3z^2-r^2}$ and Ti $4p_z$ due to the breaking of symmetry at the OV site, from cubic to C_{4v} symmetry [91].

This model which was adjusted to experimental results (*e.g.* the band gap of 3.2 eV) qualitatively reproduces the observations in the photoelectron spectroscopy experiments of STO [92, 93]. Although it has been confirmed that the in-gap state is related to the formation of oxygen defects at the surface [22], the presented model of Ref. [34] is not completely established. Other studies propose that the energy position of the in-gap state in STO depends on the vacancy clustering [94] or that the properties of the in-gap state in LAO/STO correlate with the thickness of the LAO layer [95]. A recent density functional theory study shows that in the case of multiple OV even two or three localized states might be present in the first few layers of STO [96].

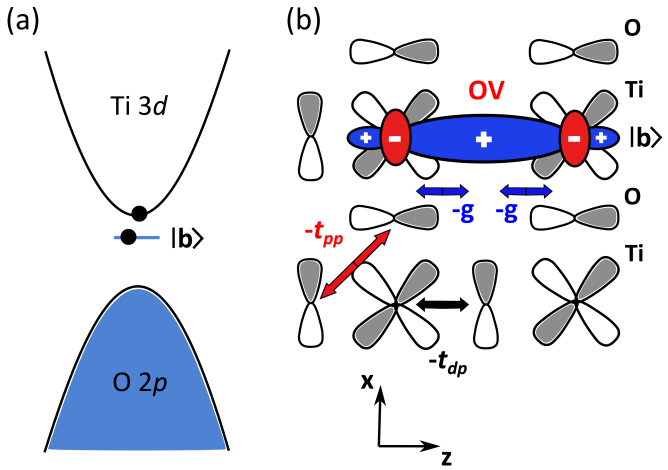

Figure 2.7: Illustration of the band and the local orbital picture for an OV in a TMO in (a) and (b), respectively (adapted from Ref. [34]).

2.1.6 2D Electron Gas at TMO surfaces

The creation of OV at the surface of a TMO leads to a nonuniform charge-carrier distribution at the surface [97]. Fully ionized OV provide two electrons per vacancy site and, hence, act as a dopant. Thereby, an equilibrium surface space-charge layer with a thickness d forms close to the surface of the TMO [97]. In the case of a large d which applies to STO [98] the point-defect concentrations can be schematically illustrated as shown in Figure 2.8 (a). At the surface of the TMO, a surface charge Q_S and an enhanced oxygen vacancy concentration $V_O^{\cdot\cdot}$ are present. The charge discontinuity in the system leads to a subsequent redistribution of the OV as well as to an electrostatic charging in Figure 2.8 (a) highlighted by the black and red solid lines for the oxygen vacancy and electron concentration, respectively. The acceptor concentration A remains the same. Moreover, the presence of electrostatic charges at the surface of TMO causes a potential gradient so that excess electrons can accumulate

in the surface space-charge layer (see bright-red area in Figure 2.8 (a)).

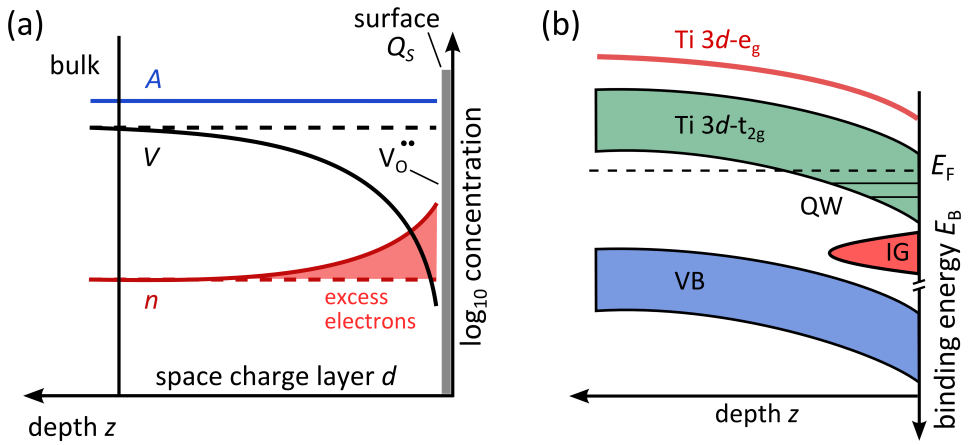

Figure 2.8: (a) Concentration of acceptors A, oxygen vacancies V and electrons n after creation of point-defects in the form of oxygen vacancies at the surface of BTO. Schematic diagram is adapted from Ref. [97]. (b) Band picture of STO including a confining potential at the surface adapted from [93]. This gradient induces a downward bending of the Ti 3d-e_g, Ti 3d-t_{2g} energy levels and the valence band (VB). Simultaneously, quantum well states (QW) and an in-gap state (IG) appear below the Fermi level E_F.

It has been demonstrated that the electrical potential at the surface which depends on the amount of OV [99] can be described by a wedge model [23] or by the Poisson equation implemented into the Schrödinger Hamiltonian [22]. This confining potential induces a downward bending of the individual bands of STO near the surface [93, 97]. As a result the Ti 3d-t_{2g} states of STO shift below the E_F and form 2D quantum well states [22, 23, 93]. A schematic representation of the band structure at the surface is displayed in Figure 2.8 (b). The itinerant electrons which occupy the Ti 3d states exhibit profoundly different physical properties compared to the localized states, so-called in-gap (IG) states.

Changes in the carrier density n which can occur due to a different bulk doping [23] or different ultraviolet irradiation doses [22] do not affect the Fermi contour of STO. The independence on doping implies a 2D character of the respective Ti 3d-t_{2g} states. In addition, this 2D nature was confirmed by the appearance of Shubnikov-de Haas oscillations in δ-doped STO [100]. The impact of the carrier density on the 2D electron gas has also been nicely modeled theoretically [101].

2.1.7 Unique characteristics of $BaTiO_3$

The crystal and electronic structure discussed so far applies for most Ti-based d^0 TMO, as for instance STO, BTO or $CaTiO_3$ (CTO). Since the physical properties in these materials mainly depend on the valence O $2p$ and conduction Ti $3d$ states no crucial consequence might be expected by exchanging the alkali metal from Ca to Sr or to Ba. However, only BTO exhibits some additional and unique properties which do not appear in the other structural isomorphs.

In order to understand the differences among CTO, STO and BTO, it is necessary to compare the adiabatic potential curvature K which represents the energy landscape within the JTE (Subsection 2.1.2) of the three mentioned compounds. $K = K_0 + K_v$ is given by the two quadratic contributions of the pseudo JTE in Equation (2.1). The positive K_0 is the average value of the curvature operator and the negative K_v is the vibronic contribution [74, 102]. Taking into account all possible vibronic excitations, K yields -0.17 , -0.10 and -0.10 for BTO, STO and CTO, respectively [102]. As a consequence, the structural displacement of the Ti^{4+} ion according to theory is most stable in BTO. BTO, indeed, exhibits a tetragonal crystal structure at room temperature resulting from such a distortion. This structural change in BTO is accompanied by the occurrence of **ferroelectricity** [37]. In a ferroelectric material, an atomic displacement establishes a spontaneous electric polarization which can be switched by an external electric field. This physical property might be of great use in non-volatile devices [46, 55, 56]. In contrast, CTO is not ferroelectric and STO shows ferroelectric behavior just at very low temperatures when pressure is applied or in the presence of impurities [74].

Besides its room temperature ferroelectricity BTO displays several **structural phase transitions** on varying the temperature [103] (cubic to tetragonal at 383 K [104], tetragonal to orthorhombic at 278 K [105] and orthorhombic to rhombohedral at 183 K [106]). A schematic picture is shown in Figure 2.9:

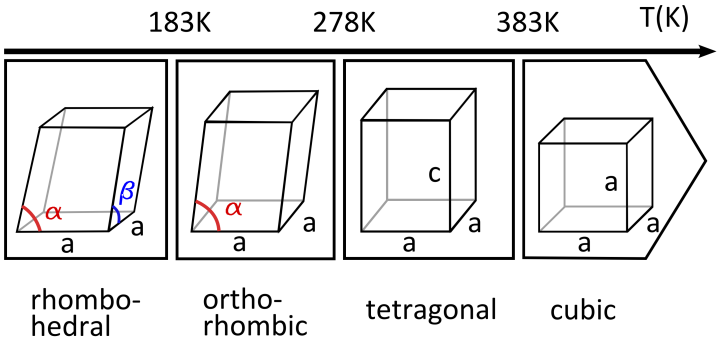

Figure 2.9: Structural phase transitions in BTO.

In the tetragonal phase the electric polarization points along the c-axis ([0 0 1]), in the orthorhombic phase it is oriented along the plane diagonal [0 1 1] and in the rhombohedral phase it follows the room diagonal [1 1 1] [54]. The cubic phase is paraelectric and, hence, shows no spontaneous electric polarization. Initially the ferroelectricity in BTO was explained by the displacive model [107]. Recent theoretical studies, however, revealed that the rhombohedral phase, among the four phases, is the energetically most favorable under distortions (see also Subsection 2.1.2) [37, 74]. These conclusions support a deviating approach in order to understand the ferroelectric phases in BTO, the order-disorder model [108]. According to this theory all ferroelectric phases (with their different polarizations) are actually composed of unit cells with rhombohedral structure. By averaging over a certain number of these unit cells along one direction all the other phases (orthorhombic, tetragonal and cubic) can be constructed. The several structural phase transitions in BTO [103] result from an enhancement in the system's symmetry due to temperature. Experimentally this approach was verified by local structural and electronic probes [109, 110].

Room temperature ferroelectricity, the concurrence of **structural phase transitions** and the possibility of **surface conductivity** (see Subsection 2.1.6) make BTO a potential building block for oxide heterostructures. Due to these reasons BTO is of particular interest and, despite its long scientific history, still the subject of a lot of recent studies, including this thesis.

2.2 Group-V semimetals

In a bulk TMO the conduction band minimum (CBM) and valence band maximum (VBM) usually are separated by a narrow band gap. This insulating behavior in a pure d^0 case is in contrast to a semimetal where the CBM and the VBM both cross E_F. In general, semimetals represent an additional class of solid next to insulators, semiconductors and metals according to electronic band theory. The most prominent representatives are located in group V of the periodic table, as *e.g.* Arsen (As), Antimony (Sb) and Bi.

In particular, Bismuth (Bi) is an essential element in a variety of compound systems which exhibit exceptional physical properties. On the one hand Bi plays an important role in the class of three-dimensional topological insulators (TI) as $Bi_{1-x}Sb_x$ [111] or in Bi_2Se_3 and Bi_2Te_3 [112]. At the surface of these TI, topologically protected surface states span the bulk band gap [113]. This results in a conducting channel at the surface of the insulating bulk materials. On the other hand, Bi forms surface alloys with the noble metals Ag(111) and Cu(111) [114–116] as well as with the semiconductor Si(111) [117]. The presence of a strong Rashba effect in these alloys

induces a large spin-splitting in the electronic structure [58, 118]. In the case of a TI or a Rashba material, the spin-orbit coupling (SOC) has to be significantly strong. This requirement, however, is already fulfilled in pure Bi.

2.2.1 Spin-orbit interaction

In heavy elements the effect of SOC on the total energy of certain states is considerably large. This correlation of atomic number Z and SOC is also displayed in the respective Hamiltonian $\hat{H}_{\mathrm{SOC}}$ which describes the interaction of spin and orbital angular momentum:

$$\hat{H}_{\mathrm{SOC}} = \frac{\hbar}{4m^2c^2}(\nabla V \times \vec{p})\vec{\sigma}, \tag{2.5}$$

where $\vec{\sigma}$ is the Pauli spin operator and ∇V is the potential gradient. The latter parameter reflects the attracting force of the core-hole on the electron and strongly scales with the atomic number of the material. The strong coupling of spin and momentum in the heavy element Bi can be easily detected in its electronic structure. For instance the valence p states ($p_{1/2}$ and $p_{3/2}$) of Bi with an atomic number of $Z = 83$ are split by ≈ 1.5 eV [119]. A detailed description of the electronic properties in Bi in the presence of strong SOC is discussed in Subsection 2.2.3.

In general, when the spin of the electron is included in the representation of the band structure two conditions have to be considered. The presence of time-reversal symmetry in a system leads to a so-called Kramers degeneracy of a Bloch state $\Psi_{\vec{k}}(\vec{r},s)$ with its complex conjugate $\Psi^*_{\vec{k}}(\vec{r},s)$ [113]. In the band structure this fact leads to $E(\vec{k},\uparrow) = E(-\vec{k},\downarrow)$. On the other hand, the preservation of inversion symmetry in the systems results in $E(\vec{k},\uparrow) = E(-\vec{k},\uparrow)$. The combination of both symmetries requires that for every state with the energy $E(\vec{k},\uparrow)$ there has to be a state with inverted spin $E(\vec{k},\downarrow)$. Then, each energy level is occupied by two electrons with opposite spin which is referred to the degeneracy of energy eigenstates. In the bulk electronic structure of Bi the strong SOC results in a lifting of degeneracies [120]. At the surface where also the inversion symmetry of the system is broken SOC even more affects the electronic structure.

However, before displaying the consequences of the SOC on the surface electronic structure of Bi it is necessary to understand the (surface) structure of the material. In general, each crystal symmetry can be assigned to a space group in real space which refers to a BZ in reciprocal space. The symmetry of the corresponding BZ then determines the high-symmetry directions in the electronic structure.

2.2.2 The Bismuth crystal structure

The Bi crystal displays a rhombohedral symmetry and belongs to the trigonal space group R$\bar{3}$m. In this configuration each atom has three equidistant nearest- and next-nearest neighbors. In an alternative perspective the crystal can be regarded to be hexagonal with six atoms per unit cell or, with respect to the rhombohedral ([1 1 1]) direction, as an assembly of buckled bilayers [121, 122]. In the following, the crystal structure of Bi is always described in its representation of a buckled bilayers.

The bilayers are oriented along the Bi(0001) plane of the hexagonal structure which coincides with the Bi(111) plane in the rhombohedral representation. Figure 2.10 illustrates two of these Bi bilayers from a top and a side view [123]. The atoms within the buckled bilayer form covalent bonds which are indicated by black connecting lines (Figure 2.10). In contrast, the individual bilayers interact via some type of van der Waals bonding. Hence, the bonding strength within the bilayer (intra-bilayer) is stronger than between two bilayers (inter-bilayer). This difference is also reflected by the atomic distances shown in Figure 2.10 [122]. These structural aspects determine the symmetry of the BZ of Bi with its high-symmetry points and lines, especially, with respect to its projection to the surface.

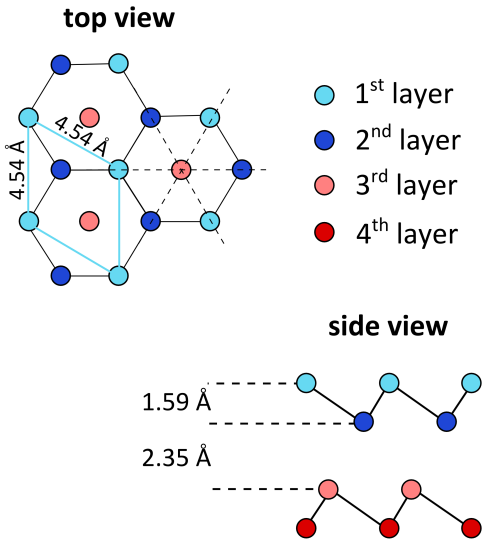

Figure 2.10: Crystal structure of Bi along the (0001) plane. The Bi bilayers are illustrated by a top and a side view (adapted from [123]).

2.2.3 Surface electronic structure of Bi(0001)

Due to the shallow hole and electron pockets at particular high-symmetry points of the bulk BZ (T and L point) Bi exhibits a semimetallic behavior in the bulk [121]. At a critical layer thickness of 30 nm, however, Bi becomes semiconducting by passing through a semimetal-to-semiconductor transition from the bulk material to a thin film

system [124]. In the following, it will be focused on the surface electronic structure of semiconducting thin Bi films.

A projection of the Bi bulk BZ to the (0001) surface leads to a hexagonal surface BZ. In the projected spin-orbit gap of the bulk electronic structure the existence of surface states was reported [125, 126]. These surface states cross the Fermi level E_{F} and show a peculiar Fermi surface which mirrors the symmetry of the SBZ [127]. A schematic of the SBZ and the Fermi surface is illustrated in Figure 2.11 [128].

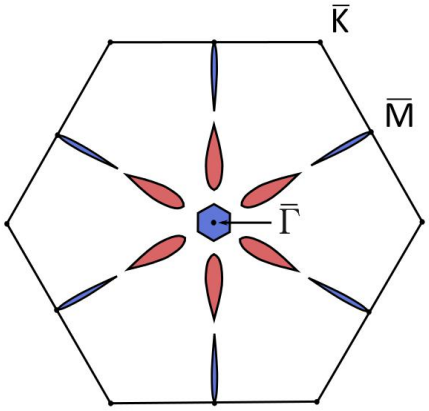

Figure 2.11: Hexagonal SBZ of Bi(0001) with the high-symmetry points $\bar{\Gamma}$, $\bar{M}$ and $\bar{K}$. The corresponding Fermi surface consists of six consecutive electron and hole pockets along the $\bar{\Gamma}$ - $\bar{M}$ direction (adapted from [128]).

The Fermi surface consists of a hexagonal electron pocket at the $\bar{\Gamma}$-point and six hole pockets which form narrow lobes elongated along the $\bar{\Gamma}$ - $\bar{M}$ direction. In addition, at the six $\bar{M}$-points of the SBZ shallow electron pockets appear. The 2D nature of these states was confirmed by photoelectron spectroscopy (PES) measurements [129, 130]. One important property of Bi is its larger number of charge carriers at the surface compared to bulk [122] and, hence, its large surface conductivity [131]. Another aspect is the unique structure of the Fermi surface which can not be explained by geometric considerations nor by the presence of dangling bonds [122]. Instead, the breaking of inversion symmetry in combination with SOC, as explained in the previous subsection, plays an important role.

For the quasi-2D surface states which experience a potential gradient perpendicular to the surface the spin degeneracy $E(\vec{k},\uparrow) = E(\vec{k},\downarrow)$, except at the high-symmetry points, is lifted. In this case, SOC crucially modifies the electronic structure at the surface as shown in Figure 2.12 which is taken from [132]. The splitting of the states is strongly anisotropic and differs along the $\bar{\Gamma}$ - $\bar{M}$ and $\bar{\Gamma}$ - $\bar{K}$ direction. Unfortunately, the surface states in the vicinity of $\bar{\Gamma}$ and $\bar{M}$ lie in the projected bulk bands and are not resolvable in PES experiments [130].

The appearance of spin-split surface states renders Bi an interesting material in the expanding scope of spintronics. Spintronics, in general, aims at exploiting the spin degree of freedom instead of the charge of the carrier. By this concept, the size of

electronic devices can be further reduced without self-heating effects [4].

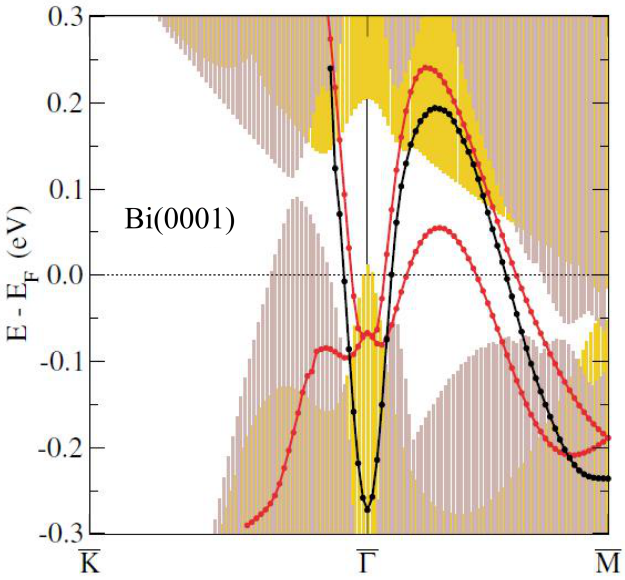

Figure 2.12: Surface electronic structure of Bi(0001). The black and red lines represent the surface states without and with SOC, respectively. The projection of the bulk band is illustrated by the violet (without SOC) and yellow (with SOC) shaded areas (taken from Ref. [132]).

CHAPTER 3

EXPERIMENTAL REPRESENTATION OF THE ELECTRONIC STRUCTURE

The purpose of this thesis is to investigate the properties of pure TMO and TMO-based hybrid systems by probing their electronic structure. A powerful tool to study energy levels of electrons in solids and the band structure of materials, in general, is represented by photoelectron spectroscopy (PES). This chapter covers, on the one hand, the basic theoretical framework of PES and introduces two particular techniques which are applied throughout this thesis. On the other hand, specific conditions that become valid in the study of TMO are discussed. Furthermore, the different experimental conditions including their individual setups are presented and the treatment and preparation of the different sample systems are illustrated.

3.1 Introduction to PhotoElectron Spectroscopy

Photoelectron spectroscopy (PES) is based on the photoelectric effect which has been discovered by Hertz in 1887 and explained by Einstein a few years later [133, 134]. Thereby, the illumination of a material with light can result in the emission of electrons if their kinetic energy is higher than the work function ϕ_0 of the material. These photoelectrons emitted in the photoemission process have a maximal kinetic energy of $E_{kin}^{max} = h\nu - \phi_0$ depending on the excitation energy $h\nu$ of the light.

The measured physical quantity in PES, on the other hand, is the photocurrent $\boldsymbol{I}(\boldsymbol{k}, E_{kin})$ which contains much more information of the studied system than the mere E_{kin} of the photoelectrons determined by energy conservation. The description of $\boldsymbol{I}(\boldsymbol{k}, E_{kin})$ is derived in the following, based on the references [135, 136].

In the photoemission process the interaction between a photon field $\boldsymbol{A}$ and the N-electron system induces the excitation of electrons from their ground states Ψ_i to an available final state Ψ_f. For a weak interaction the transition probability w_{fi} can be approximated by Fermi's golden rule:

$$w_{fi} \propto \frac{2\pi}{\hbar} \left| \left\langle \Psi_f^N \middle| \hat{H}_{int} \middle| \Psi_i^N \right\rangle \right|^2 \delta\left(E_f^N - E_i^N - h\nu\right), \tag{3.1}$$

with the final and initial state energies E_f^N and E_i^N, respectively, the interaction Hamiltonian $\hat{H}_{int}$ and the reduced Planck constant $\hbar$. The δ-function describes the energy conservation in the system.

The sum over all possible transitions determines the photocurrent acquired in PES experiments: $\boldsymbol{I}(\boldsymbol{k}, E_{kin}) \propto \sum_{f,i} w_{fi}$. The interaction Hamiltonian yields

$$\hat{H}_{int} = \frac{e}{2m}(\boldsymbol{A}\cdot\boldsymbol{p} + \boldsymbol{p}\cdot\boldsymbol{A}) - e\phi + \frac{e^2}{2m}\boldsymbol{A}\cdot\boldsymbol{A} \approx \frac{e}{m}\boldsymbol{A}\cdot\boldsymbol{p}, \tag{3.2}$$

where $\boldsymbol{A}$ and ϕ are the vector and the scalar potentials, respectively, $\boldsymbol{p}$ is the momentum operator and m, e are the electron mass and the elementary electron charge. Several assumptions lead to the approximation at the end of Equation (3.2): two photon processes are not considered so that $\boldsymbol{A}\cdot\boldsymbol{A}$ is negligible, the gauge $\phi = 0$ is chosen and the commutator relation $[\boldsymbol{p}, \boldsymbol{A}] = -\mathrm{i}\hbar\,\nabla\cdot\boldsymbol{A}$ is applied.

In addition, the wavelength of the light for low excitation energies ($h\nu \leq 100\,\mathrm{eV}$) is substantially larger than the atomic distances in the photoemission experiment. Under these circumstances the vector potential $\boldsymbol{A} = \boldsymbol{A}_0$ can be regarded as a constant so that $\nabla\cdot\boldsymbol{A} = 0$ [135]. Mathematically, the so-called dipole approximation which is applied to the expansion of the plane wave $\boldsymbol{A}$ leads to the relation [135]:

$$\left\langle \Psi_f^N \middle| \boldsymbol{A}\cdot\boldsymbol{p} \middle| \Psi_i^N \right\rangle \propto \left\langle \Psi_f^N \middle| \boldsymbol{A}_0\cdot\boldsymbol{r} \middle| \Psi_i^N \right\rangle, \tag{3.3}$$

by taking into account commutation relations and the quantum mechanical identity of $\boldsymbol{p}$. The constant $\boldsymbol{A}_0$ contains information about the light polarization ϵ.

Until now, in order to obtain the accurate solution for the photocurrent one has to solve a N electron problem. A common simplification is given by the *sudden approximation*. Within this assumption the photoelectron ϕ_i^k before the excitation is decoupled from the remaining $(N-1)$ electron system Ψ_i^{N-1}. The ionization process itself is considered to take place rather abruptly. As a result the wave function of the

initial system then can be factorized by:

$$\Psi_i^N = \mathscr{A}\phi_i^k\Psi_i^{N-1}, \tag{3.4}$$

where $\mathscr{A}$ is an antisymmetric operator in order to sustain an antisymmetric wave function satisfying the Pauli principle for fermions. The *sudden approximation* has a direct implication on Equation (3.3):

$$\left\langle \Psi_f^N \middle| \boldsymbol{A}_0 \cdot \boldsymbol{r} \middle| \Psi_i^N \right\rangle \propto \left\langle \phi_f^k \middle| \boldsymbol{A}_0 \cdot \boldsymbol{r} \middle| \phi_i^k \right\rangle \left\langle \Psi_m^{N-1} \middle| \hat{c}_k \middle| \Psi_i^N \right\rangle, \tag{3.5}$$

where the first term represents the one-electron dipole matrix element M_{fi}^k, $\hat{c}_k$ is the annihilation operator for an electron and the second term describes the overlap integral of the N electron system with the remaining $(N-1)$ electrons which now are in an excited state Ψ_m^{N-1} with energy E_m^{N-1}.

According to all the assumptions and considerations made above, the transition probability yields:

$$w_{fi} \propto \frac{2\pi}{\hbar}\sum_{f,i}\left|M_{fi}^k\right|^2 \sum_{m,i}\left|\left\langle \Psi_m^{N-1} \middle| \hat{c}_k \middle| \Psi_i^N \right\rangle\right|^2 \delta\left(E_m^{N-1} + E_{kin} - E_i^N - h\nu\right), \tag{3.6}$$

where interference effects between the photoelectron and the remaining $(N-1)$ electrons are neglected. The last sum depicts the spectral function $A(k,w)$ which includes all the many-body effects of the N particle system. In order to solve this rather complicated spectral function $A(k,w)$ the Green's function formalism is applied. However, this is not in the scope of this thesis but can be found in elaborated literature on PES, as *e.g.* in [135]. On the other hand, the one-electron dipole matrix element M_{fi}^k comprises mainly the geometry of the experiment as light polarization, measurement scattering plane, etc.

3.2 PES on core-levels of 3d-TMO

Photoemission experiments on the core-levels of specific materials are usually conducted in the range of X-rays (XPS). At these comparable high photon energies the *sudden approximation* is applicable even in the sense that in the overlap integral the $(N-1)$ initial state Ψ_i^{N-1} is used.

For a constant $\boldsymbol{A}_0$ Equation (3.5) yields [135]:

$$\left\langle \Psi_f^N \middle| \boldsymbol{r} \middle| \Psi_i^N \right\rangle \propto \left\langle \phi_f^k \middle| \boldsymbol{r} \middle| \phi_i^k \right\rangle \sum_s c_{m,i}, \tag{3.7}$$

with the probability $\left|c_{m,i}\right|^2 = \left|\left\langle \Psi_m^{N-1} \middle| \Psi_i^{N-1} \right\rangle\right|^2$ to find the $(N-1)$-particle system in the excited state m after the removal of an electron. The probability factor is unity for a particular $m = \tilde{m}$, where $\Psi_i^{N-1} = \Psi_{\tilde{m}}^{N-1}$ is fulfilled; for all other m $c_{m,i}$ is zero. In the spectrum of PES, the non-zero state ($m = \tilde{m}$) results in the so-called main line at a specific energy which derives from the energy conservation $\delta\left(E_m^{N-1} + E_{kin} - E_i^N - h\nu\right)$ in the system. The shape of this spectral feature can be approximated by a delta function which implies instant photoemission in a non-interacting system, the so-called *sudden approximation* [135]. In strongly correlated systems, however, several $\left|c_{m,i}\right|^2$ are also non-zero due to the non-vanishing overlap of Ψ_i^{N-1} and Ψ_m^{N-1} eigenstates. This results in the contribution of several satellite lines in the spectrum located at lower E_{kin}.

In the respective spectra of $3d$-TM a particular satellite line, namely, the charge transfer satellite appears. The charge transfer in Ti-based TMO between the titanium metal of d character and the oxygen ligand L (introduced in Subsection 2.1.4) crucially affects the eigenstates of the system. This concept can be adopted to the representation of the ground state which then is a linear combination of $3d^0$, $3d^1\underline{L}$ and $3d^2\underline{L}^2$ configurations [137, 138], where $\underline{L}$ represents a hole in the usually fully occupied oxygen $2p$ orbital. For the following we neglect the $3d^2\underline{L}^2$ term since it is qualitatively not changing the XPS spectra. The energy difference in the initial states is given by the charge transfer energy: $E[3d^1\underline{L}] - E[3d^0] = \Delta$. On the other hand, also the final state of XPS is varied by the core hole potential so that the individual final states are $\underline{2p}\,3d^0$ and $\underline{2p}\,3d^1\underline{L}$, where $\underline{2p}$ reflects the core hole. The energy difference of both states yields: $\left|E[\underline{2p}\,3d^1\underline{L}] - E[\underline{2p}\,3d^0]\right| = \left|\Delta - V_{pd}\right|$. V_{pd} represents the p-d hybridization interaction of the O $2p$ orbital with the Ti $3d$ (see Subsection 2.1.4).

The scenario of the XPS process is schematically depicted in Figure 3.1. Thereby, energy E_B reflects the binding energy of the initially excited core electron and is defined by $E_B = E_m^{N-1} - E_i^N$ or by the more commonly used equation within the non-interacting electron picture: $E_B = h\nu - \phi - E_{kin}$. Depending on the magnitude of the energies V_{pd} and Δ either final state 1 ($V_{pd} > \Delta$) or final state 2 ($V_{pd} < \Delta$) is present in the core-level spectra. In the case of final state 1 the main line consists of $3d^1\underline{L}$ states and the satellite line of $3d^0$ states and for final state 2 the situation is *vice versa*.

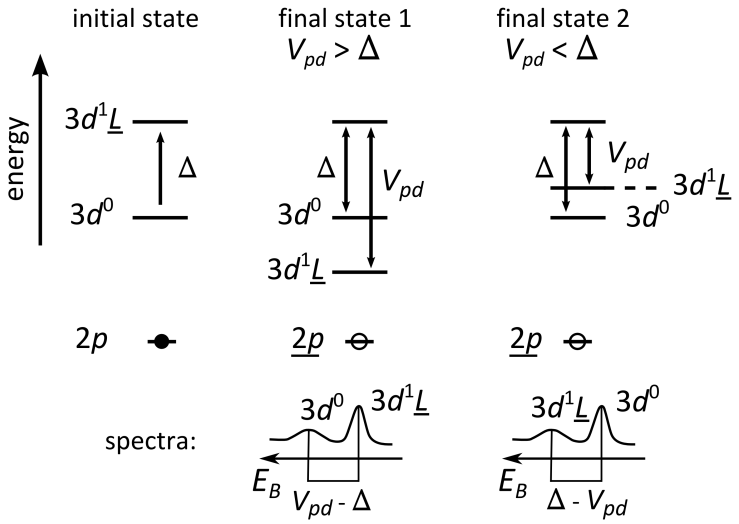

Figure 3.1: Illustration of the initial and the different final states of a $3d$-TM with the corresponding spectra in core-level spectroscopy adapted from [135].

3.3 Resonant PES

At an absorption threshold a resonant enhancement of the spectral weight of particular states in the photoemission spectra can be reached. PES at such an absorption edge is called resonant PES (resPES). Thereby, an additional two-electron process besides direct photoemission is involved. Here, resPES of the $3d$ conduction band at the L-edge (including mp^6 states where $m = 2$ or 3) is considered. The term for direct photoemission yields:

$$mp^6 3d^n + h\nu \rightarrow mp^6 3d^{n-1} + e^-(\epsilon), \tag{3.8}$$

where the excited electron has the kinetic energy $\epsilon = E_{kin}$. At photon energies which directly yield the specific energies in the absorption (here at the L-edge) electrons in the mp^6 core-level are excited into the $3d$ conduction band. The spectrum of a $2p^6 3d^0$ to $2p^5 3d^1$ excitation in Ti-based d^0-TMO, for instance, exhibits a characteristic multiplet structure [139]. This fact can be explained by the substantial crystal field splitting in the conduction band (see Subsection 2.1.1) and the spin-orbit split Ti $2p$ core-level. In the presence of absorption a second process is involved in resPES. This direct combination process is represented by the following steps:

$$mp^6 3d^n + h\nu \rightarrow \left[mp^5 3d^{n+1}\right]^* \rightarrow mp^6 3d^{n-1} + e^-(\epsilon), \tag{3.9}$$

Thereby, the excitation of a Ti mp core-level represents the first step [140]. From the

subsequent intermediate state $\left[\mathrm{m}p^5 3d^{n+1}\right]^*$ one $3d$ electron decays back to the Ti mp core-level (Auger decay). The resulting energy gain allows to excite a second $3d$ electron into the vacuum with the exact same energy ϵ as in the direct PES process. The complete resPES process is schematically depicted in Figure 3.2 [141].

In the absorption process of resPES the electron of the Ti mp core-level is actually lifted into the energetically higher $3d$-e_g state. The excited photoelectron, however, stems from a $3d$-t_2g conduction state by analogy with direct photoemission. Both channels interfere quantum mechanically so that above the optical threshold the spectral weight of Ti $3d$ states in resPES is enhanced [135, 141].

A similar consideration can be made for the O $2p$ valence states. The valence band in Ti-based d^0-TMO partly consists of Ti $3d$ states resulting from a finite overlap of Ti and O orbitals as discussed in Subsection 2.1.3. Under these circumstances an electron from a Ti mp core-level can be lifted into a $3d$-t_2g conduction state which, in the end, leads to an excitation of an O $2p$ valence electron in the subsequent Auger decay. The probability of this process, however, strongly depends on the band gap of the TMO.

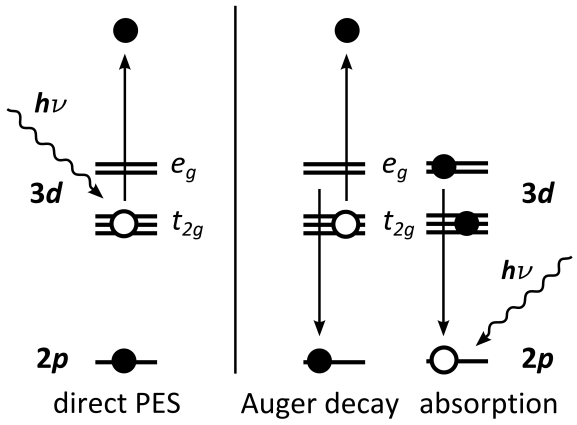

Figure 3.2: Scheme of resPES with its two channels. Direct PES (left) and the direct combination process in photoemission (right) both lead to the excitation of a $3d$ photoelectron. In the latter case (Auger-like decay) an electron from the $2p$ core-level is lifted in the $3d$ conduction band and its decay back to the Ti mp core hole allows to excite a second $3d$ electron into the vacuum (adapted from the Supplemental Material of [141]).

3.4 Angle-resolved PES

In the treatment of the PES process only the energetics of the involved (initial and final) states have been considered so far. The kinetic energy of an excited photoelectron considering the energy conservation yields: $E_{kin} = h\nu - \phi - E_\mathrm{B}$.

In addition to the kinetic energy of the photoelectron, angle-resolved PES (ARPES) allows to probe its momentum. By this method the actual band structure of a material might be reconstructed. This, however, requires the conservation in momentum of the N electron system [142]: $\boldsymbol{k}_f^N - \boldsymbol{k}_i^N = \boldsymbol{k}_{h\nu}$. ARPES is mainly conducted in the range

of ultraviolet radiation ($h\nu < 100\,\text{eV}$) where the photon momentum, in the order of $10^{-3}\,\text{Å}^{-1}$, can be neglected. In the case of an infinite crystal with a periodic potential the momentum $\boldsymbol{k}^N$ of a N electron system can be written as the crystal momentum $\boldsymbol{k}$. Then, the resulting momentum conservation $\boldsymbol{k}_f = \boldsymbol{k}_i$ implies that the optical transition of the photoelectron from an initial to a final state (as explained in Section 3.1) is "vertical" [135]. This picture in the reduced zone scheme can be transferred into the extended zone scheme so that: $\boldsymbol{k}_f = \boldsymbol{k}_i + \boldsymbol{G}$, where $\boldsymbol{G}$ represents a reciprocal lattice vector. The corresponding matrix element $M^k_{fi}(\boldsymbol{k}_i, \boldsymbol{k}_f)$ in the optical transition (described in Section 3.1) now depends on the momentum and solely contains the initial and final Bloch states within the crystal [135]. Figure 3.3 illustrates the individual wave vectors which are involved in the PES process.

An exclusive consideration of the optical excitation is only possible within the three-step model of PES [143, 144]. This model splits up the photoemission process into three parts so that the optical excitation, the travel of the photoelectron to the surface and its transmission through the surface are regarded as separate steps. Inelastic scattering of the photoelectron with other electrons or phonons in the crystal on its way to the surface result in a loss of energy and momentum information. This strongly restricts the information depth of photoemission which actually is described by the inelastic mean free path (IMFP) of electrons in a material (see Figure 3.5). A more realistic approach (which will not be discussed in detail) is represented by the one-step theory which treats a semi-infinite crystal. Thereby the final state is a so-called reversed LEED (low energy electron diffraction) state which is a damped state near the surface of the material [135, 145, 146].

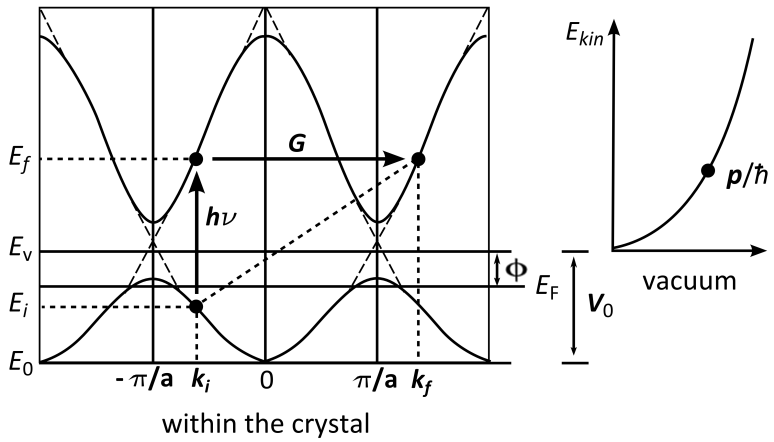

Figure 3.3: Schematic representation of the optical transition within the crystal (left) and of the free-electron final state in vacuum (right) including the wave vectors and the involved energies (adapted from [135]).

In ARPES the wave vector of the photoelectron is measured. Inside the crystal its momentum is defined by $\boldsymbol{K} = \boldsymbol{k}_i + \boldsymbol{G}$, in contrast to the crystal momentum $\boldsymbol{k}$. Outside the crystal the wave vector of the photoelectron is described by $\boldsymbol{K}_f = \boldsymbol{p}/\hbar$. Its three components along the Cartesian coordinates

$$
\begin{aligned}
K_x &= 1/\hbar\sqrt{2mE_{kin}}\, sin\vartheta\, cos\varphi \\
K_y &= 1/\hbar\sqrt{2mE_{kin}}\, sin\vartheta\, sin\varphi \\
K_z &= 1/\hbar\sqrt{2mE_{kin}}\, cos\vartheta
\end{aligned}
\tag{3.10}
$$

are defined by the polar (ϑ) and the azimuthal (φ) emission angle of the experiment. The corresponding components parallel ($\boldsymbol{K}_\parallel = \boldsymbol{K}_x + \boldsymbol{K}_y$) and perpendicular ($\boldsymbol{K}_\perp = \boldsymbol{K}_z$) to the surface result from Equation (3.10). In context of the three-step model the introduction of a surface (in the last step) has a severe implication on the momentum conservation. Due to the translational symmetry along the surface plane the parallel component of the momentum in- ($\boldsymbol{k}_\parallel$) and outside ($\boldsymbol{K}_\parallel$) of the crystal is conserved:

$$
\boldsymbol{k}_\parallel = \boldsymbol{K}_\parallel = 1/\hbar\sqrt{2mE_{kin}}\, sin\vartheta. \tag{3.11}
$$

On the other hand, the component perpendicular to the surface is not conserved anymore because of a surface potential step of depth $E_\mathrm{v} - E_0$. Thereby, E_v represents the vacuum level and E_0 the bottom of the valence band [135]. Different experimental methods have been developed in order to overcome the discrepancy of $\boldsymbol{K}_\perp$ and $\boldsymbol{k}_\perp$ [135]. Some of these approaches are able to accurately map the whole 3D band. However, they are quite complicated and demand a complementary experimental data set [135, 147, 148]. Another possibility is to approximate the photoelectron momentum by including an *inner potential* V_0 in the nearly-free-electron representation of the final state:

$$
\boldsymbol{k}_\perp = 1/\hbar\sqrt{2m\left(E_{kin}\, cos^2\vartheta + V_0\right)}, \tag{3.12}
$$

where $V_0 = |E_0| + \phi$. This latter approach, however, requires the knowledge of an appropriate *inner potential* V_0. V_0 can be either deduced from experiment data by considering the periodicity of $E(\boldsymbol{k}_\perp)$ over several BZ (tunable photon source) or from theory by the application of muffin tin potentials [142].

ARPES allows to illustrate the whole 3D band structure $E(\boldsymbol{k})$ of a material. On the one hand, the energy dispersion $E(\boldsymbol{k}_\perp)$ along $\boldsymbol{k}_\perp$ is determined experimentally by varying the photon energy $h\nu$ of the incident light. On the other hand, the parallel component $E(\boldsymbol{k}_\parallel)$ is acquired by the acceptance angle of the analyzer and by the rotational degrees of freedom of the manipulator (see experimental setup).

3.5 Reciprocal map of $BaTiO_3$

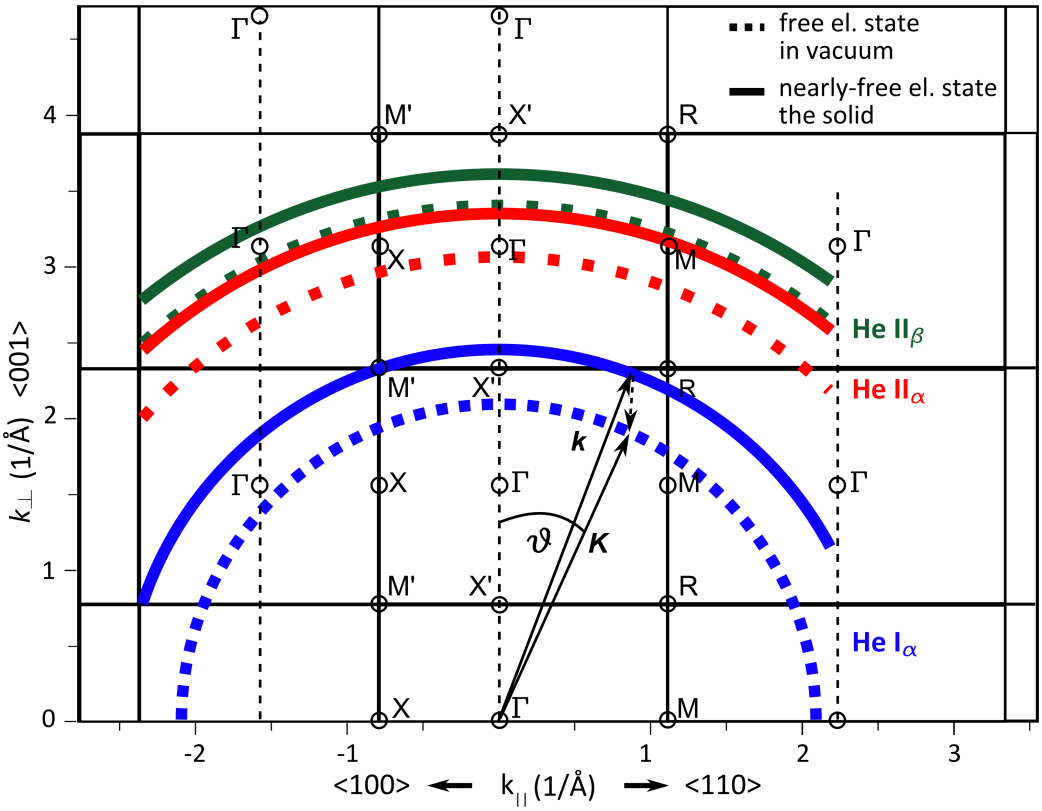

Figure 3.4: Reciprocal map of cubic BTO. The high-symmetry points of the cubic BZ along [1 0 0], [1 1 0] and [0 0 1] direction are depicted. Colored lines mark the maximal kinetic energy E_{kin} of photoelectrons excited by characteristic photon energies of a Helium discharge lamp (blue, red and green) with their corresponding momentum outside ($\boldsymbol{K}$, dotted hemisphere) and inside ($\boldsymbol{k}$, solid hemisphere) the solid.

The kinetics of the system including the individual components of the momentum (see previous section) can be nicely summarized in a reciprocal map. Figure 3.4 illustrates such a map for the material of interest, namely BTO. The high-symmetry points (Γ, X, M, X′, M′ and R) are depicted along the high-symmetry directions [1 0 0], [1 1 0] and [0 0 1] according to the cubic BZ of BTO (see Figure 2.3). Please note that at room temperature actually the tetragonal structure of BTO has to be considered. However, the change in the lattice parameter c and $\boldsymbol{k}_\perp = 2\pi/c$ is less than 1% [54]. The high-symmetry points Z and A of the tetragonal phase [149] are assigned to X′ and M′ in the reciprocal map of Figure 3.4, respectively, in order to distinguish them from the high-symmetry points in the Γ plane. In general, the reciprocal map of a material allows to visualize the momentum of the photoelectron in k-space which is probed by an

explicit photon energy. Here, the most prominent energies of a Helium discharge lamp which has been used in the home lab setup (see Section 3.7) are displayed: the blue, red and green lines represent the energies of He I_α ($h\nu = 21.22$ eV), He II_α ($h\nu = 40.84$ eV) and He II_β ($h\nu = 48.37$ eV), respectively. In order to obtain the perpendicular component of the momentum, an *inner potential* of $V_0 = 12$ eV is assumed (see Section 3.4) according to previous studies on STO [92, 150]. The momentum of the nearly-free electronic state inside the solid $\boldsymbol{k}$ (solid lines) can be deduced from the measured momentum $\boldsymbol{K}$ outside the crystal (dotted lines) in accordance to Equation (3.11) and (3.12). Note, that $\boldsymbol{K}$ itself is defined by the polar angle ϑ and the kinetic energy $\boldsymbol{E}_{kin}$ of the photoelectron.

3.6 Experimental conditions

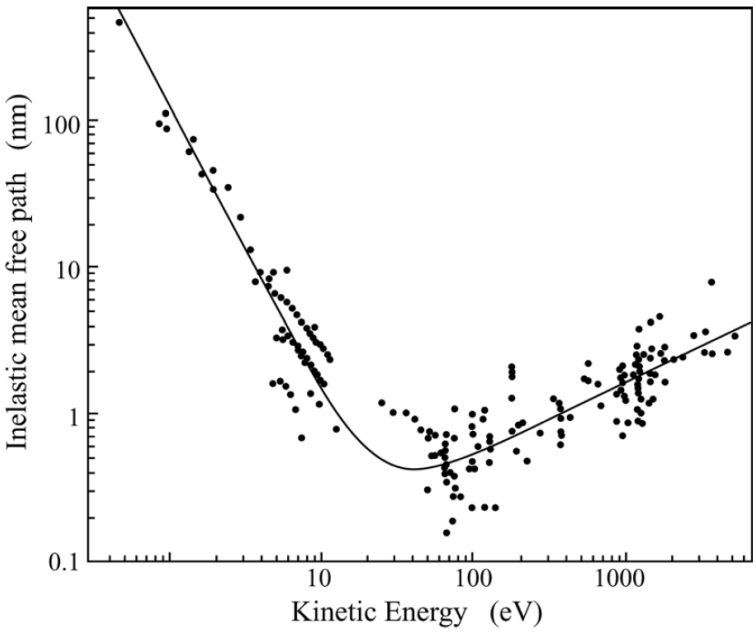

Figure 3.5: The dependence of the IMFP λ_m on the kinetic energy (black dots). Its slope can be simulated by an *universal curve* shown as a solid line taken from [136] (original version: Ref. [151]).

As the theoretical background of PES has already been discussed (see above), this section focuses on its practical realization. PES is a very surface-sensitive technique due to the limited IMFP of electrons in solids (see explanation of three-step-model in Section 3.4). This means that the excited photoelectron in the PES process is only able to penetrate through a certain amount of atomic layers (usually in the order of Å). In general, the IMFP of electrons in a material is mainly determined by electron-electron scattering and strongly depends on the kinetic energy of the electron [151]. In Figure 3.5 the IMFP λ_m in thickness (nm) is shown as a function of the kinetic energy for several different materials. Since the IMFP λ_m is almost independent on the investigated material (black dots) it can be described by an *universal curve* (solid

line). The function of the *universal curve* is experimentally derived and yields:

$$\lambda_{\mathrm{m}} = \frac{538}{E^2} + 0.41(aE)^{1/2}, \tag{3.13}$$

where E is the kinetic energy and a is the monolayer thickness (nm). The limited IMFP of the photoelectron in PES leads to the necessity of a clean surface in order to probe the sample itself and not unwanted adsorbates. Therefore, the experimental setup used in PES experiments is composed of a network of different **u**ltra **h**igh **v**acuum (UHV) chambers. The following two subsections describe in detail the two UHV setups which were used during this thesis.

3.7 Experimental setups

In general an ultra-high vacuum (UHV) network is preferably composed of at least of three chambers which are separated by valves: an entry chamber with a base pressure $p \approx 10^{-8}$ mbar, a preparation chamber ($p \approx 10^{-10}$ mbar) and a main chamber ($p \leq 10^{-10}$ mbar). In an entry chamber samples can be loaded in and out of the UHV. The preparation chamber allows to clean, grow and prepare the samples for the subsequent photoemission experiment. Since the preparation procedures differ for the individual samples, each preparation will be explained more explicitly in the next subsection. The actual photoemission experiments, however, take place in the main chamber. This centerpiece of each photoemission setup is, therefore, equipped with the photon sources and the analyzer. The sample movement within the UHV network is performed by a transfer system which is adjusted to the sample holder.

3.7.1 Home laboratory

Figure 3.6 schematically presents the PES setup in the home laboratory in Würzburg. In this setup a He gas discharge lamp (MB Scientific AB) and a X-ray tube, both with an attached monochromator, function as photon sources (green box). The excitation energies of the monochromatized He lamp are $h\nu = 21.22$ eV (He I_α), $h\nu = 23.09$ eV (He I_β), $h\nu = 40.84$ eV (He II_α), $h\nu = 48.37$ eV (He II_β) and, therefore, are in the region of ultraviolet (UV) light. In order to probe the core-levels of the material an additional monochromatized X-ray tube with an aluminum anode for Al-K_α excitation ($h\nu = 1486.6$ eV) is mounted to the chamber. The angle of incident light (from both light sources) and the surface normal has been chosen to be $\alpha = 54.7°$ (magic angle), so that the photocurrent does not depend on the angular momenta of the photoelectron wave function, the light polarization or the symmetry of the initial state but only on the

total cross section [135, 152]. The excited photoelectron e^- leaves the sample (orange) under the polar (ϑ) and the azimuthal (φ) emission angle and enters the transfer lens of the hemispherical analyzer (gray, Scienta R4000). By means of the lens system the electrons with a particular E_{kin} are focused onto the entrance slit and at the same time their velocity is adjusted (by retardation) to the pass energy E_P of the analyzer. Thereby, E_P yields [153]

$$E_P = \frac{eU}{R_2/R_1 - R_1/R_2} \tag{3.14}$$

and is defined by the applied voltage U and by the geometry of the hemisphere with radii R_1 and R_2. The kinetic energy E_{kin} and the emission angle of the photoelectrons are recorded simultaneously on the multichannel plate (MCP). Via a CCD camera at the backside of the MCP the data is transferred to the measuring computer where it is processed by the appropriate software (SES software). The instrumental energy resolution ΔE depends on specific dimensions of the analyzer and is roughly given by [153]

$$\Delta E \approx E_P \left(\frac{s}{2R}\right), \tag{3.15}$$

where s is the entrance slit width and $R = 1/2\,(R_1 + R_2)$. Hence, a lowering of the E_P leads to better resolution but also decreases the count rate in PES. The optimal corresponding angular resolution $\Delta\,\vartheta$ of the Scienta R4000 analyzer is 0.2° [153].

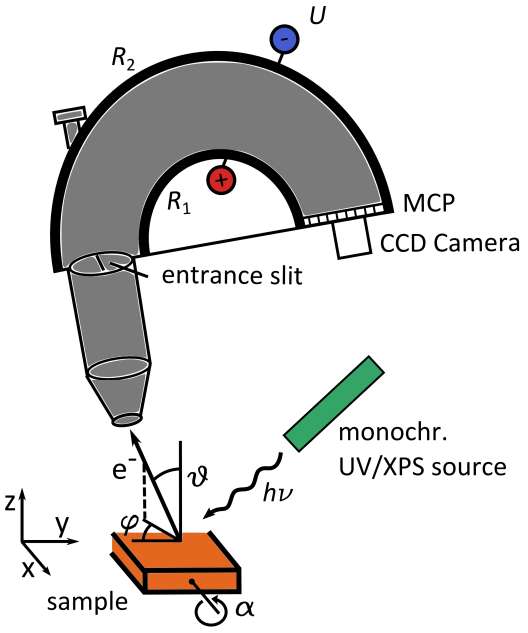

Figure 3.6: Schematic illustration of the PES setup installed in the laboratory in Würzburg with a R4000 analyzer.

Since the sample (orange) is put on a manipulator it can be adjusted along the three axis (x, y and z) and the rotational degree of freedom given by angle α. This helps to find the right focal point of analyzer, sample and light spot where the measured photocurrent is optimal. Furthermore, a rotation of the sample by the angle α in combination with the large acceptance angle (30°) of the analyzer (for Scienta R4000) allows to map a large area in the material's $k_{||}$-space. This is in accordance with Equation (3.10) and (3.11) where, besides E_{kin}, the polar (ϑ) and the azimuthal (φ) emission angle determine the respective k value. As the manipulator is linked to a cryostat with an open Helium circuit the sample can be cooled down to approximately 10 K in order to perform temperature dependent measurements or to reduce the thermal broadening.

3.7.2 Synchrotron facility

In a home laboratory the experimentalist is restricted to certain photon energies (light source) and light polarizations. The light from most of the commercially available photon sources is unpolarized. At a synchrotron, however, the photon energy can be varied over a large range and the polarization direction of the light can be changed. The first fact becomes important whenever the cross section of the investigated material changes drastically with the excitation energy. In addition, a continuous energy range allows to investigate resonant effects as *e.g.* at the L-edge of Ti (see Section 3.3). The light polarization, on the other hand, directly influences the one-electron dipole matrix element M_{fi}^{k} in Equation (3.5) [154]. As a result, electronic states in the band structure with distinct orbital character get either enhanced or reduced for a certain polarization.

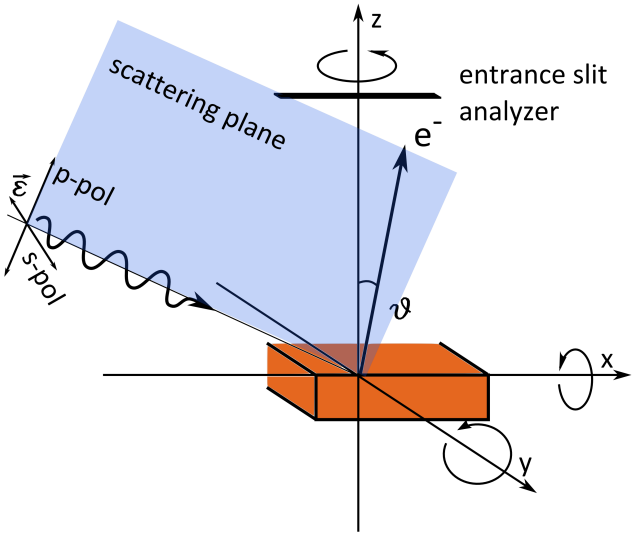

Figure 3.7: Sample geometry in the μARPES chamber at the ALS including the polarization vector of the light, the entrance slit of the analyzer and the corresponding scattering plane.

Due to these two facts a part of the experiments was performed at beamline 7 (BL7) of the Advanced Light Source (ALS) in Berkeley. This beamline provides photon energies between 20 – 1000 eV with a light polarization which can be changed from linear horizontal (LH), to circular (CP+, CP-) or to linear vertical (LV). In this setup thin films of BTO have been prepared in a pulsed laser deposition (PLD) chamber which additionally serves as a preparation chamber (see preparation section). The experiments were conducted in the μARPES main chamber where the spot size of the synchrotron light is in the range of 20 μm × 20 μm. The configuration of the ARPES experiment is in principle the same as the one shown in Figure 3.6. In view of the polarization of the light $\vec{\epsilon}$, however, it is important to consider the light's polarization vector with respect to the scattering plane of the experiment. The sample geometry and the scattering plane are clarified in Figure 3.7. The direction of the polarization vector $\vec{\epsilon}$ which lies in the scattering plane is referred to p-polarized (p-pol.) light and the vertical component as s-polarized (s-pol.) light. Furthermore, the manipulator of the μARPES chamber has two additional rotational degrees of freedom (around y- and z-axis) compared to the home lab system. In this synchrotron setup the temperature of the sample can be varied from 15 K up to 2300 K.

3.8 Sample preparation

Photoelectron spectroscopy is a powerful tool to investigate the material's band structure. As a consequence of the creation of photoelectrons in PES, however, the substrate is slightly positively charged. In the case of metals this depletion is balanced out by a careful grounding of the experimental setup so that a charging of the sample is prevented. Pure BTO, on the other hand, is a ceramic and exhibits insulating behavior even at elevated temperatures (≈ 400 K) [155]. Therefore, the preparation of BTO for PES is a delicate procedure since also the ferroelectricity of BTO strongly depends on the degree of doping [156, 157]. The aim of the preparation steps presented in the next subsections has been to maintain the ferroelectric behavior in BTO while considerably doping the system in order to be able to use PES.

3.8.1 $BaTiO_3$ single crystals

The first class of samples investigated in this thesis are $BaTiO_3$ single crystals (10mm × 10mm × 2mm) purchased from SurfaceNet. Their special shape (hat-shape) facilitates to mount the sample on the sample holder (Figure 3.8). In addition, the sample's polished surface (7mm × 7mm) represents the highest point in the experimental setup and not the clamps as otherwise. This particular feature ensures that the sample surface is not decontaminated from its surrounding while heating the

sample. A schematic picture of the sample and the sample holder system is given in Figure 3.8 (a) and (b).

The individual preparation steps consist of several cycles of sputtering and annealing (see Figure 3.8 (c)). First, the surface is bombarded by Ar^+ ions in order to clean the surface from adsorbates. Therefore, Ar gas which is let into the preparation chamber ($p_{Ar} = 5 \times 10^{-5}$ mbar) gets ionized and, then, is accelerated to the surface by means of a sputter gun working at voltages between $0.5 - 3$ keV. In the subsequent annealing process the sample is heated to high temperatures ($T \approx 800 - 1500$ K) to smoothen the surface again. These preparation steps also lead to the creation of oxygen vacancies (OV) at the surface of BTO. Their extent can be controlled by the sputtering voltage and the annealing temperature but also by a partial oxygen pressure p_{O_2} in the preparation chamber. In general, OV provide itinerant electrons to the host system (at least one) [34] which leads to a certain amount of doping of the initially insulating BTO substrate. This also means that depending on the preparation the doping level of BTO varies. Additionally, these vacant oxygen sites at the surface induce a large variety of surface reconstructions at the surface [158–160]. This might as well represent an advantage since the substrate can be tuned within these surface reconstructions. However, the reconstruction itself also affects the ferroelectric polarization of BTO [161, 162].

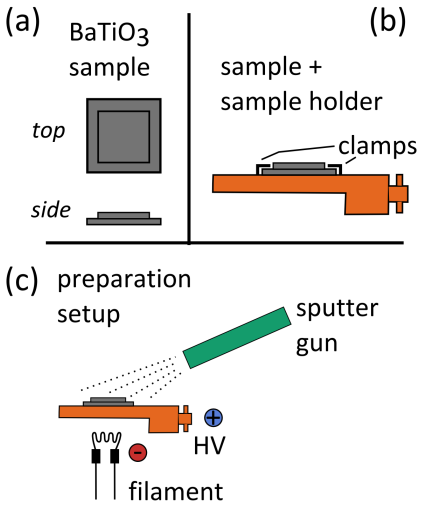

Figure 3.8: Illustration of the hat-shaped $BaTiO_3$ samples in (a), of their mounting on the sample holder in (b) and of the preparation setup in (c).

For our experiments at the home laboratory we prepared the BTO substrate according to Ref. [159] (1 keV acceleration voltage and $T \approx 1200$ K) in order to obtain a (2×1) reconstruction with a TiO_2 termination. In the same way a (1×1) surface reconstruction was prepared, however, by supplemental partial oxygen pressure $p_{O_2} \approx 10^{-6}$ mbar in the chamber. As the BTO crystal tend to break by passing the Curie tempera-

ture $T_C = 383\,K$ of the ferroelectric-paraelectric phase transition the BTO sample was carefully heated up to the required annealing temperature. Due to the minor reduction of the sample by OV the ferroelectric domains in BTO persist even after the preparation [163]. After each preparation the quality of surface was checked. Via low energy electron diffraction (LEED) it is possible to verify both surface reconstruction. Furthermore, a clean and smooth surface exhibits very sharp LEED spots without additional broadening. A possible decontamination of the surface with absorbents was monitored by means of XPS (investigating carbon C 1*s* peak). The corresponding results (LEED, XPS and ARPES) are described in Section 4.1.

3.8.2 Bi/$BaTiO_3$ hybrid system

The BTO substrates used in the hybrid system Bi/$BaTiO_3$ were prepared in the same manner as the pure BTO crystal (see previous subsection). In a subsequent step thin Bi films of variable thickness (2 – 12 ML) are deposited on the clean and freshly prepared substrate surface via a Knudsen cell. An accurate monitoring of the crucible's temperature in the evaporation process ensures a constant deposition of Bi with a rate of 0.1 ML/min. Prior literature designates the buckled Bi layer as a bilayer [121, 122] in this thesis, however, we utilize the term "monolayer" (ML). It it is more unambiguous with respect to penetration depths and inelastic mean free paths (IMFP). For a smooth and continuous film growth of constant thickness the Bi films were post-annealed to 350 K for 2 min since at this elaborate temperature the Bi atoms tend to thermally redistribute at the surface [164]. The surface alloy reconstruction of BiCu(111)($\sqrt{3} \times \sqrt{3}$) served as a model system to calibrate the evaporator [115]. As the lattice constants of Bi(0001) and BTO(001) fit almost perfectly along the substrate's [1 0 0] and [0 0 1] direction an epitaxial growth of the Bi films on BTO is assumed. The characterization of the surface structure of Bi/$BaTiO_3$ by LEED as well as the determination of the Bi layer thickness are presented in Section 6.1 in detail.

3.8.3 $BaTiO_3$ thin films

In contrast to the home lab experiments the measurements at BL 7 of the Advanced Light Source (ALS) were conducted on thin BTO films. By means of pulsed laser deposition (PLD) thin films of $BaTiO_3$ with a particular thickness are grown on (001) oriented 0.05 % Nb-doped $SrTiO_3$ substrates. The setup in the PLD chamber is schematically shown in Figure 3.9. In the PLD process a 248 nm Coherent Complex Pro 205 F Excimer Laser with a repetition rate of 1 Hz and a power of 150 mW bombards a rotating monocrystalline BTO target [24]. The generated BTO plasma deposits on the doped STO substrate which itself is glued on a molybdenum sample holder using silver

paste. During the whole growth process the sample holder is continuously heated up to a temperature of 700° C with a filament at the backside. The silver paste guarantees a good thermal and electrical contact between substrate and sample holder. In addition, the chamber is kept at a 1×10^{-4} mbar O_2 atmosphere mixed with ozone in order to compensates for most of the generated OV at the surface.

These growth parameters ensure an epitaxial growth of alternating TiO_2 and BaO layers [165]. The sample quality was monitored by means of *in situ* reflective high energy electron diffraction (RHEED) throughout the whole growth process. Based on the corresponding RHEED oscillations the thickness of the BTO films was determined. The RHEED results in combination with LEED and XPS allow to fairly well characterize the sample quality, termination, composition etc. (see Section 5.1).

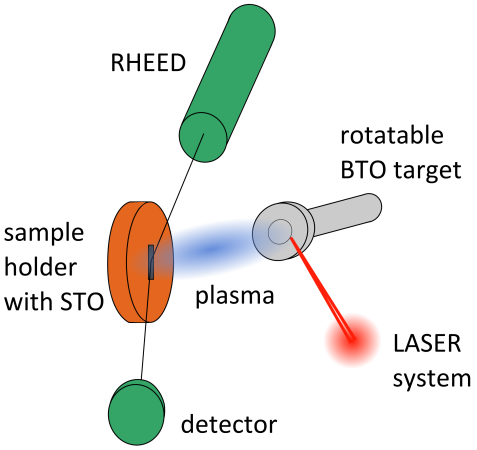

Figure 3.9: Schematic representation of the preparation chamber at BL 7 (ALS) with its PLD setup.

CHAPTER 4

ELECTRONIC STRUCTURE OF $BaTiO_3$: SINGLE CRYSTALS

Although the ferroelectric properties of BTO have been discovered more than 60 years ago [54] and it is known by recent calculations that an indication for ferroelectricity can be found in the valence band structure and valence band density of states [37, 72], there is a lack of experimental results on the electronic structure of BTO. Most of them focus on angle-integrated valence and core-level spectra [166, 167]. There are some additional resonant studies [168–170] but only one on the angle-resolved valence band [163]. This chapter gives an overview of the O $2p$ valence band of single crystalline BTO investigated by ARPES. The experimental findings are compared to recent band structure calculations [80] and to the optical gap of BTO [171]. A significant p - d hybridization of conduction and valence band states is found in the spectral weight of the valence band. Furthermore, the creation of OV at the surface of BTO influences the surface stoichiometry and affects the BTO valence band structure. As BTO deviates from a perfect d^0 system, correlation among Ti $3d$ states might arise. In the Ti $2p$ core-level spectra of BTO, indeed, clear indications for such a correlation is observed.

4.1 Surface structure of $BaTiO_3$ single crystals

The characterization of the surface structure of BTO concerning the terminating layer as well as possible surface reconstructions is crucial. For BTO there exist two possible surface terminations, either a BaO or a TiO_2 layer and several different surface reconstructions, namely, (1×1), (2×1), $c(2 \times 2)$, (2×2), etc. [158]. Since these

facts tremendously influence the electronic properties of the substrate [158–160] their behavior has to be clarified before analyzing the actual ARPES data. In addition, the level of defects in insulating BTO depends on the preparation treatment. It has already been shown that OV and itinerant electrons might have an impact on the ferroelectricity in BTO [156, 157].

After the sample preparation, which is explained in Subsection 3.8.1, the quality and the reconstruction of the individual BTO surfaces were examined via LEED. The LEED patterns of the two different preparations realized in this thesis are shown in Figure 4.1:

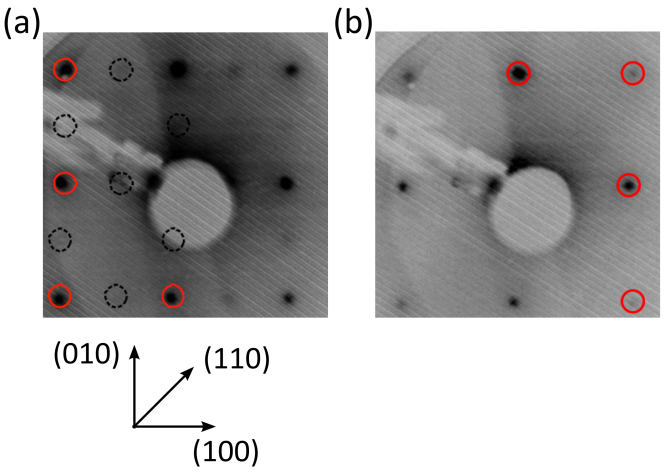

Figure 4.1: LEED patterns of two different $BaTiO_3$ surfaces measured at a beam energy of 39 eV. (a) The standard preparation leads to a (2×1) reconstruction and (b) additional annealing under O_2 atmosphere results in a (1×1) reconstruction.

The preparation of the BTO crystal via sputtering and annealing, following the protocol of Ref. [159], leads to a (2×1) reconstruction. The corresponding pattern is illustrated in Figure 4.1 (a), for a beam energy of 39 eV measured at room temperature. LEED, in general, depicts the reciprocal lattice of the surface geometry including the first 2 -3 unit cells. The red circles highlight the (10)-, (11)-, (01)-, etc. points of the reciprocal lattice which represent the centers of the BZ (Γ-points) in the extended zone scheme. Their distance is given by the reciprocal lattice vector $\boldsymbol{G} = 2\pi/a$, where a is the in-plane lattice constant of BTO. On the other hand, the characteristic diffraction spots of the (2×1) reconstruction are depicted by the black dotted circles. These spots appear along the [1 0 0]- as well as along the [0 1 0]-direction in the diffraction pattern. Thus, the surface structure consists of two different domains which are rotated by 90° with respect to each other. The same preparation, however, with an annealing at a partial oxygen pressure p_{O_2} results in a (1×1) reconstructed surface. The corresponding LEED pattern shown in Figure 4.1 (b) was acquired under the same conditions concerning temperature and beam energy as the (2×1) surface reconstruction in Figure 4.1 (a).

The width of the LEED spots, furthermore, give some indication about the surface

quality with respect to the surface roughness [172]. Due to the rather sharp (1 × 1) spots in the LEED patterns of both reconstructions, a clean and smooth BTO surface after the preparation can be assumed. However, in order to support this assumption additional XPS measurements on the individual BTO samples were conducted. The respective results provide further information on the surface quality and purity since XPS is able to detect possible contamination of the surface. By this method, moreover, the surface termination can be determined and an assumption regarding the doping level can be made. Figure 4.2 presents the XPS spectra of the crucial core-levels of BTO measured at a (2 × 1) surface reconstruction.

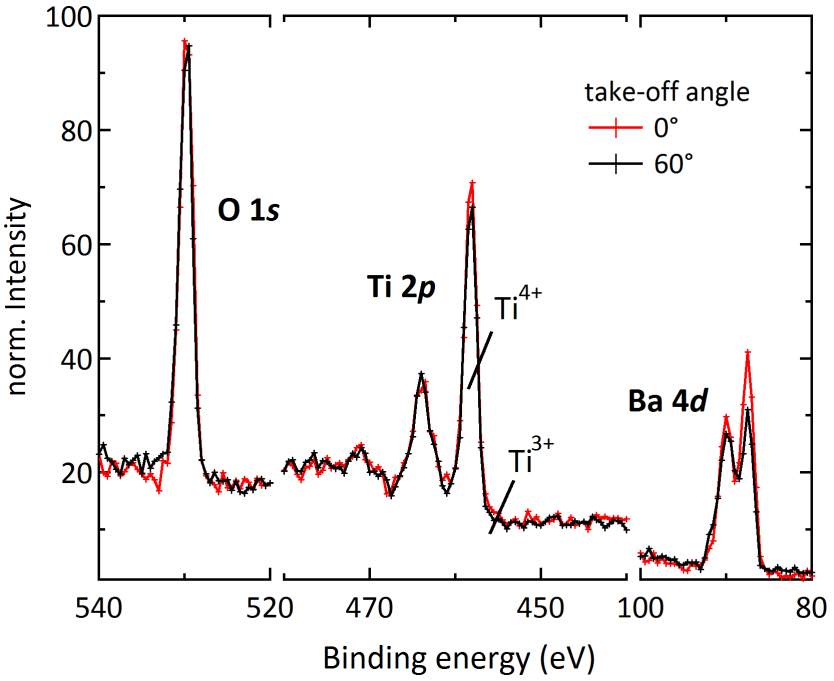

Figure 4.2: XPS spectra of the O 1*s*, Ti 2*p* and Ba 4*d* core-levels for the different take-off angles of 0° and 60°. The measurement was done with a Al-K_α excitation source at room temperature and the spectra are normalized to the background intensity.

The O 1*s*, Ti 2*p* and Ba 4*d* core-levels at two different take-off angles (0° and 60°), measured with an Al-K_α X-ray tube at room temperature, are displayed. Depending on the take-off angle of the XPS setup the probing depth of photoelectrons varies [173]. For higher take-off angles the measurement becomes more surface sensitive while spectral weight from deeper layers is reduced. The spectral weight of the O 1*s* and Ti 2*p* core-levels in Figure 4.2 stays almost unaltered upon changing the take-off angle from 0° to 60°. In contrast, the intensity of the Ba 4*d* core-level decreases by 20 %. As shown in Subsection 2.1.1 the BTO crystal can be regarded as a stack of alternating TiO_2 and BaO layers. Hence, the results of the angle-dependent XPS measurements suggest that the terminating surface layer is predominantly TiO_2.

In addition, the level of OV for a Ti-based d^0 TMO can be extracted from the ratio of the Ti^{3+} and Ti^{4+} signals of the Ti $2p_{3/2}$ core-level [174]. As the Ti^{3+} contribution at

the lower binding energy side in Figure 4.2 is vanishingly small, a moderate doping of the sample by the creation of OV might be assumed. By comparison to studies on STO [29, 161] including their sample preparation the carrier density in the sample can be estimated to be between $5 \cdot 10^{13}$ cm^{-2} and $1 \cdot 10^{14}$ cm^{-2}. This low electron concentration is related to a small amount of OV at the surface so that surface conductivity might be induced by band bending (Subsection 2.1.6). However, the ferroelectric behavior in bulk BTO is proposed to be maintained [156]. In all the XPS spectra no distinguishable C 1s signal was visible so that a strong contamination of the surface due to adsorbates can be excluded.

4.2 O 2p valence band

In the previous section we carefully characterized the single crystalline BTO surface in order to obtain a clean and smooth surface which allows a characterization of the BTO electronic structure by photoemission. The O 2p valence band of BTO can be found in an energy range of 3 eV to 9 eV below the Fermi level (E - E_F) as illustrated in the angle-integrated measurement of Figure 4.3:

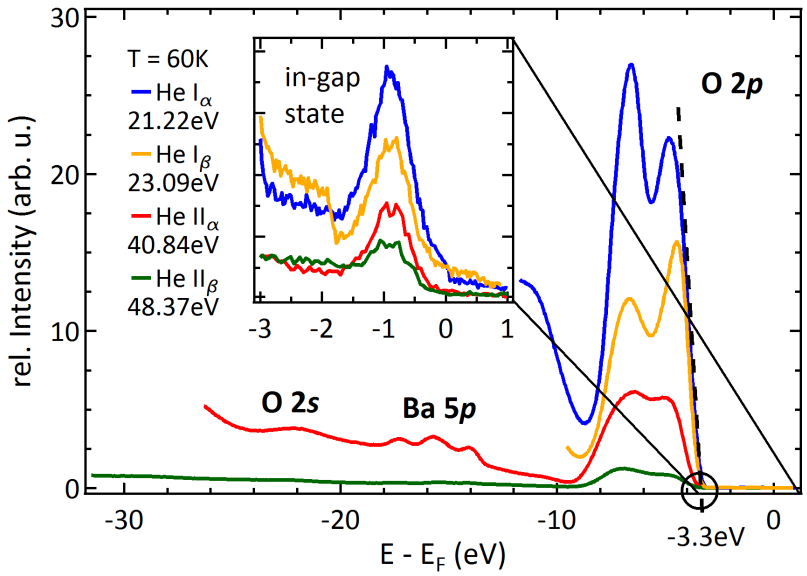

Figure 4.3: Angle-integrated valence spectra of $BaTiO_3$ for different excitation energies (He I$_\alpha$, He I$_\beta$, He II$_\alpha$ and He II$_\beta$). The dotted line represents the slope at the valence band maximum extrapolated from its steepest rise.

Undoped BTO is considered to be a regular band insulator when the correlation effects of the Ti 3d states are neglected. By extrapolating the slope of the valence band maximum (black dotted line) in Figure 4.3 the band-gap of BTO is estimated to a size of 3.3 eV indicated by the black circle. This value is in accordance to another PES study [168] and close to the value of 3.2 eV in optical-absorption measurements [171]. In addition to the valence band, the Ba 5p and O 2s core-levels are accessible with

higher excitation energies, namely He II_α and He II_β. Inside the band-gap of BTO an additional state at around 1 eV appears as shown in the inset. This state is connected to the creation of OV at the BTO surface and can be attributed to the bonding state introduced in Subsection 2.1.5 [34]. The microscopic origin and properties of this state will be further investigated in the context of the results presented in Chapter 5. The intensities of the spectra measured at different excitation energies in Figure 4.3 are not normalized with respect to each other. Their spectral weight, thus, reflects the change in intensity of the different Helium emission lines, where He I_α amounts to 88 % of the total intensity while the contribution of He II_β is only 0.5 % of the total intensity. In addition, the photoionization cross section for O $2p$ increases for smaller energies leading to a higher spectral weight in the photoemission spectra [175]. However, not only the overall intensity varies but also the shape of the valence band depends on the excitation energy as will be explained in detail in Subsection 4.2.3. In the following subsections different aspects of the O $2p$ valence band are investigated, *e.g.* its band structure is displayed and its spectral weight is discussed depending on the photon energy, the surface reconstruction as well as on temperature effects. Most of the measurements presented below were performed on a (2 × 1) reconstructed surface and are measured with the He II_α emission line at 60 K, unless stated otherwise.

4.2.1 Constant energy maps

Similar to the LEED experiment, constant energy maps allow to reveal the high-symmetry direction of the investigated BTO crystal. Therefore, individual ARPES measurements (k_x vs E - E_F), where k_x is directed along the analyzer slit, are extended to a 3-dimensional data set by continuously changing the polar angle (k_y). Constant energy maps represent cuts through this 3-dimensional data set (k_x, k_y and E - E_F) at constant energies E - E_F. From symmetries in the intensity distribution the high-symmetry points or directions can be determined.

In Figure 4.4 five of these constant energy maps (CEM) at certain energies within the valence band of BTO (at -8.4 eV, -6.8 eV, -5.6 eV, -5.0 eV and -4.1 eV) are displayed. CEM as well as the LEED pattern (previous chapter) reflect the symmetry of the BTO crystal and, thus, depict the high-symmetry directions. In the LEED experiment, however, the BTO crystal was rotated by 45° with respect to the geometry in the ARPES measurements so that the LEED patterns and the CEM can be directly compared by a rotation of 45°. Since the k directions in the CEM are not directed along high-symmetry directions they are referred to as k'_x and k'_y. The CEM at -8.4 eV in Figure 4.4 (a) suits best to highlight the cubic (1 × 1) surface BZ of BTO (dashed lines) and the corresponding high-symmetry points $\bar{\Gamma}$, $\bar{\mathrm{M}}$ and $\bar{\mathrm{X}}$. Furthermore, the colored lines depict the four high-symmetry lines oriented along the $\bar{\Gamma}$ - $\bar{\mathrm{X}}$ direction (yellow

and blue) and along the $\bar{\Gamma}$ - $\bar{\mathrm{M}}$ direction (red and green). The measurements shown in Figure 4.4 are performed at a temperature of 60 K where BTO is in its rhombohedral structural phase. The actual change of less than 2 % in the lattice constant are too small to be recognized by either LEED or ARPES [105]. For the following consideration concerning the electronic structure of the BTO valence band, hence, the cubic lattice parameters are considered. Particular distinctions between the different phases are stressed in Subsection 4.2.5.

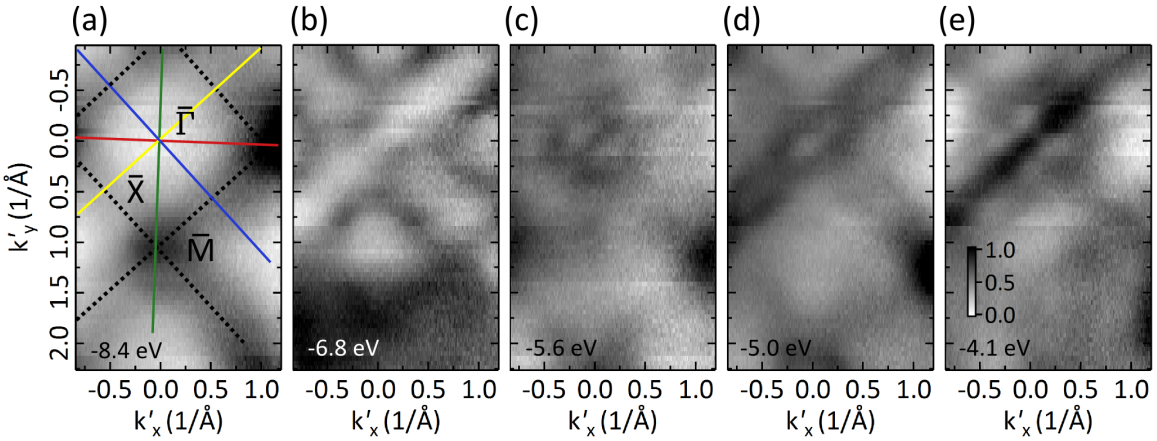

Figure 4.4: Constant energy maps at different energies (E - E_F) within the O 2p valence. (a) The high-symmetry points, the borders of the cubic (1 × 1) BZ (dashed lines) and the four different high-symmetry lines along $\bar{\Gamma}$ - $\bar{\mathrm{X}}$ direction (yellow and blue) and along $\bar{\Gamma}$ - $\bar{\mathrm{M}}$ direction (red and green) are presented. (e) The color scale for the normalized intensity (from low to high) is given.

From the CEM at -5.6 eV, -5.0 eV and -4.1 eV it becomes obvious that the spectral weight along two nominally equal high-symmetry directions differs. This becomes obvious in particular along the blue and yellow lines which reflect $\bar{\Gamma}$ - $\bar{\mathrm{X}}$ directions. The intensity variations in the CEM, in particular in Figure 4.4 (b) and (e), might be caused by the (2 × 1) surface reconstruction of BTO which results in a smaller tetragonal surface BZ. Thereby, the electronic states from higher surface BZ are backfolded into the first surface BZ and influence the intensity distribution within the CEM [176]. These variation in the electronic structure are more pronounced in the O 2p valence band which will be discussed in the next subsections.

Although there is a spectral signature of the (2 × 1) reconstruction it might be rather small. First, the BTO surface is composed of two domains which are rotated by 90° with respect to each other according to the LEED pattern presented in Section 4.1. Therefore, it can be assumed that also in ARPES the spectral weight of both domains

overlap and contribute to the total PES signal. Since both domains exhibit equal LEED intensity none of the two domains forms preferentially at the surface and, hence, is dominantly measured in ARPES. Second, the LEED spots of the (2 × 1) reconstruction are slightly suppressed in contrast to the (1 × 1) spots so that also in the ARPES maps, in general, the spectral features of the (2 × 1) reconstruction are supposed to be weaker.

In addition, matrix-element effects which occur due to the setup's geometry might affect the different intensity distributions in the CEM along nominally equal high symmetry directions [154]. Thereby, the symmetry of the specific O $2p$ orbital with respect to the scattering plane of the photoelectrons determines in the photocurrent even when the exciting light is unpolarized.

4.2.2 Band structure

In this subsection the band structure along the four high-symmetry directions is investigated in order to get further insight in the electronic structure of the valence band. The following ARPES data sets of BTO along specific high-symmetry directions ($k_{||}$ vs E - E_F) are extracted from the total 3-dimensional data set (k'_x, k'_y and E - E_F). A further processing of the data by means of a 2nd derivative method [177] is applied in order to distinguish individual spectral features within the valence band as they are subject to a experimental and intrinsic broadening, see Ref. [23, 163, 178].

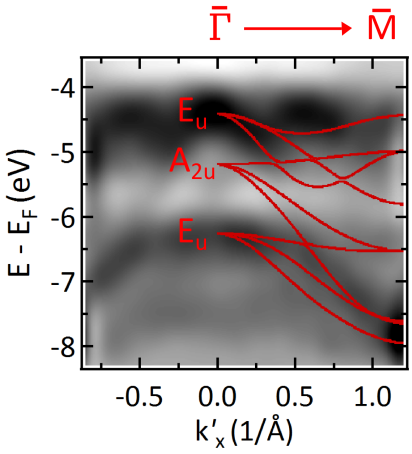

Figure 4.5: Comparison of experiment and theory for the O $2p$ valence band of BTO. The experimental data is extracted along the red line in the CEM of Figure 4.4 (a) measured with He II_α emission ($h\nu = 40.84$ eV) at $T = 60$ K. In order to enhance the visibility the band structure the experimental data is displayed by its 2nd derivative. The red lines represent band structure calculations for the high-symmetry directions $\bar{\Gamma}$ - $\bar{M}$ taken from Ref. [80]. The splitting of the O $2p$ energy bands is highlighted according to Subsection 2.1.3.

In Figure 4.5 the band structure of the valence band extracted along the red line in Figure 4.4 (a) is presented. At a photon energy of $h\nu = 40.84$ eV (He II_α) the photoemission hemisphere intersects the 3D BZ of BTO along the $\bar{\Gamma}$ - $\bar{M}$ direction, by assuming an *inner potential* of $V_0 = 12$ eV (see Figure 3.4). The experimental electronic structure

is superimposed by a theoretical band structure calculated for the $\bar{\Gamma}$-$\bar{\mathrm{M}}$ direction as displayed by red lines [80]. In order to allow a direct comparison of theory and experiment the calculation is shifted to the valence band maximum (VBM) of the ARPES measurement and adjusted to the experimental energy and momentum (in k'_x direction) scale. The splitting of the valence band into $\mathrm{E_u}$, $\mathrm{A_{2u}}$ and $\mathrm{E_u}$ by the axial crystalline field (see Subsection 2.1.3) as well as the dispersion of the bands towards the zone boundary are nicely resolved by the experiment (see Figure 4.5). In addition, the experimental data is in good agreement with the result of a recent band structure calculation [80], in particular close to normal emission ($k'_x = 0$).

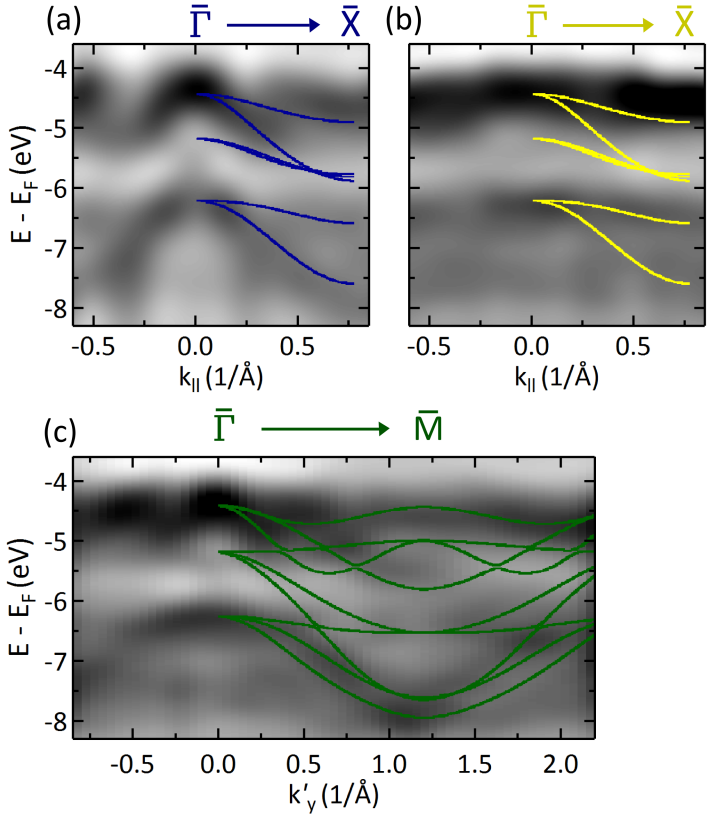

Figure 4.6: Calculated and experimental band structure of the BTO valence band along different high-symmetry directions. The 2nd derivative plots of the experimental spectra with the colored calculation correspond to the respective high-symmetry lines in Figure 4.4 (a) measured with He II_α emission ($h\nu = 40.84$ eV) at $T = 60$ K. The theoretical curves are adapted from Ref. [80].

An additional electronic feature which appears at the VBM in Figure 4.5 is not supported by theoretical band calculations [80, 81]. Its position in momentum space, $k'_x = 0.55\,\text{Å}^{-1}$, coincides with the surface BZ boundary at $k'_x = \sqrt{2}\pi/2a_{\mathrm{BTO}}$ of the (2×1) surface reconstruction along [1 1 0] where a_{BTO} is the lattice constant of BTO. This electronic feature, hence, might represent accumulated spectral weight at $k'_x = \sqrt{2}\pi/2a_{\mathrm{BTO}}$ which stems from backfolded bands due to the (2×1) surface reconstruction in BTO. The intensity contours in the CEM of Figure 4.4 (b) and (e) also indicate a backfolding of electronic states into the first surface BZ. This electronic feature might also be

related to surface contributions in the PES signal due to the termination layer (BaO or TiO_2) which will be discussed in detail in Subsection 4.2.4.

The band structure of the remaining high-symmetry directions (green, yellow and blue line) are illustrated in Figure 4.6. At the top, the experimental results extracted along the blue and the yellow line of Figure 4.5 (a) are compared to the theoretical calculation along the $\bar{\Gamma}$ - $\bar{\mathrm{X}}$ direction from Ref. [80]. Both experimental band structures display significant differences in their dispersion behavior. Whereas the electronic features of the O $2p$ valence band disperse along the blue line in Figure 4.6 (a) they are considerably more shallow along the yellow direction as displayed in Figure 4.6 (b). These differences in the spectral weight along both lines were already observed in the CEM of Figure 4.4. An explanation might be the suppression of particular electronic features in the PES process by geometry or spectral changes due to the (2×1) surface reconstruction in BTO.

The band structure in Figure 4.6 (c) which is extracted along the green line in Figure 4.5 (a) gives an overview of the O $2p$ band structure beyond the first (1×1) surface BZ. Although all the electronic features from the first BZ are nicely reflected in the second BZ they are slightly more faint and less pronounced.

4.2.3 Photon energy dependence

In this subsection the dependence of the valence band on the photon energy is investigated. At different photon energies the photoemission hemisphere cuts the BTO 3D BZ at different $\boldsymbol{k}_\perp$ values. As a consequence photoemission probes bulk electronic states at different position in the 3D k space as depicted in Figure 3.4. This is accompanied by a variation in the spectral weight measured in the experiment. 2D surface states, however, are not affected and show no dispersion as a function of photon energy.

The BTO O $2p$ valence band exhibits a change in its shape upon varying the excitation energy which has already been displayed in the angle-integrated spectra of BTO in Figure 4.3. Therefore, the character the O $2p$ valence band is expected to be bulk-like. In order to further characterize the valence band structure ARPES measurements along the red line of Figure 4.4 (a) are performed for He II_α, He II_β and He I_α excitation. The experimental results are depicted in Figure 4.7 (a), (b) and (c), respectively, whereas the red lines represents the corresponding theoretical band structure from Ref. [80].

PES measured with He II_α ($h\nu = 40.84\,\mathrm{eV}$) excitation probes the electronic structure near the $\bar{\Gamma}$ - $\bar{\mathrm{M}}$ direction and in the case of the He I_α line ($h\nu = 21.22\,\mathrm{eV}$) the $\bar{\mathrm{X}}'$ - $\bar{\mathrm{R}}$ direction is measured (see Figure 3.4). In the latter case of He I_α excitation a significantly smaller k'_x range is accessible by PES for the same experimental geom-

etry. This prevents a qualitative comparison with the theoretical band structure for $k'_x \geq 0.4\,\text{Å}^{-1}$. The He II$_\beta$ line lies within the BTO BZ and in the middle of the $\bar{\Gamma}$ - $\bar{\text{M}}$ and the $\bar{\text{X}}'$ - $\bar{\text{R}}$ direction. In Figure 4.7 (b), however, the spectral contribution is mainly determined to be along $\bar{\text{X}}'$ - $\bar{\text{R}}$ by comparison with the calculation. This observation suggests that the position of the He emission energies in the reciprocal map of BTO (see Figure 3.4) are at slightly higher $\boldsymbol{k}_\perp$ values so that the *inner potential* is actually larger than $V_0 = 12\,\text{eV}$. In total, the ARPES spectra in Figure 4.7 nicely resolve the valence band structure and the experimental band structure for all photon energies is fairly reproduced by the calculated electronic band structure along the different high-symmetry directions [80].

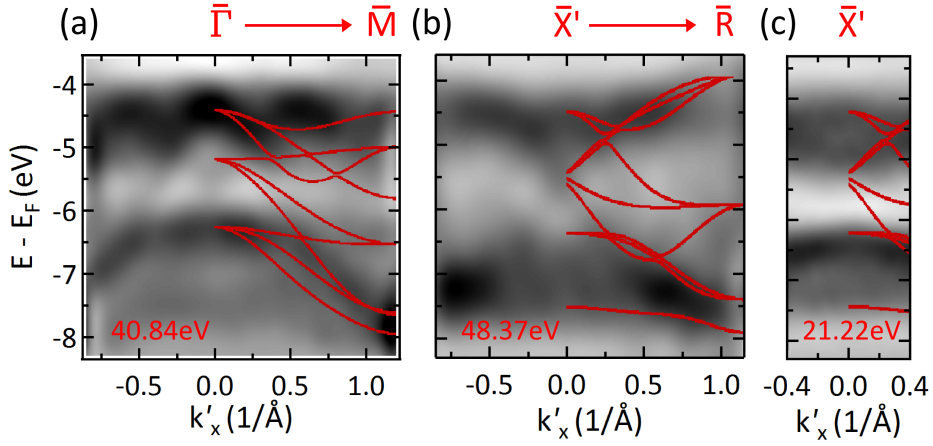

Figure 4.7: Photon energy dependence of the O 2p valence band of BTO along the red line in Figure 4.4 (a) measured with (a) He II$_\alpha$ ($h\nu = 40.84\,\text{eV}$), (b) He II$_\beta$ ($h\nu = 48.37\,\text{eV}$) and (c) He I$_\alpha$ ($h\nu = 21.22\,\text{eV}$) at $T = 60\,\text{K}$. The 2$^{\text{nd}}$ derivative plots of the experimental data is superimposed by the respective calculation adapted from Ref [80].

Another important aspect in the photon energy dependence of the BTO valence band is the Ti 3$p \rightarrow$ 3d absorption transition, presented in Equation (3.9), at a photon energy close to $\approx 38\,\text{eV}$ [168]. At photon energies which exceed a certain threshold an additional photoemission channel based on Auger decay contributes to the total spectral weight. This leads to an enhancement of Ti 3d states in the photoemission spectra of the O 2p valence band (see Section 3.3). ResPES experiments on BTO already demonstrated an increase in spectral weight at the higher binding energy side of the valence band [168–170] in accordance to similar findings for partial d DOS in electronic structure calculations [179, 180]. He II$_\beta$ with the excitation energy of $h\nu = 48.37\,\text{eV}$ is expected to lie above the threshold of the absorption transition [168, 170].

The measured band structure in Figure 4.7 (b), indeed, exhibits a strong enhancement in spectral weight between -6 eV$\leq E - E_F \leq$ -8 eV. However, in 2nd derivative plots the photoemission intensity can not be trusted quantitatively. Therefore, angle-integrated spectra for He II$_\alpha$ (red) and He II$_\beta$ (green) excitation are considered in Figure 4.8 (a). All spectra are normalized to the background and to the first maximum of the valence band (at around -4.9 eV). By increasing the photon energy above the absorption edge a crucial enhancement of the photoemission signal positioned around -7 eV occurs which is highlighted by the black arrow. Figure 4.8 (b) displays a resonant photoemission which has been integrated over the total O 2p valence band taken from Ref. [168]. The energy position of the He II$_\alpha$ line (red bar) is just before the strong increase of spectral weight due to the absorption transition, whereas He II$_\beta$ (green bar) is energetically located after the threshold.

This finding supplies some evidence for the existence of Ti 3d states in the spectral weight of the O 2p valence band. In addition, a p - d hybridization of valence and conduction states in BTO is suggested which is in accordance to electronic structure calculations [179, 180]. A similar observation has already been reported for the Ti 2$p \rightarrow$ 3d absorption edge in a resonant inelastic x-ray scattering (RIXS) experiment on BTO [181].

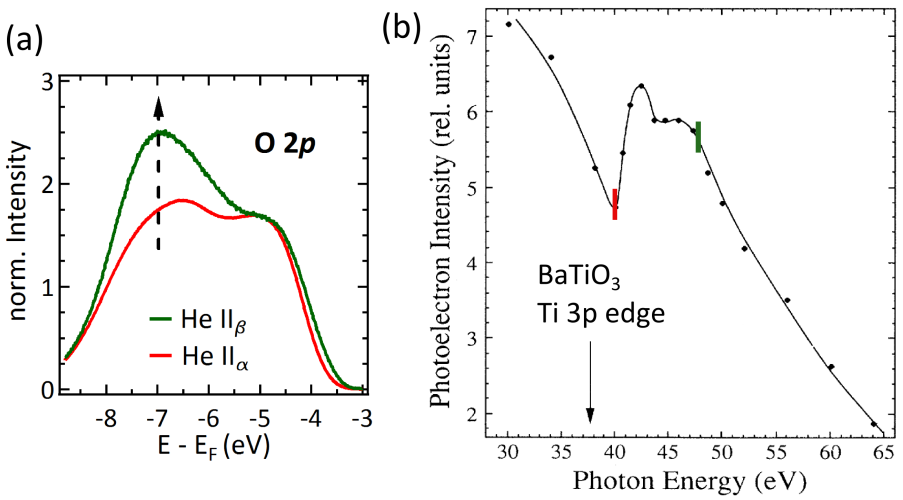

Figure 4.8: (a) Comparison of angle-integrated valence spectra of BTO for photon energies below (He II$_\alpha$ with $h\nu$ = 40.84 eV in red) and above (He II$_\beta$ with $h\nu$ = 48.37 eV in green) the absorption threshold. By varying the photon energy the intensity at the high binding energy side of the valence band varies significantly (black arrow). The spectra are normalized to the background intensity and to the respective spectral weight at E_F - 5 eV. (b) Photoemission intensity integrated over the O 2p valence band as a function of photon energy taken from Ref. [168]. The red and green bar mark the energy position of the He II$_\alpha$ and He II$_\beta$ line.

4.2.4 Different surface reconstruction

The data and spectra discussed in the previous subsections address only (2 × 1) surface reconstructions prepared by sputtering and annealing cycles. A subsequent annealing under partial oxygen pressure, however, leads to a (1 × 1) reconstructed surface as verified by LEED (see Figure 4.1). These surfaces also exhibit distinct differences in spectral weight.

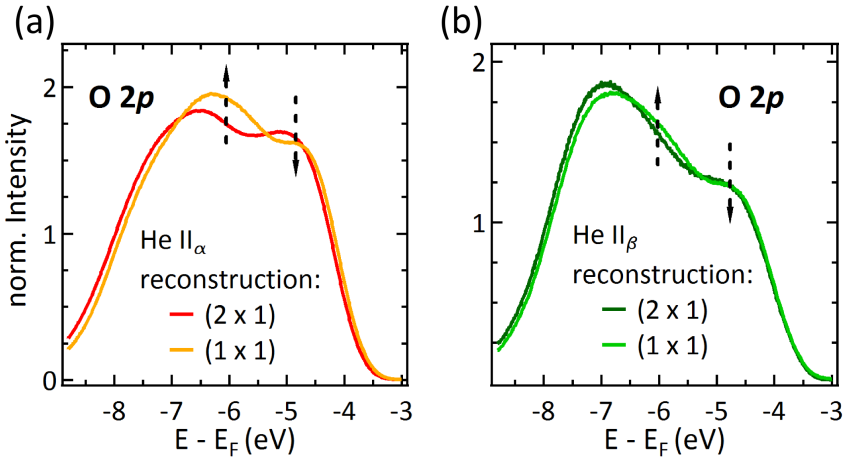

Figure 4.9: Changes in the spectral weight of the BTO valence band due to different surface reconstructions. In (a) and (b) the angle-integrated photoemission spectra for (2 × 1) and (1 × 1) reconstructed surfaces are compared directly for He II$_\alpha$ and He II$_\beta$ excitation, respectively. The data was measured at $T = 60$ K and the spectral changes are highlighted by black arrows. All spectra are normalized to the background intensity.

In Figure 4.9 (a) and (b) the integrated spectral weight for the (1 × 1) surface is compared with the (2 × 1) surface for He II$_\alpha$ and He II$_\beta$ excitation. The spectra of the (1 × 1) reconstruction is shifted by ≈ 70 meV towards higher E - E_F with respect to the spectra of the (2 × 1) surface reconstruction. The partial oxygen pressure in the preparation of the (1 × 1) reconstruction partly heals out OV and leads to a smaller OV concentration at the BTO surface [93, 182]. As a result, the band bending at the surface is narrowed and the accompanied shifting of the core-levels is reduced (see Subsection 2.1.6). These effects are studied in more detail in Chapter 5 for thin BTO films.

In addition to a change in the defect concentration, a transfer of spectral weight from the high-energy side of the valence band (-5 eV≤ E - E_F ≤ -4 eV), for a (2 × 1) reconstruction, to the middle of the valence band at ≈ E_F - 6 eV, for a (1 × 1) reconstruction, is observed. This finding is illustrated by black arrows highlighting the increase and

decrease of spectral weight. While the O $2p$ spectral weight is changing, the in-gap state at $\approx E_F$ - 1 eV is almost not affected (not shown). Different surface terminations in BTO (BaO or TiO_2) depending on the sample preparation and the corresponding surface reconstructions might alter the electronic structure of BTO. Band structure calculations which consider surface effects [183, 184], indeed, state that different surface terminations induce surface states at different energy positions in the spectra. For a BaO-termination surface states appear in the middle of the valence band whereas a TiO_2 termination shows the respective surface features at the VBM [184]. By comparison with our results, it might be assumed that the (1 × 1) surface is mainly BaO-terminated and the (2 × 1) surface mainly TiO_2-terminated. Already the XPS spectra discussed in connection with Fig 4.2 exhibit a TiO_2-termination for the (2 × 1)-reconstructed surface. In general, the most stable and prominent phase for a BaO terminated surface in BTO is the (1 × 1) reconstruction while the TiO_2 termination displays several different phases according to theoretical surface phase diagrams [161, 162].

A direct comparison for the band structure of both terminations is shown in Figure 4.10 measured for He II_α excitation:

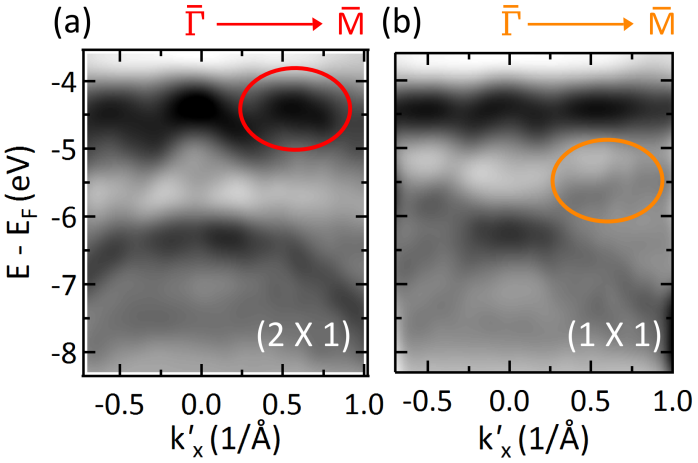

Figure 4.10: 2nd derivative plot of the O $2p$ valence band structure measured with He II_α emission and $T = 60$ K at a (2 × 1) and a (1 × 1) surface reconstruction presented in (a) and (b), respectively. The red and orange ellipses mark the areas where additional spectral weight for the corresponding reconstructions appears.

The (2 × 1) reconstruction in Figure 4.10 (a) exhibits a pronounced electronic feature at the VBM highlighted by the red ellipse which is absent in the measurement of the (2 × 1) reconstructed surface. On the other hand, the (1 × 1) surface reconstruction in Figure 4.10 (b) displays an additional spectral feature at around $E - E_F \approx$ -4.5 eV (orange ellipse). Thus, the difference in spectral weight observed in Figure 4.9 can be directly related to the appearance or absence of surface electronic features in Figure 4.10.

4.2.5 Temperature dependence

The material BTO is still the subject of extensive research since it displays ferroelectricity at room temperature [37] as well as various structural phase transitions [103]. Therefore, a change in the electronic structure, for instance a difference in the magnitude of spectral weight or shape, is expected when the temperature of the sample passes through a particular transition [185].

In Figure 4.11 (a) and (b) angle-integrated photoemission spectra of the valence band are presented as a function of temperature:

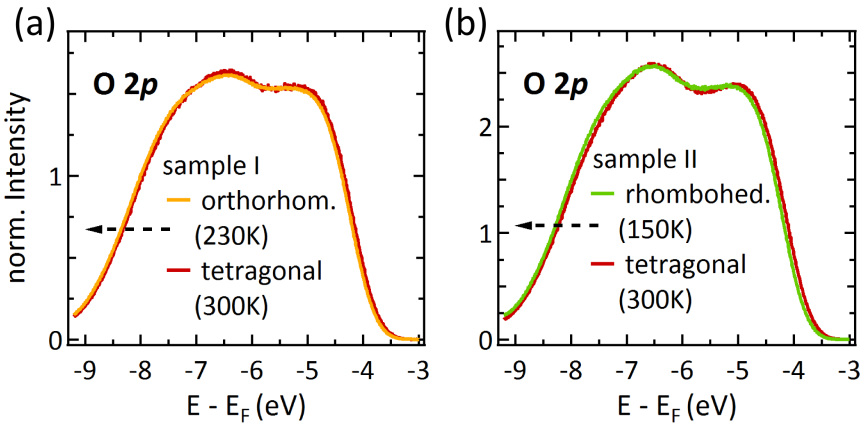

Figure 4.11: Temperature effects on the BTO valence band investigated with He II$_\alpha$ excitation ($h\nu = 40.84$ eV). The valence band shifts towards lower E - E_F by decreasing the temperature from 300 K to 230 K (orthorhombic phase of BTO) in (a) or from 300 K to 150 K (rhombohedral phase of BTO) in (b). All spectra are normalized to the background intensity.

The BTO samples (I and II) employed in the photoemission data shown in Figure 4.11 (a) and (b) were prepared at different days so that their spectral shape slightly varies. In order to exclude variations in the photoemission signal due to slightly different sample surfaces each spectra in the low temperature phase was directly compared to the data for the tetragonal phase measured subsequently. Figure 4.11 (a) displays the spectral weight of the valence band measured at room temperature (tetragonal phase) and at 230 K (orthorhombic phase) whereas Figure 4.11 (b) shows the angel-integrated spectra for the tetragonal phase and the rhombohedral phase measured at room temperature and at 150 K, respectively. In the angle-integrated spectra as well as in the band structure (not shown) no crucial differences are observed. The decrease in temperature, however, gives rise to a small shift of the total spectra towards lower E - E_F (Δ E $\approx$ 60 meV for 300 K $\rightarrow$ 150 K) indicated by the black arrows. This shift is not related to the different structural phases, but it is rather a general consequence of

OV diffusion in BTO and due to changes in the defect concentration at its surface. A similar effect is detected when the sample is annealed under partial oxygen pressure which also leads to a change in the number of OV at the surface. In this case, however, the spectra are shifted towards higher E - E_F. A detailed description of OV on the surface of BTO and its implications for the electronic structure are given in Chapter 5 for thin BTO films.

4.3 Ti 2p core-level studies

The 2p core-level of 3d TMO, in general, contains information on certain parameters that are relevant in the description of a Mott-Hubbard and a charge transfer insulator [88, 89]. In particular, the Coulomb energy U, the charge transfer energy Δ and the hybridization strength ($pd\sigma$) can be extracted by comparing a cluster model calculation with experimental 2p core-level spectra [88]. The configuration-interaction cluster model is fitted to a measured XPS spectra and convoluted with an extrinsic inelastic loss background as determined by EELS (electron energy loss spectroscopy) for better comparison. The best fitting results yield the values of U, Δ and ($pd\sigma$) within the cluster model.

By means of this model the respective values of two nominally d^0 TMO, namely TiO_2 and STO, were already determined in a combined theoretical and experimental study demonstrated in Ref. [89]. A similar consideration for BTO, however, is lacking. In the following an indirect and qualitative evaluation of the Ti 2p core-level spectra of BTO is demonstrated by considering the experimental and theoretical results of TiO_2 and STO.

Figure 4.12 compares the Ti 2p core-level spectra of single crystalline BTO measured with an Al-K_α source ($h\nu$ = 1486.6 eV) at room temperature (green) to the calculated spectra of TiO_2 (orange) and STO (red) taken from [89]. All spectra are plotted with respect to the energy position of the Ti $2p_{3/2}$ core-level. In the BTO spectra a linear background was subtracted. The Ti $2p_{1/2}$ spin-orbit peak position is not shifting in energy among TiO_2, STO and BTO which proves that the spin-orbit splitting is almost the same for the different TMO. This is in contrast to the energy positions of the satellite peaks which slightly vary for TiO_2, STO and BTO. In addition, the satellite peak structure in BTO does not seem to be determined by a single Voigt peak. EELS measurements on the STO sample in Ref. [89], indeed, reveal that the structure of the satellite peaks in the XPS core-levels is actually given by a superposition of two loss features A and B for each individual Ti $2p_{1/2}$ and the Ti $2p_{3/2}$ spin-orbit peak. In the case of this qualitative study, however, it is sufficient to compare the main intensities in the satellite peaks. This concept has already been successfully

demonstrated in the combined theoretical and experimental study of Ref. [89].

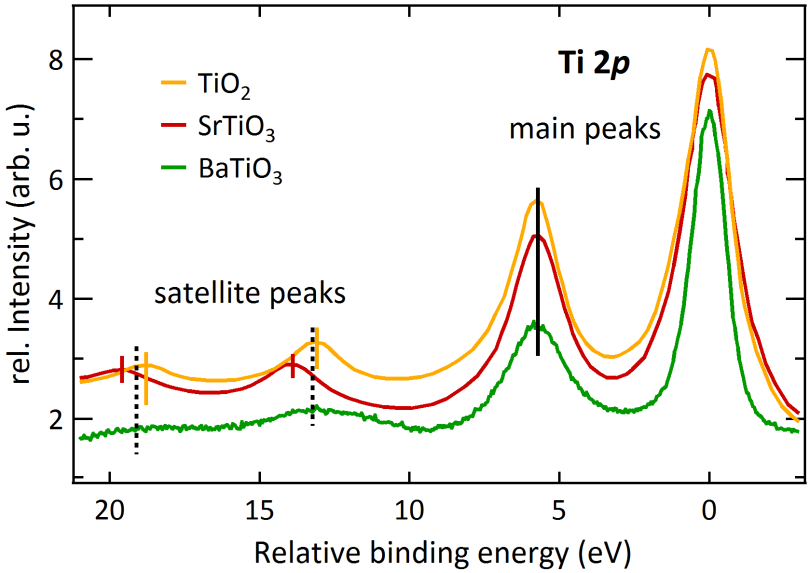

Figure 4.12: The 2p core-level of BTO (green) is compared to the results for TiO_2 (orange) and STO (red) from a cluster model calculation taken from [88].

Before interpreting this phenomenon it is crucial to recall the origin of this characteristic satellite structure (see Section 3.2). In the presence of an orbital overlap of the O 2p (ligand) and the Ti 3d states and strong p-d hybridization [137, 138] an additional electronic state with $3d^1\underline{L}$ configuration appears in the photoemission spectrum. The ground state in this approach is given by a linear combination of $3d^0$, $3d^1\underline{L}$, $3d^2\underline{L}^2$, ..., $3d^n\underline{L}^n$ configurations.

This ansatz is also applied in the cluster model for calculating the core-level spectra of TiO_2 and STO. Thereby, configurations up to the 5th order are taken into account to obtain reliable results [89]. According to Ref. [89] the energy shifts of the satellite peaks observed in the TiO_2 and STO spectra are only determined by the hybridization strength ($pd\sigma$). From the cluster model calculation the values of $pd\sigma$ are estimated to be 2.60 ± 0.1 and 2.43 ± 0.1 eV for TiO_2 and STO, respectively. All other input parameters for TiO_2 and STO remain unchanged, namely, $U = 4.5 \pm 0.5$ eV, $\Delta = 4.0 \pm 2$ eV and the Ti 3d occupation number is $n_d = 1.1 \pm 0.2$ (see Ref. [89]).

The energy position of the satellite peaks in BTO are in between the ones of TiO_2 and STO. Therefore, it can be concluded that for BTO the hybridization strength is between the theoretical values for TiO_2 and STO: $2.43\,\text{eV} \leq (pd\sigma)_{\text{BTO}} \leq 2.60\,\text{eV}$ [89]. In contrast, the values of U, Δ and n_d are proposed to not change for TiO_2 and STO [89], so that also in BTO they are expected to stay the same. The value for the Ti 3d occupation number $n_d = 1.1$, indeed, agrees fairly well with recent electronic structure calculations [71, 80]. Hence, these results suggest that BTO, as STO and TiO_2, is in the intermediate region (near $U = \Delta$) of the *Zaanen-Sawatzky-Allen* phase diagram

[87]. Other theoretical work proposes that STO and TiO_2 are rather charge transfer insulators than Mott-Hubbard insulators [186] which also puts BTO in the charge transfer regime of the *Zaanen-Sawatzky-Allen* phase diagram.

CHAPTER 5

ELECTRONIC STRUCTURE OF $BaTiO_3$: THIN FILMS

A transition from bulk $BaTiO_3$ to thin film systems by continuously decreasing the size of the crystal weakens the ferroelectricity in $BaTiO_3$ but the ferroelectric polarization, in general, is retained [187]. Strain in thin film systems tend to influence the ferroelectric properties [43] and even lead to an enhancement of the remanent polarization [44]. Therefore, $BaTiO_3$ thin films are of growing interest, in particular, since the film growth can be nicely controlled by PLD under oxygen atmosphere [165]. This chapter addresses the surface and electronic structure of $BaTiO_3$ thin films. Due to the creation of OV at the surface of BTO a quasi-particle state and a incoherent spectral contribution in the vicinity of the Fermi level are observed. Both electronic states are characterized by means of photon energy, light polarization, partial oxygen pressure and temperature. In addition, a schematic model is proposed which correlates the appearance of the electronic states to the formation of OV at the surface. The depletion and accumulation of charge carriers at the surface could be controlled by temperature and partial oxygen pressure [188].

5.1 Surface structure of $BaTiO_3$ thin films on $SrTiO_3$

In contrast to the commercially available BTO single crystals the BTO thin films on a Nb-doped (0.05%) STO substrate are directly prepared in a separated UHV chamber through PLD (see Subsection 3.7.3) by following the preparation protocol of Ref. [165]. The lattice constants of the STO substrate ($a_{STO} = 3.905$ Å) and the BTO films ($a_{BTO} = 3.994$ Å) agree fairly well so that only a slight lattice mismatch at the

interface during growth is expected. According to a growth study the preparation via PLD, indeed, leads to a layer-by-layer growth (alternating TiO_2 and BaO layers) of the BTO films as long as the critical thickness of 12 unit cells (u.c.) is not exceeded [189]. The surface of thin BTO films during and after growth has already been extensively studied in literature by RHEED [190] and LEED [191]. In Figure 5.1 the characteristics of the prepared BTO films are shown:

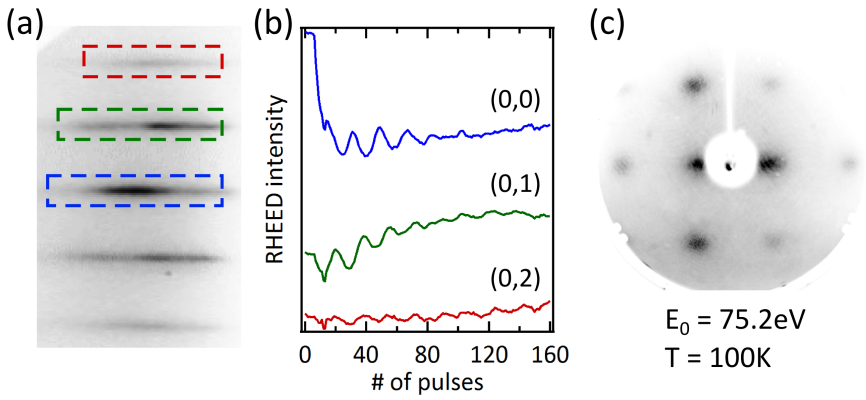

Figure 5.1: Characterization of the $BaTiO_3$ films grown on $SrTiO_3$ via PLD. (a) Final RHEED image after the growth of 8 unit cells. (b) Intensity variation of the (0,0), (0,1) and (0,2) RHEED reflections indicated by the respective colors. (c) LEED image of the $BaTiO_3$(001) films measured at $E_0 = 75.2$ eV and $T = 100$ K.

From the number of RHEED oscillation $n = 8$ the thickness of the BTO films is deduced to 8 u.c consisting of 4 TiO_2 and BaO layers illustrated in Figure 5.1 (b). A damping in the oscillations after 4 u.c. is attributed to a certain amount of strain due to the slight difference in the lattice constants a_{BTO} and a_{STO} of BTO and STO. It has already been shown that at low thicknesses of 1.6 nm the BTO films tend to grow quasi-pseudomorphic to STO, *i.e.* with the bulk tetragonal c values of STO [56]. At higher thicknesses the in-plane lattice parameters of the BTO films, however, approach the BTO bulk values ($a_{BTO} = 3.994$ Å, $c_{BTO} = 4.0335$ Å) [56, 105]. The strong reflections in the RHEED and LEED patterns in Figure 5.2 a) and c), respectively, suggest a rather high film quality with a 1×1 reconstruction at the surface of BTO.

XPS spectra give indication of the chemical composition of the BTO films. In Figure 5.2 all relevant core-levels of BTO until a binding energy of 145 eV are presented [169]. No traces of STO in the form of the prominent Sr $3d$ states, where the cross section is by one magnitude higher than for Ba $4d$ and Ti $3p$ [175], are observed (see black dotted box). The BTO films, hence, are expected to grow in thick enough closed layers in order to not unveil the STO substrate. According to the RHEED

oscillations the terminating layer during the growth is assumed to be BaO. This fact is further supported by the 1×1 reconstruction in LEED which is most stable for a BaO termination [158, 161, 162]. In addition, the Ba $4d$ core-levels exhibit side-peaks at higher binding energies which have been attributed to under coordinated Ba at the surface (see inset of Figure 5.2) [169].

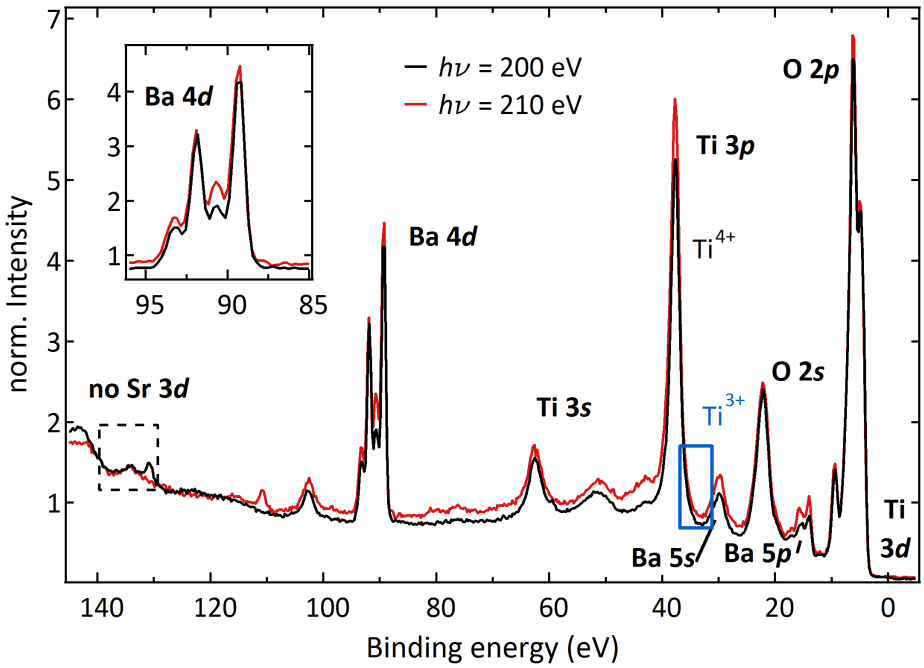

Figure 5.2: XPS spectra of the BTO films on Nb doped STO measured at the photon energies of 200 and 210 eV and at a temperature of $T = 100$ K. No traces of STO are identified in the spectra (black dotted box) so that exclusively signatures of BTO are detected by PES. The inset shows a close-up scan of the Ba $4d$ states. All spectra are normalized to the background intensity.

In addition, the Ti^{3+} shoulder at the lower binding energy side of the Ti $3p$ states (blue box) in Figure 5.2 is clearly suppressed. From the ratio of Ti^{4+} and Ti^{3+} states in the XPS spectra the carrier density can be deduced [174]. This suggests a considerable low carrier density in the BTO films which is related to a low OV concentration at the surface. Similar investigations on the carrier concentration of a Ti-based TMO have been conducted at the Ti $2p$ and Ti $3p$ core-level of BTO and STO, respectively [93, 163]. In general, the carrier concentration considerably affects the electronic structure in oxide materials, in particular, the electronic states near the surface of STO [29, 192]. This fact will be studied in more detail at the end of this chapter.

At photon energies above 40 eV and at high intensities of the photon beam the

illumination of oxide materials, in particular titanates, with light leads to the creation of OV at its surface [24, 182, 193]. This leads to a creation of itinerant electrons at the surface of the thin films so that no further preparation is required, in contrast to the preparation of the BTO single where several cycles of sputtering and annealing reduce the sample surface (see Subsection 3.8.1).

5.2 O 2*p* valence band

According to the characterization of the surface structure in the previous section the BTO thin films with a thickness of 8 u.c. mainly display a lattice constant close the BTO bulk value in X-ray diffraction [56]. In order to confirm a bulk-like behavior of the BTO films the O 2*p* valence band is investigated and compared to band structure calculations of bulk BTO [80, 81].

Figure 5.3 illustrates the valence band structure of BTO in the form of angle-integrated spectra around the $\bar{X}'$-point and constant energy maps (CEM) at particular energies E - E_F measured at $T = 300$ K with a photon energy of $h\nu = 100$ eV and p-polarized light:

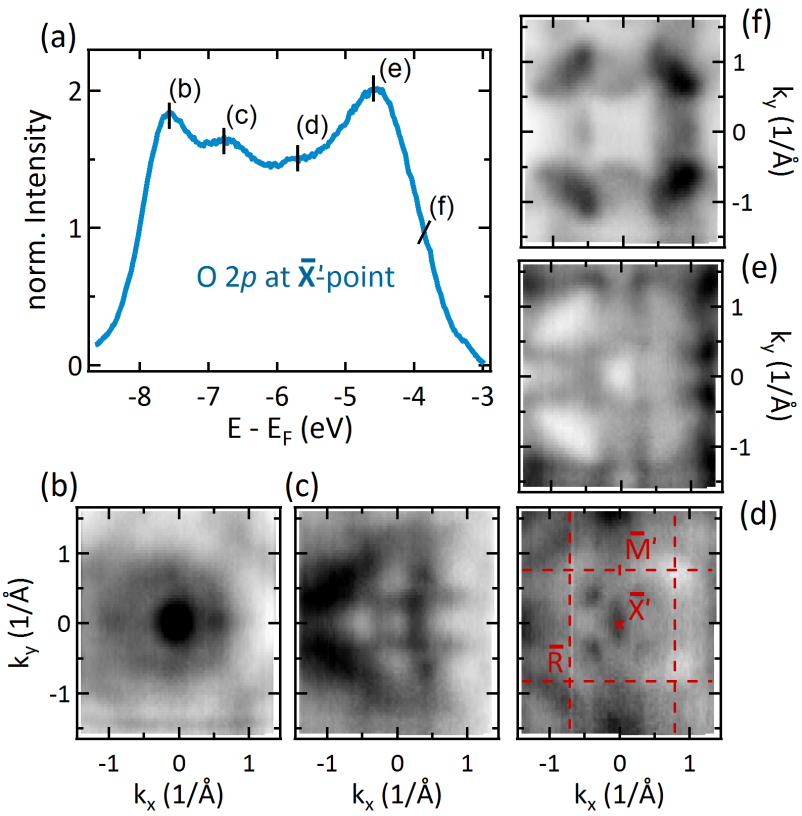

Figure 5.3: O 2*p* valence band of BTO thin films. (a) The spectral weight around the $\bar{X}'$-point displays five characteristic energies at E - E_F = -7.5 eV, -6.8 eV, -5.8 eV, -4.5 eV and -3.8 eV. (b - f) The intensity distribution in k-space is presented by several constant energy maps which are labeled with respect to their energy position in the O 2*p* valence band.

At the excitation energy of $h\nu = 100$ eV the PES hemisphere at normal emission and along $k_\perp$ direction cuts the 3D BZ of BTO near its X′-point. A k_z (= $k_\perp$) plot along the in-plane [1 1 0] direction and for photon energies 80 eV ≤ $h\nu$ ≤ 180 eV is shown in Figure 5.6 (a). Figure 5.3 (a) displays the integrated spectral weight around the $\bar{\text{X}}'$-point of the BTO valence band. It exhibits four intensity maxima and one distinct shoulder at E - E_F = -7.5 eV, -6.8 eV, -5.8 eV, -4.5 eV and -3.8 eV. Measured CEM at each of these energy positions display a characteristic intensity distribution in k-space illustrated in Figure 5.3 (b) - (f). In the map at E - E_F = -5.8 eV the projected cubic BZ with the high-symmetry points ($\bar{\text{X}}'$, $\bar{\text{M}}'$ and $\bar{\text{R}}$) is superimposed (Figure 5.3 (c)).

The CEM of the BTO thin films can not directly be compared to the results of the single crystals in Figure 4.4. Due to their different excitation energies, the photoemission hemisphere in the experiment of single crystalline BTO with a photon energy of $h\nu = 40.84$ eV cuts $k_\perp$ at the Γ-point for normal emission, in contrast to the X′-point for thin BTO films with $h\nu = 100$ eV. This affects the intensity contours in the CEM since the valence bands is measured along different high-symmetry directions.

In addition, the CEM in Figure 5.3 for the BTO thin films exhibit a strong left-right asymmetry in their intensity which is not observed in the case of the BTO single crystals (see Figure 4.4). The intrinsic CEM intensity contours for a cubic system are expected to be 4-fold and symmetric. Therefore, this variation in photoemission intensity is deduced to be an effect of the PES measurement itself. The light polarization in combination with the geometry of the photoemission setup, for instance, contribute to the matrix element in the transition probability of the PES process displayed in Equation (3.6) and, hence, might affect the measured photocurrent [154]. By assuming a plane-wave final-state the resulting matrix element M_{fi}^{k} of Equation (3.3) is determined by $\boldsymbol{A} \cdot \boldsymbol{k}$, where $\boldsymbol{A}$ is the vector potential and $\boldsymbol{k}$ the wave vector of the photoelectron. This assumption leads to an enhanced PES intensity for photoelectrons which are emitted parallel to the light polarization (p-polarization) compared to the perpendicular case [194]. According to this consideration the photocurrent at positive k (corresponds to the right side of the analyzer slit in Figure 3.7) is amplified whereas the photocurrent at negative k (the left side) is reduced. This is, indeed, observed in the CEM of the BTO thin films measured with p-polarized light where the light is coming from negative k values. In the case of the BTO single crystals measured with unpolarized light such an intensity asymmetry is missing (see Chapter 4).

For a better comparison of BTO thin films and BTO single crystals an analogous data set on the BTO thin films at $h\nu = 40$ eV was measured (not shown). However, in these measurements the PES spectral weight is strongly reduced so that the dispersing spectral features of the valence band are hardly visible. This might be due to the fact that the photon energy of $h\nu = 40$ eV is not sufficiently high enough or just at the threshold in order to efficiently create OV and, hence, reduce the system [193]. On

the contrary, the single crystals are prepared by alternating cycles of sputtering and annealing so that the photon energy does not affect the reduction of the surface.

The experimental band structure of the O $2p$ valence band is also directly compared to a theoretical band structure calculation [80] as presented in Figure 5.4. The band structure in Figure 5.4 (a) and (b) is extracted along the high-symmetry directions $\bar{X}'$ - $\bar{M}'$ and $\bar{X}'$ - R from Figure 5.3 (c), respectively. The individual bands are nicely resolved in the photoemission experiment without the application of a 2^{nd} derivative method which was used to display the band structure of the BTO single crystals, *e.g.* in Figure 4.5. In addition, experimental and theoretical results match well, especially near the X-point where the 4 intensity maxima are nicely reproduced by the band structure calculation (see also Figure 5.3 (a)). This means that the BTO films of 8 u.c. are thick enough to induce a considerably high bulk contribution in the PES signal especially as the inelastic mean free path of the photoelectrons is 2 - 3 atomic layers in this photon range.

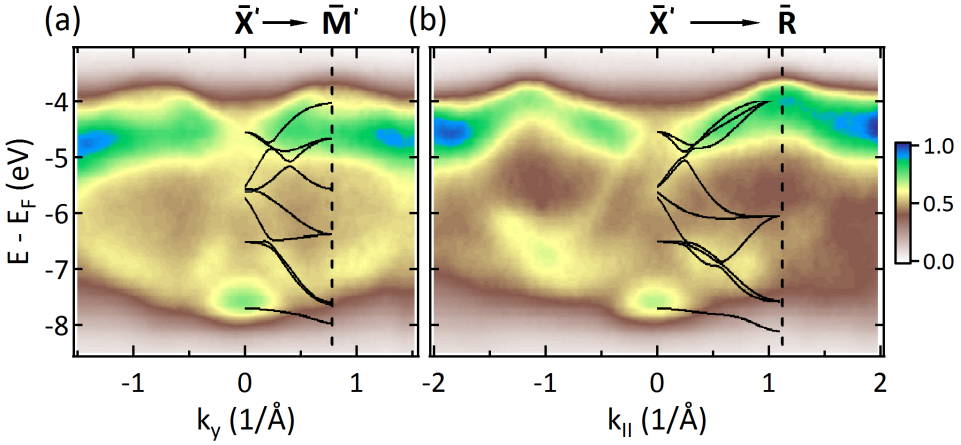

Figure 5.4: Experimental (BTO thin films) vs. theoretical band structure of the BTO O $2p$ valence band along two high-symmetry directions: (a) $\bar{X}'$ - $\bar{M}'$ and (b) $\bar{X}'$ - $\bar{R}$ direction. The experimental data was measured with $h\nu = 100$ eV and p-polarized light at $T = 300$ K. The theoretical spectra are adapted from a study on the bulk electronic structure of BTO (Ref. [80]). At the right side, the color scale for the normalized ARPES intensity is given.

5.3 Electronic structure at the surface

In the PES process, the illumination of the BTO thin films by synchrotron light leads to the creation of OV at the surface and induces itinerant and localized electrons [24, 182, 193]. This effect is accompanied by the occurrence of additional spectral

weight near the Fermi level E_F. The characteristics of this peculiar electronic states and their dependence to the generation of OV is studied in this section.

Figure 5.5 gives a general overview of the ARPES results measured with p-polarized light at $h\nu = 150$ eV and at a sample temperature of $T = 100$ K. The PES data was measured over several SBZ of BTO, namely around $\bar{\Gamma}_{00}$, $\bar{\Gamma}_{01}$, $\bar{\Gamma}_{10}$ and $\bar{\Gamma}_{11}$ and the respective boundaries between these SBZ are emphasized by red dashed lines.

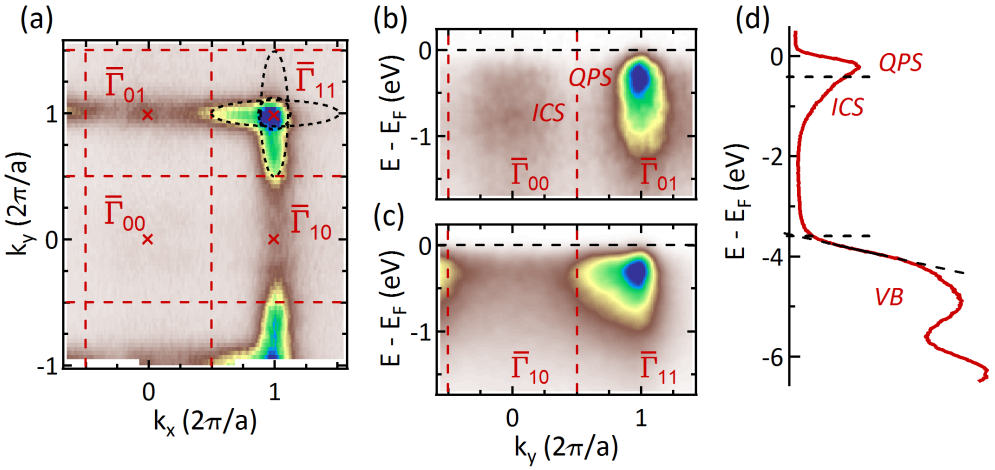

Figure 5.5: Overview of the electronic structure of thin BTO films with a thickness of 8 u.c. ARPES was measured at $h\nu = 150$ eV, p-polarization and $T = 100$ K. (a) The Fermi surface, (b - c) the band structure along specific high-symmetry lines $\bar{\Gamma}_{00}$ - $\bar{\Gamma}_{01}$ (top) and $\bar{\Gamma}_{10}$ - $\bar{\Gamma}_{11}$ (bottom) and (d) the angle-integrated spectral weight are presented. The $\bar{\Gamma}_{hk}$-points (in red) are labeled by Miller indices according to their position in k-space . Red dashed lines highlight the zone boundaries of the BTO's surface BZ in (a - c) and black dashed lines at the right mark the conduction band minimum (CBM) and valence band maximum (VBM).

In the Fermi surface of Figure 5.5 (a) hardly any spectral weight is visible at $\bar{\Gamma}_{00}$ whereas at $\bar{\Gamma}_{01}$ and $\bar{\Gamma}_{10}$ spectral signatures are faintly discernible pointing along k_x and k_y, respectively. Both ellipsoidal contributions next to an additional circular contour become observable at $\bar{\Gamma}_{11}$. The extent of each contribution is indicated by dashed sketches. At higher k values ($k_x \geq 2\pi/\mathrm{a}$ and $k_y \geq 2\pi/\mathrm{a}$), however, the spectral weight is almost completely suppressed. A similar FS for similar experimental condition has already been observed for BTO single crystals [185]. The spectral weight of the Fermi surface is attributed to quasi-particle states (QPS). An associated incoherent spectral (ICS) contribution is still present in the ARPES signal at ≈ 2 eV and, thus, reaches far into the BTO band gap. Both spectral features become obvious in the ARPES

measurements along the $\bar{\Gamma}_{00}$ - $\bar{\Gamma}_{01}$ (top) and $\bar{\Gamma}_{10}$ - $\bar{\Gamma}_{11}$ (bottom) direction in Figure 5.5 (b) and in the angle-integrated spectra in Figure 5.5 (d).

At $\bar{\Gamma}_{01}$ and $\bar{\Gamma}_{11}$ the band structure mainly is determined by the QPS while its spectral weight is significantly suppressed at $\bar{\Gamma}_{00}$. The ICS, on the other hand, is prominently observable at $\bar{\Gamma}_{00}$ and centered at ≈ 0.75 eV. Since both contributions are rather broad in energy (FWHM > 0.2 eV) and indistinct in their dispersion a substantial quasi-particle scattering might be expected. However, a more complete picture of these electronic states becomes available when their response in the PES process is studied with respect to photon energy, light polarization and resonant effects as shown below.

In general, the reduction of the BTO surface leads to metallic states at E_F, namely to a QPS at approximately 0.28 eV, and to a downward shifting of the valence band where the valence band maximum (VBM) is at approximately 3.55 eV. This scenario is best shown in the angle-integrated spectra in Figure 5.5 (d). Despite the shift in energy, the size of the band gap is maintained ($E_g \approx 3.27$ eV [171]) as evaluated by the difference of conduction band minimum (CBM) and VBM given in black dashed lines.

5.3.1 Photon energy dependence

In order to correctly determine $k_z = k_\perp$ of BTO from the photon energy $h\nu$ (see Equation 3.12) the knowledge of the lattice constant c_{BTO} [105] as well as the use of an appropriate *inner potential* V_0 are essential. Here, an optimized *inner potential* of $V_0 = 14.5$ eV [195] is employed which is slightly higher than the value of $V_0 = 12$ eV used in the previous chapter. The reason is that for $V_0 = 14.5$ eV the intensity modulation at the high-symmetry points along k_z in the BZ of BTO are more nicely reproduced. Figure 5.6 (a) presents the corresponding k_z-map for the spectral weight of the QPS along Γ_{00} - Γ_{11}.

Intensity maxima in the spectral weight appear at the Γ_{hkl}-points in the 3D BZ of BTO, namely at Γ_{004}, Γ_{113} and Γ_{114}. The ones at Γ_{004}- and Γ_{114}-point are cut by the PES arcs for the photon energy of $h\nu = 135$ eV and 150 eV, respectively (black dashed lines). Note here, that the photon energy of $h\nu = 100$ eV as used in the measurements of the O $2p$ VB (Section 5.2) intersects with the Γ_{00} direction near the X-point between Γ_{003} and Γ_{004} and with the Γ_{11} direction at the Γ_{113}-point highlighted by a blue arc in Figure 5.6 (a).

In Figure 5.6 (b) - (e) the corresponding Fermi surfaces are presented, along with the ones for $h\nu = 80$ eV and 120 eV. Their intensity distribution within the k_x-k_y plane strongly varies with the photon energy. For instance, in the FS maps at $h\nu = 120$ eV and 135 eV in Figure 5.6 (c) and (d) a considerable intensity of the QPS is visible at $\bar{\Gamma}_{00}$. In the respective FS maps for $h\nu = 80$ eV and 135 eV (Figure 5.6 (b) and (e)), on the

other hand, a noticeable QPS contribution is observed at $\bar{\Gamma}_{10}$ and $\bar{\Gamma}_{01}$. However, the ARPES signal of the QPS not only modulates laterally but also along k_z as already mentioned above in the k_z-map of Figure 5.6 (a). The modulation along k_z most likely is due to a finite number of BTO layers contributing to the total intensity. This conversely means that the QPS is not completely confined at the surface but marginally penetrates into the bulk. However, a prominent dispersion of the QPS along k_z is not discernible so that the QPS is considered to be of 2D character. Further properties of the QPS and the ICS can be unveiled by studying their polarization dependence.

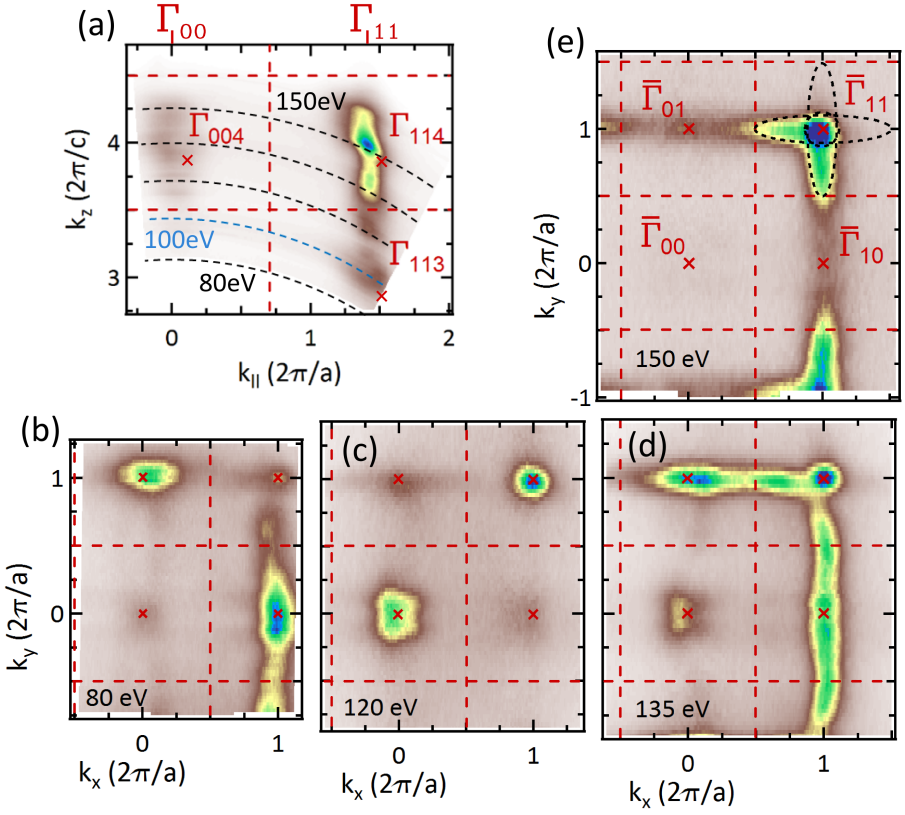

Figure 5.6: Photon energy dependence of the electronic states in a 8 u.c. thin BTO film. (a) The spectral weight of the QPS is displayed as a function of k_z measured in the photon energy range of 80 eV $\leq h\nu \leq$ 180 eV. (b - e) Different Fermi surfaces for the particular excitation energies of $h\nu = 80$, 120, 135 and 150 eV measured at $T = 100$ K and with p-polarization. Each excitation energy is emphasized by a black arc in the k_z-scan in (a). In addition, the PES hemisphere for $h\nu = 100$ eV is plotted in blue. The red dashed lines indicate the BZ boundaries in the different FS and in the k_z-scan.

5.3.2 Polarization dependence

The FS for $h\nu = 135$ eV and p-polarized light in Figure 5.6 (d) exhibits relatively high intensity at $\bar{\Gamma}_{00}$ as the PES hemisphere cuts the 3D BZ of BTO at Γ_{004} along k_z and at normal emission. In addition, the elongated ellipsoids along k_x, k_y and the circular contour are separately visible at $\bar{\Gamma}_{01}$, $\bar{\Gamma}_{10}$ and $\bar{\Gamma}_{11}$, respectively. Figure 5.7 illustrates how the spectral weight of the QPS and the ICS varies when the light polarization is altered from p-polarization to s-polarization. This also means that the polarization vector which originally lies within the PES scattering plane (p-pol.) is rotated out of the plane pointing in perpendicular direction (s-pol.) (see Subsection 3.6.2).

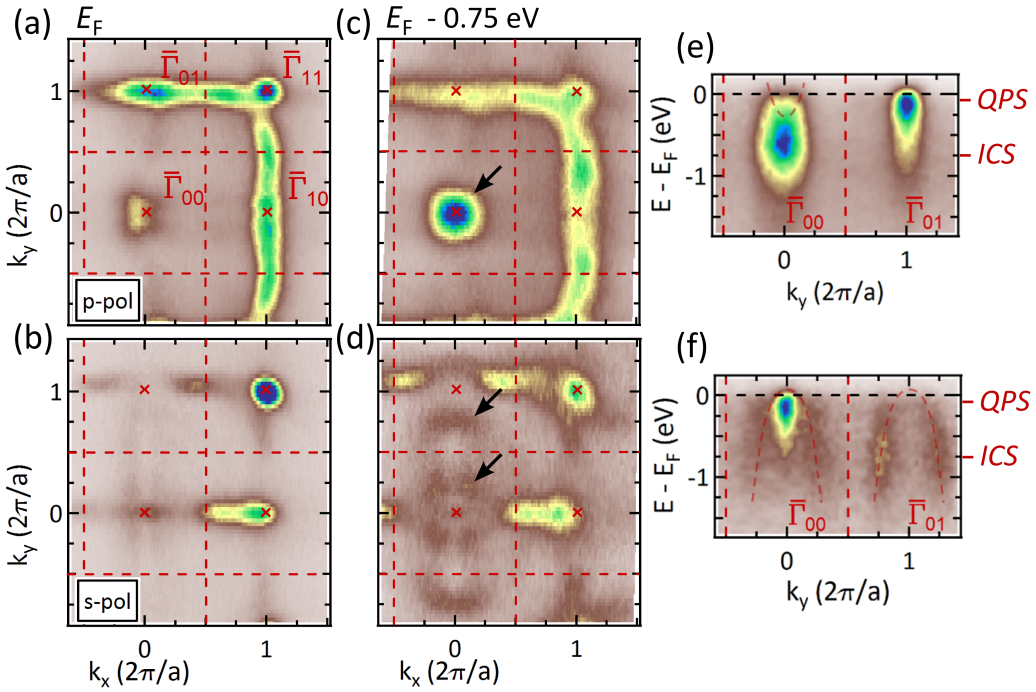

Figure 5.7: Polarization dependence of the electronic states. The top / bottom panel shows the ARPES results for p / s-polarized light measured with $h\nu = 135$ eV at $T = 100$ K. (a - b) Direct comparison of the intensity distribution in the FS map, (c - d) for the CEM at E_F -0.75 eV and (e - f) of the electronic structure along $\bar{\Gamma}_{00}$-$\bar{\Gamma}_{01}$ direction for both light polarizations is possible. Black arrows highlight the spectral weight of the ICS in (c - d). In addition, the signatures of an electron and a hole pocket are observed at the $\bar{\Gamma}_{00}$-point for p- and s-polarized light, respectively, indicated by shallow red parabolas in (e - f).

In the FS map of Figure 5.7 (b) the spectral weight of the QPS is strongly reduced within the whole k_x-k_y plane for s-polarization, besides at $\bar{\Gamma}_{10}$ and $\bar{\Gamma}_{11}$. At the high-

symmetry points the intensity nearly stays the same or is even increased for $\bar{\Gamma}_{10}$ and $\bar{\Gamma}_{11}$, respectively. In the first case, the elongation of the electronic feature, moreover, is rotated by 90°. In order to consider the intensity distribution of the ICS, respective CEM at E_F -0.75 eV in Figure 5.7 (c) and (d) are regarded. The spectral features of the QPS are faint, however, also additional spectral weight accumulates around the $\bar{\Gamma}_{00}$-point. In the case of *p*-polarization this supplementary intensity which is highlighted by black arrows exhibits a circular contour whereas for *s*-polarization it appears in the form of a paddle along $\bar{\Gamma}_{00}$-$\bar{\Gamma}_{01}$ direction. The corresponding ARPES maps along $\bar{\Gamma}_{00}$-$\bar{\Gamma}_{01}$ direction in Figure 5.7 (e) and (f) clarify the spectral properties of the QPS and the ICS. For instance, the shape of the QPS at the $\bar{\Gamma}_{00}$-point can approximately be described by an electron pocket as highlighted by a red dashed parabola (see Figure 5.7 (e)). This electronic feature, however, is only discernible for *p*-polarized light and for the photon energies of $h\nu = 135$ eV and 120 eV (not shown). In contrast, *s*-polarization reveals signatures of hole-like bands around $\bar{\Gamma}_{00}$ and $\bar{\Gamma}_{01}$ leading to the paddles in the respective CEM. Their dispersion is indicated by red dashed parabolas in Figure 5.7 (f) and resembles in shape and dispersion an electronic state observed in the layered system Al/BTO/STO [196].

The contribution of the QPS and the ICS to the complete spectral weight in PES becomes obvious in EDC at particular high-symmetry points, *e.g.* at $\bar{\Gamma}_{00}$ and $\bar{\Gamma}_{10}$, as displayed in Figure 5.8 (a) and (b). The dashed lines reflect the energy positions of the ICS as suggested in the CEM in Figure 5.7 (c) and (d) and of the QPS. A general trend is the increase of the ICS spectral weight when the polarization vector is rotated into the scattering plane of the PES geometry. Circular polarization contains contribution of both polarization vectors and, thereby, the measured spectral weight averages over those of *p*-pol and *s*-pol. In addition, the ICS seems to be composed of several electronic contributions which are pronounced at distinct $\bar{\Gamma}$-points. At $\bar{\Gamma}_{10}$ in Figure 5.8 (b) the ICS is centered at E_F - 0.75 eV whereas at $\bar{\Gamma}_{00}$ in Figure 5.8 (a) two different spectral contributions at an energy $< E_F$ - 0.75 eV and $> E_F$ - 0.75 eV are observed. These contributions are enhanced for a certain light polarization so that the prominent feature at the higher binding energy is best visible for *s*-polarization.

The ARPES signal, on the one hand, significantly modulates in the 3D k-space which was studied in the previous subsection. On the other hand it strongly depends on geometry parameters and on the symmetry of the experiment as light incidence, light polarization, scattering plane, etc. [154]. Changes in the spectral weight of the individual electronic contributions of QPS and ICS with respect to the light polarization can be attributed to their orbital character including their orientation in k-space. This is manifested by the initial wave function of the electronic states. However, in order to unambiguously determine the origin of the QPS and the ICS a resonant PES experiment was performed. At the end of Subsection 5.3.3 both electronic contributions,

QPS and ICS, are assigned to particular orbitals based on the results of the photon energy dependence, the polarization dependence and the resPES results.

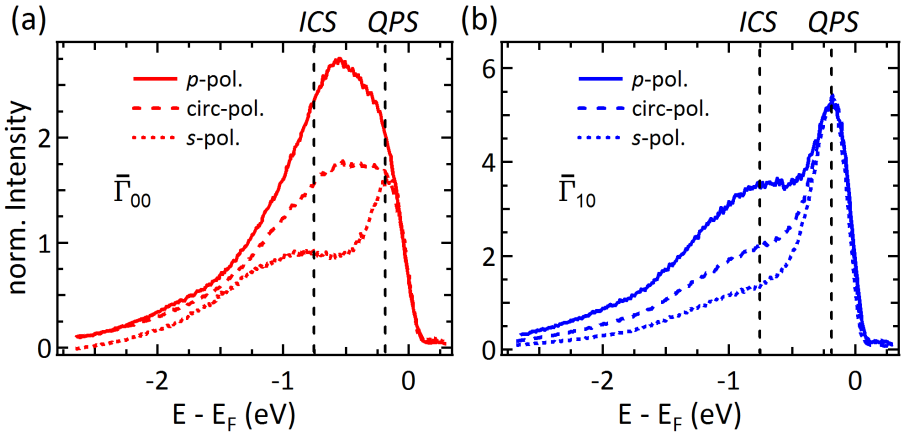

Figure 5.8: Polarization dependence of the QPS and ICS. Spectral weight of the QPS and the ICS are illustrated as a function of light polarization (p-pol, circular polarization (circ-pol) and s-pol) at $\bar{\Gamma}_{00}$ in (a) and $\bar{\Gamma}_{10}$ in (b). The dashed lines at higher E - E_F coincides with the energy positions of the CEM in Figure 5.7 (c) and (d) and the dashed line near E_F approximately gives the energy position of the QPS at $\approx E_F$ - 0.2 eV. All spectra are normalized to the background intensity and to the spectral weight at E_F.

5.3.3 Resonant PES

The technique of resonant PES (resPES) excites particular electronic states near or slightly above E_F due to a process based on an Auger decay besides the direct PES process (see Section 3.3). In our case these electronic states are the QPS and the ICS which are expected to be derived from the originally, with no surface reduction, empty Ti 3d conduction band.

Resonant PES usually is applied in combination with the respective X-ray absorption spectrum (XAS) of a corresponding material's K, L, M edge. In order to study the origin of the QPS and the ICS with respect to Ti 3d states, the Ti $L_{2,3}$ edges are of interest. The Ti L_3 (L_2) edge corresponds to an excitation of an electron from the Ti $2p_{3/2}$ ($2p_{1/2}$) core-level to the Ti 3d conduction band. In addition, the perovskite structure of BTO affects a splitting of the conduction band, the so-called crystal field splitting, with the distinct energy levels Ti $3d_{t_{2g}}$ and Ti $3d_{e_g}$ (see Section 3.1). Theoretical XAS spectra exhibit a characteristic multiplet structure reflecting the Ti 2p spin-orbit splitting and the Ti 3d crystal field splitting. This has been first shown experimentally and theoretically for a series of different TMO [139, 197]. More elaborated theoretical

studies reproduce the experimental results on BTO single crystals [198] as well as for thin BTO films in a BTO/STO multilayer system [199].

Figure 5.9 (a) presents the XAS data for the 8 u.c. thin BTO films on STO measured at $T = 300\,\mathrm{K}$ via total electron yield (TEY). The experimental spectra displays the expected multiplet structure and is in good agreement with a recent theoretical calculation for the tetragonal ferroelectric phase [198]. In addition, the XAS spectra allows to determine the carrier density at the surface which has already been shown for STO [192]. By comparing the line shape of the XAS spectrum in Figure 5.9 (a) to the results of STO [192] a low 2D carrier density in the order of $10^{14}\,\mathrm{cm}^{-2}$ for the thin BTO films can be deduced. A more elaborated evaluation of the carrier density for the BTO films, however, is depicted at the end of this subsection. In general, by means of the XAS results it is possible to estimate the doping level besides the determination via the Ti $2p$ core-levels [174].

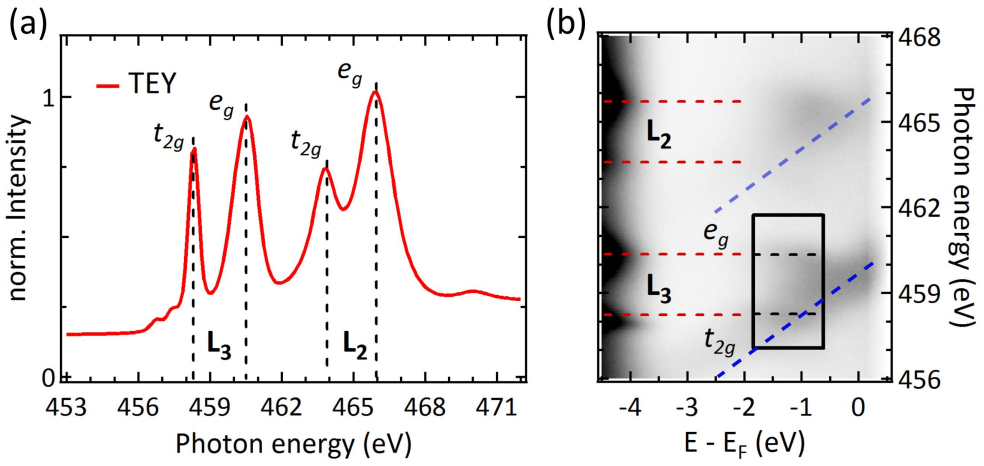

Figure 5.9: (a) XAS results at the Ti L_3 and Ti L_2 edge of BTO measured by means of total electron yield (TEY) at $T = 300\,\mathrm{K}$. The multiplet structure closely resembles the results of a recent theoretical study [198]. (b) Angle-integrated PES spectra of the QPS and the ICS measured in the same photon range as the XAS spectra but at $T = 100\,\mathrm{K}$. The red / black dashed lines highlight the individual resonances at the Ti L_3 / L_2 edge for Ti $3d_{t_{2g}} / 3d_{e_g}$ states and the blue dashed lines the 2$^{\mathrm{nd}}$ order peak in PES signal for synchrotron light.

In Figure 5.9 (b) the response of the individual electronic states, namely of the valence band, the ICS and the QPS, are studied depending on the photon energy near the Ti L_3 (L_2) edge. The red dashed lines indicate the respective excitation energies for the absorption edges. The spectral weight at the top of the valence band, *i.e.* at approximately E_F - 4 eV, is strongly enhanced for excitation energies at the Ti L_3 edge

and at the e_g part of the Ti L_2 edge. Also the intensity of the ICS is increased at these energies, especially at the Ti L_3 edge (black box). This means that both, valence band and ICS, are partially composed of Ti $3d$ states. In the case of the valence band this has been already shown theoretically and experimentally traced back to a finite p - d hybridization of valence and conduction band states [37, 72, 170, 181]. The ICS in BTO is also supposed to exhibit a significant p - d hybridization as shown for the structural isomorph STO [200]. For the QPS, however, a similar evaluation is not possible due to the large 2nd order peak in PES signal for synchrotron light as highlighted by the blue dashed lines. A subtraction of this interfering spectral weight which is shown in the Supplementary Material of Ref. [141] is rather challenging since the ARPES signal in total is too small.

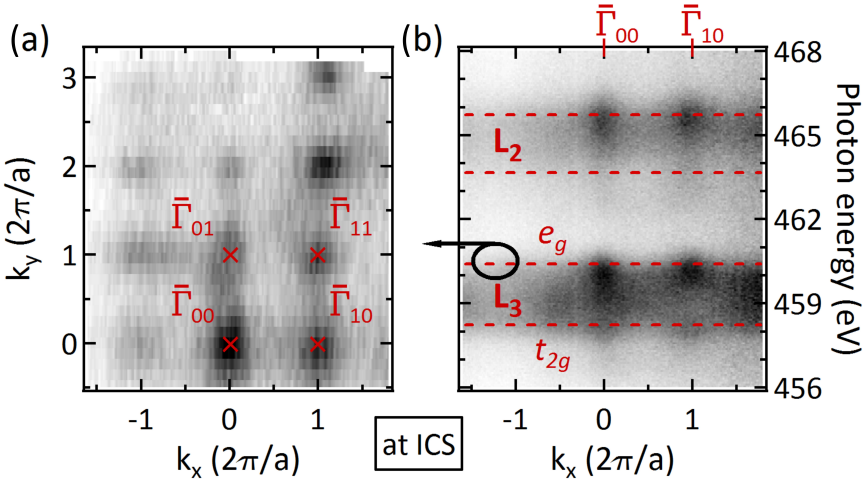

Figure 5.10: ResPES results of the ICS in BTO thin films. (a) CEM at E_F - 0.75 eV measured with $h\nu$ = 460.3 eV and p-polarized light at T = 100 K. This excitation energy coincides with the e_g part of the Ti L_3 edge marked by the second lowest dashed line in the k-map highlighted by a black circle. (b) Variations in the ICS spectral weight along k_x as a function of photon energy.

The intensity distribution of the ICS (at E_F - 0.75 eV) is further investigated by means of a CEM in Figure 5.10 (a). It is apparent that most of the ICS spectral weight appears at the $\bar{\Gamma}_{hk}$-points (red). The circular contour at these high-symmetry points resembles the results for $h\nu$ = 135 eV and p-polarized light in Figure 5.7 (c). In Figure 5.10 (b) a photon energy map of the ICS intensity along k_x is displayed. Spectral weight accumulates at $\bar{\Gamma}_{00}$ and $\bar{\Gamma}_{10}$ for photon energies corresponding to the e_g part of the Ti L_3 and the Ti L_2 edge. In contrast, the ICS signal at the t_{2g} part of the Ti L edges is significantly smaller.

In summary, the CEM in Figure 5.7 and Figure 5.10 reveal that the ICS is delocalized in k space and its intensity distribution in the k_x-k_y plane reflects the one of the QPS. In addition, there is no strong decoupling of both electronic contributions. Hence, it is assumed that the QPS and the ICS are of same orbital character. The resPES data in Figure 5.9 and Figure 5.10 suggests that the ICS is derived from Ti 3d-e_g states. However, from the polarization dependence of the ICS in Figure 5.8 two electronic contributions are expected. A recent theoretical work [96] assigns the contribution at higher binding energy primarily to Ti 3d_{z^2} orbitals, the shallow state more to Ti 3$d_{x^2-y^2}$ orbitals [96]. Since the signal of the ICS located at higher binding energy is almost completely suppressed for s-polarized light, this contribution can indeed be attributed to Ti 3d_{z^2} states by sample geometry. On the other hand, the ARPES data of BTO from Figure 5.5 to Figure 5.10 do not provide a clear evidence for a pronounced in-gap state as in STO [34].

In STO it has been demonstrated that the 2D electron gas near E_F consists of Ti 3d states with t_{2g} symmetry [22, 23]. The different spectral shape at the individual $\bar{\Gamma}_\mathrm{hk}$-points in STO is attributed to an anisotropic charge carrier hopping which lifts the degeneracy of the Ti 3d states [76]. This results in d_{xz} and d_{yz} states elongated along k_y and k_x, respectively [201]. Since the BTO thin films reproduce these intensity contours at $\bar{\Gamma}_{10}$ and $\bar{\Gamma}_{01}$ in Figure 5.6 (b) and (d) the QPS in BTO can be derived from d_{xz} and d_{yz} states. The intense circular signal at $\bar{\Gamma}_{11}$ reflects d_{xy} states pointing along k_z in accordance to the STO result in Ref. [201]. From the extent of the Fermi contour at $\bar{\Gamma}_{11}$ in Figure 5.5 (a) it is possible to deduce the 2D carrier density. Thereby, the area of the ellipses and of the circle highlighted by black dotted lines are integrated to an area A_{FS}. The corresponding formula $n_\mathrm{2D} = 2A_{FS}/(2\pi)^2$ for the 2D carrier density yields $n_\mathrm{2D} \approx 4.5 \times 10^{14}$ cm^{-2} (see Supplementary Material of Ref. [93]). This value can be converted into a 3D carrier concentration of $n_\mathrm{3D} \approx 2 \times 10^{21}$ cm^{-3} which is just at the threshold of a doping induced para- and ferroelectric phase transition [156].

5.3.4 Review on diffraction and substrate effects

In the previous subsections it has been pointed out that the QPS and the ICS derive from Ti 3d states. A possible mechanism in order to shift these originally unoccupied states below E_F is given by the band bending picture illustrated in Figure 2.8. Nevertheless, other side effects might distort the actual electronic structure of the thin BTO films on STO. In this subsection, the impact of two possible mechanisms are studied, namely the influence of the substrate electronic structure and photoelectron diffraction (PED) effects [135, 202].

Figure 5.11 compares the EDC at $\bar{\Gamma}_{11}$ of STO to the one of BTO. These curves are extracted from the respective 3D data set ($k_x = 2\pi/a$, $k_y = 2\pi/a$ and E - E_F) of the pure

STO substrate and of the BTO films on STO. The spectral weight of the QPS and the ICS are much more pronounced in the case of STO. In addition, the position of the ICS is shifted towards higher binding energies, namely to E - $E_F \geq 1$ eV, and the spectral weight at the VBM differs remarkably in comparison to BTO.

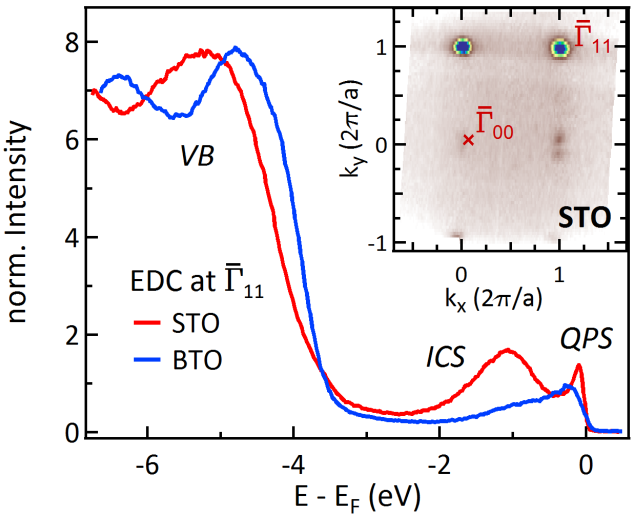

Figure 5.11: Comparison of EDC at $\bar{\Gamma}_{11}$ measured with $h\nu = 135$ eV (p-pol.) at $T = 100$ K. The spectral weight of the VB, the ICS and the QPS clearly varies for the pure STO substrate and for BTO films on STO. In addition, STO displays a different intensity contour in the FS (inset) compared to the FS of the BTO thin films. Both spectra are normalized to the background intensity.

Furthermore, the intensity contours at the FS of STO and BTO are compared. The inset of Figure 5.11 presents the FS of STO measured with $h\nu = 135$ eV (p-pol.) at $T = 100$ K. In contrast to BTO, the spectral weight is concentrated rather directly at the $\bar{\Gamma}_{hk}$-points and not within the high-symmetry points [201] as in the case of BTO illustrated in Figure 5.6 and 5.7. Hence, a significant manipulation of the electronic structure of BTO by means of the STO substrate can be excluded. From the surface structure analysis in Section 5.1 and a growth study [56] it can be assumed that the uppermost BTO layers of the 8 u.c. thick film display the bulk BTO lattice constant a_{BTO} with a slight distortion due to minor stress.

A second mechanism which might affect the electronic structure in the BTO thin films is PED [202]. An important step in the PES process as a whole is the propagation of the excited photoelectron to the surface [135]. The scattering of this photoelectron by the crystal potential leads to an additional intensity modulation due to interference effects. The PED pattern and intensity, thereby, depends on the kinetic energy of the electron and also varies in k-space by reflecting the crystal structure.

The electronic features of the BTO films discussed so far, hence, might actually stem from PED patterns which are a result of photoelectron scattering. In order to exclude this side effect the PED intensity maps are studied at specific core-levels in BTO involving Ba, Ti and O. Figure 5.12 (a) - (c) depicts the respective results of the O $2s$ ($E_B = 22$ eV), the Ti $3p$ ($E_B = 37.5$ eV) and the Ba $4d$ ($E_B = 90.7$ eV) states. In all the experiments the kinetic energy of the photoelectrons is maintained at ≈ 131 eV and

coincides with the energy of the photoelectron for the FS at $h\nu = 135$ eV presented in Figure 5.6 (d). This allows a precise comparison of FS and PED patterns as also the PED intensity changes with the electron wavelength. The PED patterns of the O 2*s* and Ba 4*d* core-level in Figure 5.12 (a) and (c) exhibit a circular shape. At the Ti 3*p* core-level in Figure 5.12 (b) the PED pattern resembles more a X-like shape with the main intensity near the corners of the surface BZ. In total, the PED patterns do not reflect the symmetry of the FS contours illustrated in Figure 5.6 and Figure 5.7. This symmetry consideration proves that the spectral weight in the FS map can not be related to a PED signal but reflects the actual electronic structure in BTO.

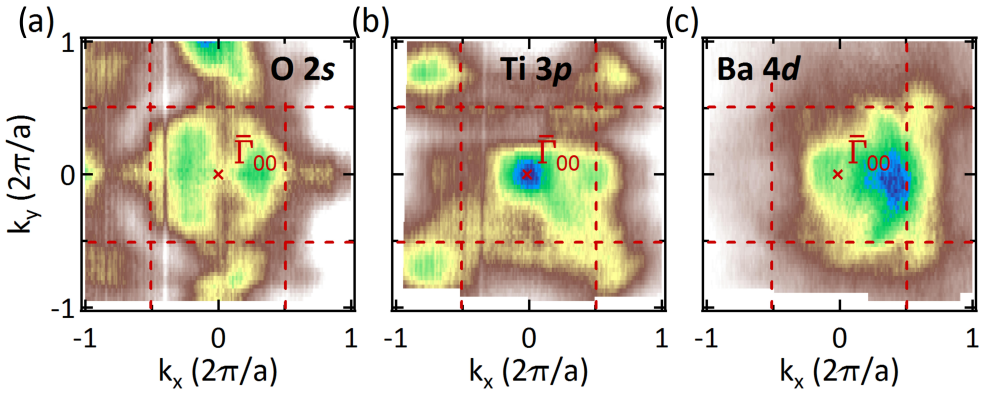

Figure 5.12: (a - c) PED patterns at the O 2*s*, Ti 3*p* and Ba 4*d* core-level measured at $T = 300$ K with *p*-polarized light and $h\nu = 156$ eV, 171.5 eV and 224.7 eV, respectively. The $\bar{\Gamma}_{00}$-points and the boundaries of the surface BZ are highlighted in red.

5.3.5 Dependency on oxygen vacancy density

The energy position of E_F in the BTO samples as well as the the amount of band bending at its surface can be linked to the creation of OV at the surface. Until now, the validity of this assumption is based on similar ARPES results observed in other titanates [23, 24, 182]. In this subsection an approach is applied which allows to find a direct correlation between oxygen deficiency and the existence of a 2DEG in BTO thin films.

As a first step the impact on the electronic states in BTO is studied while the amount of OV in the system is systematically altered. The illumination of an oxide material by synchrotron light might lead to the creation of OV at its surface [24]. In order to reoccupy these vacant oxygen sites partial oxygen pressure p_{O_2} during the PES experiment might be applied [182]. Depending on the balance of reoxidization of OV and the reduction of the BTO the electronic properties as the energy position and

spectral weight of the VB, ICS and QPS can be tuned.

Figure 5.13 summarizes the changes in the electronic structure of BTO by increasing p_{O_2} in the analyzer chamber from the nominal value $p_{O_2} \approx 10^{-11}$ mbar to 4×10^{-8} mbar. The value of p_{O_2} is illustrated in Figure 5.13 (c). By increasing p_{O_2} the spectral weight of the ICS and of the QPS illustrated by white dashed lines gets dramatically reduced and no significant ARPES intensity remains visible in the case of high p_{O_2} (see angle-integrated spectra in Figure 5.13 (a)). Simultaneously, the VB shifts towards lower binding energies by ≈ 140 meV and approaches an energy position which is close to the VBM of the insulating case by reflecting the optical band gap of BTO [168, 171]. A FS cut along k_x and measured as a function of p_{O_2} further clarifies the electronic situation at E_F displayed in Figure 5.13 (b). It is confirmed that the QPS spectral weight vanishes completely at the $\bar{\Gamma}_{00}$- and the $\bar{\Gamma}_{10}$-point for $p_{O_2} = 4 \times 10^{-8}$ mbar. This result might be related to an metal-to-insulator transition which is determined by a critical charge carrier concentration of BTO [203].

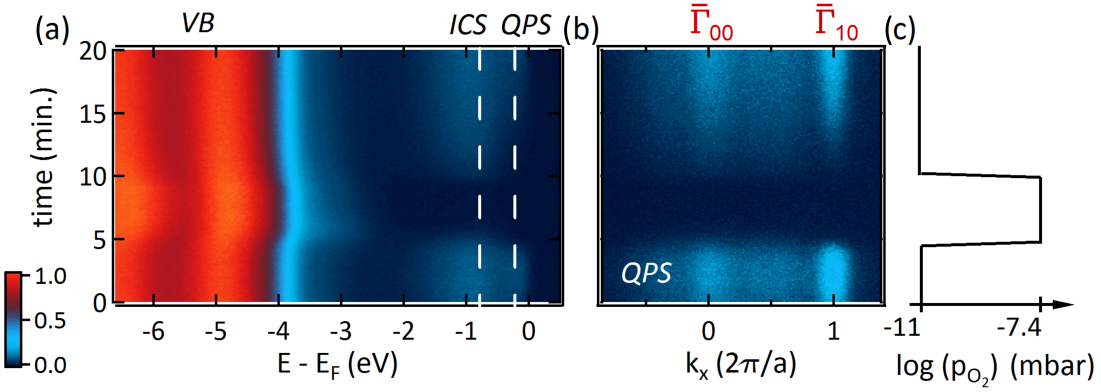

Figure 5.13: Impact of partial oxygen pressure p_{O_2} upon the individual electronic states in BTO (VB, ICS and QPS) measured at $T = 300$ K with $h\nu = 135$ eV and p-polarization. (a) Angle-integrated spectra as a function of time when p_{O_2} is varied. The energy position of the ICS and QPS are highlighted by white dashed lines and the color scale for the normalized ARPES intensity is given at the left bottom. (b) Angle-integrated spectra which presents the change in the QPS spectral weight at E_F along k_x, namely in $\bar{\Gamma}_{00}$ to $\bar{\Gamma}_{10}$ direction, for different p_{O_2}. (c) Range of p_{O_2} from 10^{-11} to 4×10^{-8} mbar.

In the following, the electronic states close to E_F are studied in more detail concerning their oxygen dependency. Therefore, the QPS and the ICS were measured for different p_{O_2} values in the range of 10^{-11} mbar $\leq p_{O_2} \leq 10^{-7}$ mbar. Their spectral weight is displayed by EDC plots for each distinct p_{O_2} at $\bar{\Gamma}_{00}$ and $\bar{\Gamma}_{10}$. The corresponding spectra are presented in Figure 5.14 (a) and (b), respectively. At $\bar{\Gamma}_{00}$, the spectral weight of the more intense ICS decreases more rapidly than the one of the QPS. At

$\bar{\Gamma}_{10}$, where the contribution of the QPS predominates, this tendency is reversed. In a very confined region close to E_F the orbitals with Ti $3d_{xz}$ and Ti $3d_{yz}$ character are proposed to be most favorable orbitals contributing to the QPS [101]. As matrix-element effects in the PES experiment [154] prefer Ti $3d_{xz}$ orbitals at $\bar{\Gamma}_{10}$ illustrated in Figure 5.6 the spectral weight of the QPS exceeds the one of the ICS in Figure 5.14 (b). At $\bar{\Gamma}_{00}$, on the other hand, the QPS exhibits no predominant orbital character and the IGS represents the main contribution. The spectral weight, in total, drops steadily at both high-symmetry points by increasing p_{O_2} and for $p_{O_2} = 10^{-8}$ mbar almost no spectral weight of the QPS and the ICS is left. This behavior is comparable to the observation in Figure 5.13 where the ARPES intensity decreases for higher p_{O_2}. Both results also resemble to the findings of a similar study, however, on STO [93].

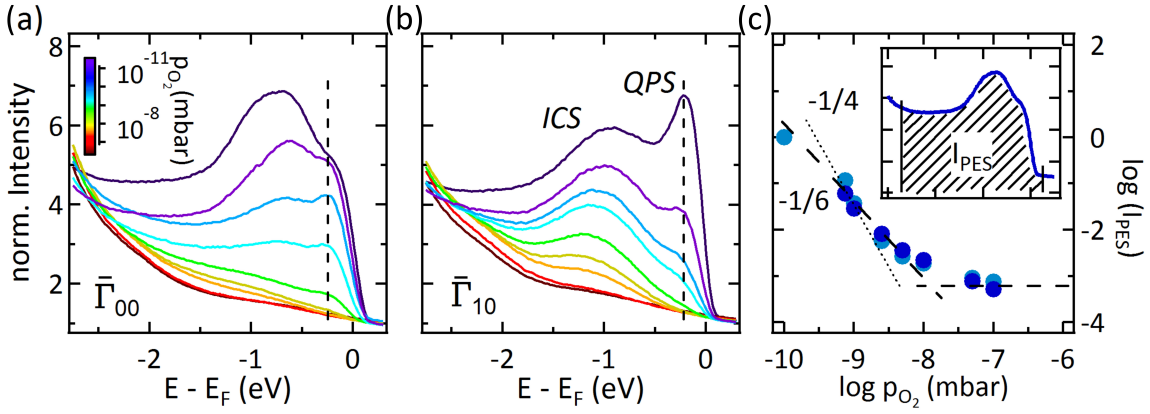

Figure 5.14: Quantitative study of the surface electronic structure upon changes in p_{O_2} ($h\nu = 135$ eV, p-pol. and $T = 100$ K). (a - b) The spectral weight of the QPS and the ICS are presented as EDC plots for 10^{-11} mbar $\leq p_{O_2} \leq 10^{-7}$ mbar at $\bar{\Gamma}_{00}$ and $\bar{\Gamma}_{10}$, respectively. All spectra are normalized to the background intensity and the scale of p_{O_2} is given in (a). (c) Spectral weight of QPS and ICS plotted with respect to p_{O_2} in a double logarithmic scale. The dashed and dotted line show the scaling behavior of -1/6 and -1/4 for a 2+ and 1+ charge state of the OV.

In STO, it has been proposed that by the removal of an oxygen atom from the surface one of the two released electrons is trapped in an in-gap state (see Ref. [34] and Subsection 2.1.5). The itinerant electron, on the other hand, might occupy the nominally empty Ti $3d$-t_{2g} band which is shifted below E_F due to band bending at the surface (see Subsection 2.1.6). Exposing the surface again to atomic oxygen leads to a suppression of the OV as well as of the QPS. This relates the occurrence of the 2DEG to the density of charged OV on the surface [182].

It is still unclear whether the same situation holds for BTO, *i.e.* how many of the released electrons are itinerant or localized. In order to answer this question a model

considering the reoxididation process in BTO is derived. Figure 5.14 (c) summarizes the results of this quantitative evaluation. Thereby, the integrated spectral weight I_{PES} at E_F summed up over the QPS and the ICS is taken into account which is seen in the inset of Figure 5.14 (c). It is implied that the QPS and the ICS are not decoupled as already discussed in Section 5.3.3. The respective I_{PES} at $\bar{\Gamma}_{00}$ (light blue) and $\bar{\Gamma}_{10}$ (dark blue) are plotted as a function of p_{O_2} in a double logarithmic scale.

In the following, the reoxidization process is described by an oxygen diffusion model. A first step is to determine the kind of vacancy which is the energetically most favorable in BTO by also including metal vacancies. Indeed, it has been demonstrated that under normal thermodynamic boundary conditions the oxygen-related vacancy mostly prevails [204]. In particular, the double shallow donor $V_O^{\cdot\cdot}$ is dominant [205]. This allows to set up the equation for the point defect reaction where two electrons e' are released [206]: $O_O^{\times} \leftrightarrows V_O^{\cdot\cdot} + 2e' + \frac{1}{2}O_2$ (in Kröger-Vink-notation), where the left side represents the reduction of the oxide. The equilibrium constant K_{red} is the corresponding unit in order to describe the reactivity and is given by the the product of the concentration of the reactants: $K_{red} \propto c_{V_O^{\cdot\cdot}} n_e^2 \sqrt{p_{O_2}}$, where $c_{V_O^{\cdot\cdot}}$ is the concentration of OV and n_e^2 is the electron density [206].

In addition, the charge neutrality condition is assumed, *i.e.*, the electron concentration compensates for the oxygen vacancy: $2n_e^2 = c_{V_O^{\cdot\cdot}}$. Thereby, n_e is the electron density within the quantum well close to the surface (≈ 10 Å) induced by band bending [207]. The concentration of OV, however, is a bulk property since they are generated by synchrotron light penetrating into the sample on the order of 1 μm. Through the creation of oxygen defects in the bulk, free carriers are released and accumulate in the surface quantum well. The quantum well as a subsystem is in dynamical thermal equilibrium with its surrounding bulk, so that photoemission probes a bulk reservoir where the law of mass action holds. By considering all these facts the electron density n_e is supposed to display a scaling behavior of $p_{O_2}^{-1/6}$. This result is nicely reproduced in the integrated data of Figure 5.14 (c). The slope of n_e with the relation $n_e \propto I_{PES}$ is close to -1/6 as highlighted by the black dashed line. Most of the OV in BTO, hence, can be associated to a 2+ charge state. This is in contrast to single crystalline STO [97] and LAO/STO [99], where a 1+ charge state of the OV has been observed. The corresponding -1/4 scaling behavior is illustrated by a faint black dotted line in Figure 5.14 (c). In the case of thin STO films with 10 u.c. thickness the dependency of $n_e \propto I_{PES}$ changes in favor of a -1/6 scaling behavior [97] which is more comparable to the results of the 8 u.c. thick BTO film. Nevertheless, the results of STO and LAO/STO have been performed at strongly elevated temperatures ($950\,K \leq T \leq 1100\,K$) which exceed the measuring temperature of the BTO thin films by one order of magnitude. Therefore, it is important to know in addition how the temperature influences the electronic structure of BTO at E_F.

5.3.6 Temperature dependence

In the previous subsection it has been clarified that atomic and molecular oxygen is able to reoxidize oxygen defects at the surface and, thereby, varies the spectral weight of the QPS and the ICS. Another mechanism is the migration of atomic oxygen from subjacent layers to the surface. In BTO single crystals presented in Subsection 4.2.4 already a total shift of ≈ 60 meV in the O $2p$ valence band has been observed by varying the temperature. This temperature effect might lead to a similar response in the electronic structure as seen for p_{O_2} in the previous subsection.

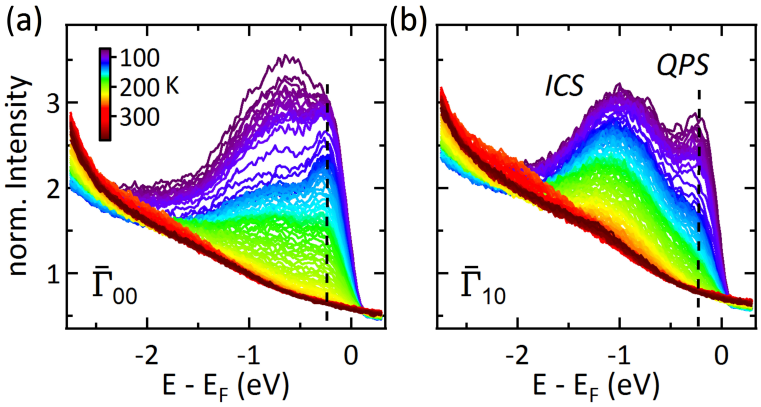

Figure 5.15: Quantitative study of surface electronic structure as a function of T measured with $h\nu = 135$ eV and p-polarized light at $p_{O_2} = 10^{-11}$ mbar. (a - b) The spectral weight of the QPS and the ICS in the form of EDC is illustrates at $\bar{\Gamma}_{00}$ and $\bar{\Gamma}_{10}$, respectively, by increasing T from 80 K to 380 K. All spectra are normalized to the background intensity and the temperature scale is given in (a).

In the following the spectral weight is studied as a function of the temperature by increasing the temperature from $T = 100$ K to $T = 380$ K. However, similar trends were observed by lowering the temperature from $T = 380$ K to $T = 100$ K. Figure 5.15 (a) and (b) display the spectral weight of the thin BTO films at $\bar{\Gamma}_{00}$ and $\bar{\Gamma}_{10}$ in the range of $80\,\text{K} \leq T \leq 380\,\text{K}$. An increase in T is accompanied by a reduction of the ARPES intensity near E_F. This is by analogy with the spectra in Figure 5.14 displaying a similar behavior of the QPS and ICS upon changes in p_{O_2}. Even the reversed trend of the QPS and ICS spectral weight at $\bar{\Gamma}_{00}$ and $\bar{\Gamma}_{10}$ is consistent in the T-dependent data of Figure 5.15. The response of the 2DEG (QPS) in BTO to the external parameters of T and p_{O_2} might be explained by an universal model.

Changes in p_{O_2} or T might not only affect the electronic states close to E_F but also the shape and the energy position of core-levels in the BTO thin films. In Figure 4.11 and Figure 5.13, already a slight shift in the O $2p$ valence band of BTO has been

observed by either changing T or p_{O_2}. It is supposed that the appearance of the QPS at the surface can be correlated to a respective energy shift of other electronic states.

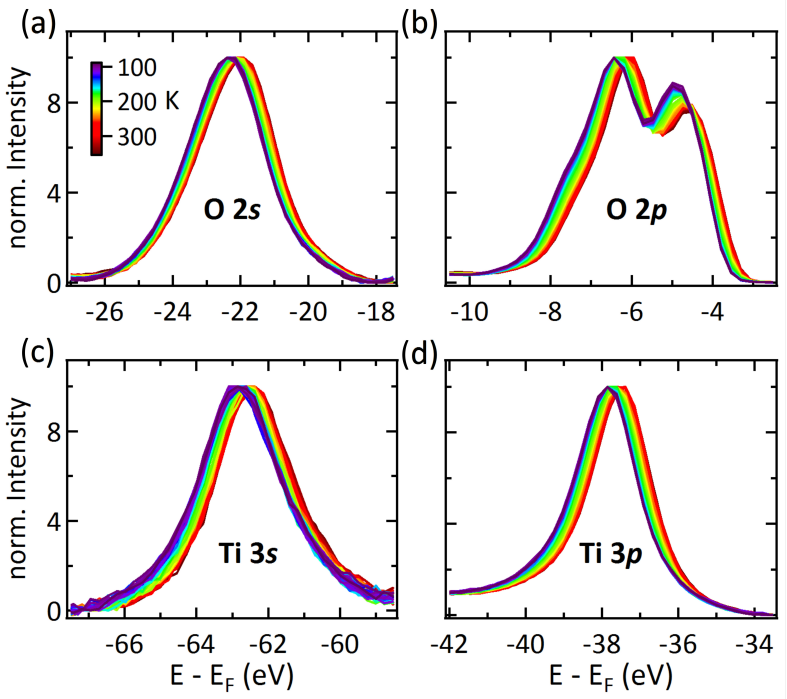

Figure 5.16: Temperature dependence of the different core-levels (a) O 2s, (c) Ti 3s and (d) Ti 3p as well as (b) the O 2p valence band for 80 K $\leq T \leq$ 380 K measured with $h\nu = 200$ eV and p-polarization at $p_{O_2} = 10^{-11}$ mbar. All spectra are normalized to the background intensity and the temperature scale is given in (a).

In order to clarify this assertion the electronic properties of the O 2s, O 2p, Ti 3s and Ti 3p states are studied with respect to T changes in the same temperature range of 80 K $\leq T \leq$ 380 K. The corresponding results are illustrated in Figure 5.16 (a) - (d). All core-levels consistently shift to lower binding energies by increasing the temperature. The same trend holds for increasing p_{O_2} as seen in Figure 5.13. At a low sample temperature T and in the presence of a low p_{O_2} in the experimental chamber the illumination of the BTO films by synchrotron light effectively creates OV at the surface of BTO. The resulting potential gradient at the surface induces a continuous downward bending of all electronic states at the vicinity of the surface illustrated in Figure 2.8. Consequently, the Ti 3d derived conduction band appears below E_F [22, 23, 93] which leads to the emergence of the QPS in the ARPES spectra.

5.4 2DEG depletion model

The temperature of the sample and the partial pressure p_{O_2} severely influence the electronic structure of the BTO thin films. In particular, the response of the 2DEG and distinct core-levels based on variations in T and p_{O_2} is already studied qualitatively in the previous two subsection. However, the behavior of the electronic states follows a certain regularity. In this section, the band bending is evaluated quantitatively. Furthermore, a model is introduced which describes the creation (depletion) of a 2DEG due to T decrease (increase) by means of the total electron density n_e.

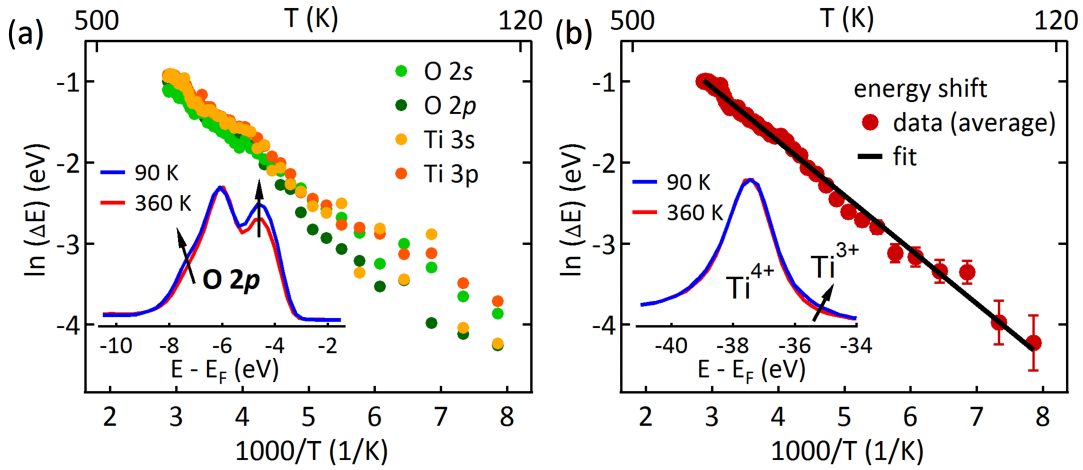

Figure 5.17: Energy shift ΔE of the core-level and valence band spectra as a function of T presented in an Arrhenius plot. (a) ΔE of the individual O $2s$, O $2p$, Ti $3s$ and Ti $3p$ states. (b) Average ΔE involving all ΔE in (a). The insets compare the spectral shape of the O $2p$ valence band in (a) and the Ti $3p$ core-level in (b) for $T = 80$ K and 300 K.

First, the energy shifts $\Delta E = |E(T) - E(80\,\mathrm{K})|$ of the O $2s$, Ti $3s$ and Ti $3p$ core-levels and the O $2p$ valence band in Figure 5.16 as a function of T are considered in more detail. In Figure 5.17 (a) the individual results of all electronic states (green dots for oxygen states and yellow/orange for titanium states) are presented in an Arrhenius plot, *i.e.* $\ln(\Delta E)$ is plotted versus $1000/T$. Figure 5.17 (b) displays the average value of ΔE for all the core-levels and the valence band from Figure 5.17 (a) by red dots and is plotted accordingly. The error bars are estimated by the standard deviation. The overall linear behavior in Figure 5.17 (b) indicates that the energy shift follows the exponential law $\Delta E = \alpha\, e^{-\beta/k_B T}$. From the slope and the intercept of a linear fit indicated by the black line it is possible to determine the magnitude of the input parameters to $\alpha = 2.5$ eV and $\beta = 57$ meV. This observation suggests that in the BTO

thin films the band bending does not emerge continuously over T but is rather T-dependent so that $\Delta E = \Delta E(T)$. α represents the maximal shift $\Delta E(T = \infty)$ - $\Delta E(T = 0)$ due to band bending and β might correspond to some kind of energy threshold for the onset of band bending. A non-linear band bending might arise from a T-dependent surface potential.

In addition to the energy position also the line shape of distinct electronic states is varying with T. For instance, by decreasing T, a clear shoulder at $\approx E_\mathrm{F}$ - 7.5 eV and an increase in spectral weight at $\approx E_\mathrm{F}$ - 4.5 eV becomes visible in the O $2p$ valence band illustrated in the inset of Figure 5.17 (a) by black arrows. This indicates that an increased density of OV at the surface of the BTO films at low T affects the surface stoichiometry. A similar observation has been made for the Ti $3p$ core-level where a weak shoulder at the lower binding energy side appears at lower T shown in the inset of Figure 5.17 (b). The shoulder can be attributed to a rise in the Ti^{3+} concentration of the system which is related to a larger number of oxygen defect sites at the surface [93].

A similar temperature study was performed for the electronic states near E_F. Therefore, the spectral weight of the QPS and the ICS in Figure 5.15 is added up like in the inset of Figure 5.14 (c). The integrated ARPES intensity $\mathrm{I_{PES}}$ is plotted as a function of T according to the Arrhenius law. Figure 5.18 (a) displays the experimental results of $\mathrm{I_{PES}}$ at $\bar{\Gamma}_{00}$ (orange) and $\bar{\Gamma}_{10}$ (red). For both high-symmetry points a similar T dependence is observed, namely an exponential decrease in $\mathrm{I_{PES}}$ for higher T. As $n_e \propto \mathrm{I_{PES}}$, the behavior in Figure 5.18 (a) nicely illustrates the depletion of charge carriers at the surface with temperature. In other words, OV from the surface migrate into the bulk as a function of T. The onset of this mechanism is estimated from the slope of $\mathrm{I_{PES}}$ at elevated T (see dashed line). The result is an activation energy of $E_A \approx 0.25$ eV and an onset temperature of ≈ 285 K. However, E_A changes for different temperature ranges so that it cannot be considered as an universal constant. The appearance of the QPS and the ICS at E_F is closely related to the T-dependent energy shift $\Delta E(T)$ in the core-level and valence band spectra.

In total, the electron density for a 2DEG up to E_F can be described by [208]

$$\begin{aligned} n_e &= \int_0^\infty dE \frac{g_{2D}}{1 + e^{(E-E_\mathrm{F})/k_B T}} \\ &= g_{t_{2g}} k_B T \ln\left(1 + e^{E_\mathrm{F}/k_B T}\right), \end{aligned} \tag{5.1}$$

where g_{2D} represents the energy independent density of states of the 2DEG. The band bending $\Delta E(T)$ in the conduction and valence band also affects the position of E_F. Therefore, the Fermi level $E_\mathrm{F}(T)$ with respect to the bottom of the CB is also T-dependent: $E_\mathrm{F}(T) = E_\mathrm{F}^0 - \Delta E(T)$ where E_F^0 is the Fermi level pinning at $T = 0$ K. The

analysis of the core-level data leads to an independent evaluation of $\Delta E(T)$ which then can be applied in the formula.

The ARPES results shown in Figure 5.18 (a) can be fairly well fit according to Equation (5.1). This indicates that the 2DEG model nicely describes the electron depletion within the experimental data. The best fit shown by a black solid curve leads to a Fermi level pinning of $E_F^0 \approx 0.35$ eV at $T = 0$ K. This value is in good agreement with the result from the band gap consideration ($E_F^0 \approx 0.28$ eV) discussed in Figure 5.5.

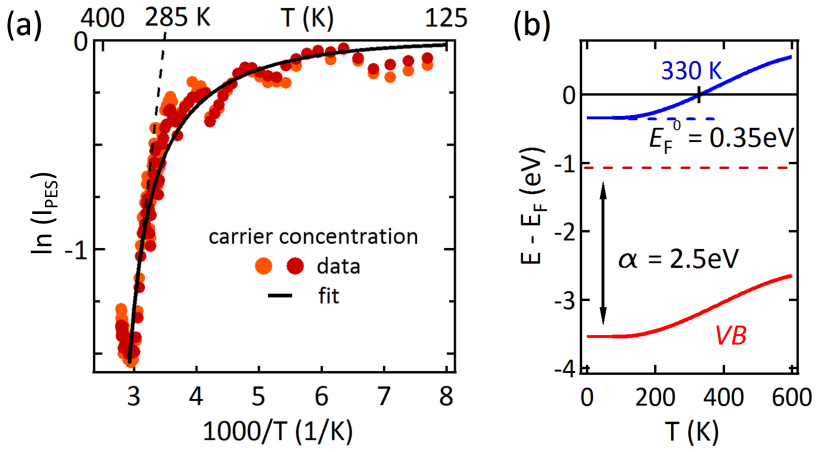

Figure 5.18: 2DEG depletion model in BTO thin films. (a) I_{PES} at $\bar{\Gamma}_{00}$ (orange) and $\bar{\Gamma}_{10}$ (red) is fitted to an established model (black solid line) in an Arrhenius plot. (b) Sketch of the band bending as a function of T presenting all parameters extracted by the fitting procedure.

The sketch in Figure 5.18 (b) summarizes the band picture in the BTO films as a function of temperature. Including the band bending $\Delta E(T)$ deduced from the core-level data in Figure 5.17 the behavior of the conduction band (CB) in blue can be described schematically. The conduction band shifts from E_F^0 to above E_F by increasing T and it crosses E_F at $T \approx 330$ K. In a rigid band picture the energy difference of the conduction band (blue) and the valence band (VB) in red is preserved so that the valence band shifts consistently. In the low T case, the energy position of the valence band lies $\alpha = 2.5$ eV below the virtual valence band pinning for $T \to \infty$ illustrated by a red dashed line. The valence band pinning is connected to the charge neutrality level of extrinsic defects [209].

In summary, the change in the electronic structure with T is induced by a band bending effect which itself depends on T. Since also the oxygen defect concentration at the surface is varying with T represented by the O $2p$ and Ti $3p$ states in the inset of Figure 5.17, OV are assumed migrate from surface to bulk. In particular, the response of the designated charge carrier density with T strongly resembles the corresponding

results for p_{O_2} presented in Subsection 5.3.5. Thereby, the complex interaction of negatively charged electrons e' and positively charged oxygen defects $V_O^{\cdot\cdot}$ is described by the Poisson-Boltzmann theory [206]. The changes in spectral weight of the QPS and the ICS as a function of p_{O_2} and T dependence might be explained by the same theory. The mechanism for oxygen accumulation and depletion at the surface, however, differs in both cases. In the p_{O_2}- (T-) dependence the deviation in the oxygen defect concentration is effected by reoxidation (oxygen migration) [210].

5.5 Outlook

One crucial onset parameter for oxygen diffusion is given by the activation energy E_A. In the thin BTO films E_A has been determined to be ≈ 0.25 eV which contradicts with typical bulk values of 0.6-1.2 eV [206, 211]. These bulk values of E_A correspond to much higher diffusion onset temperatures than the estimated T for the thin BTO films (≈ 285 K). In a recent study, however, it has been shown that finite-size and interface-proximity effects lead to a reduction of the activation enthalpy in thin films [97]. This effect is related to a change in the critical radius r_c describing the spacing between cation A and B in a ABO_3 perovskite [212]. Lowering the inverse critical radius r_c^{-1} also reduces the oxygen vacancy migration enthalpy [206]. A change of the lattice parameters, hence, tunes E_A and also influences the onset temperature. Indeed, a subsurface migration of oxygen defects has been confirmed for bulk anatase TiO_2 to set in at ≈ 200 K [213].

A small onset temperature for oxygen diffusion of ≈ 285 K does not allow a controllable manipulation of the (surface-) conductivity at room temperature. This hampers the functionality of non-volatile devices based on BTO thin films. Below a critical carrier concentration [156, 157, 163] and above a critical film thickness [214, 215] ferroelectricity in BTO prevails. In such cases the ferroelectric polarization fields might additionally enhance defect migration. This study clearly demonstrates that defect dynamics can crucially influence the electronic response at the surface and interface of oxide heterostructures. In order to accomplish a steady performance of oxide application, defect effects within this devices need to be carefully considered and understood.

Another important finding of this study is the $p_{O_2}^{-1/6}$ scaling behavior of the OV upon changes in p_{O_2}. Considering the charge neutrality condition [206] discussed in Subsection 5.3.5, this implies a primarily 2+ charge state of the OV. In other words, 2+ is the most stable ionization state of the oxygen defects in the BTO thin films, under the conditions of a free carrier density of $n \approx 2 \times 10^{21}$ cm^{-3} and a charge neutrality level at least 0.35 eV above the conduction band edge. This result is in contrast to

observations for STO bulk crystals where the carrier density scales with $p_{O_2}^{-1/4}$ at low T [97]. Assuming solely oxygen defects, this scaling behavior refers to an associated charge state of 1+ for the OV. Accidental acceptor doping additionally can affect the charge state in oxide materials, *e.g.* in BTO [204]. In the case of a charge state of 1+ the OV in STO cause the appearance of an in-gap state in the electronic structure [34] that might induce electron correlation at the oxygen defect site. The in-gap state is regarded as a local magnetic moment which might cause other emerging phenomena in STO, as the Kondo effect [216] or surface ferromagnetism [217]. In BTO thin films, neither a pronounced localized defect state in the ARPES spectra nor a $p_{O_2}^{-1/4}$ scaling behavior has been observed. These results suggest the absence of such a local magnetic moment so that similar effects as the ones observed in STO are scarcely to be expected.

In order to substantiate the findings on defect migration in BTO, an identical study (dependence of the QPS on T and p_{O_2}) has to be conducted on BTO single crystals. As these bulk systems lack of an underlying substrate (in contrast to Nb-doped STO used in the BTO thin films) a possible impact on the electronic structure of BTO by the adjacent STO substrate can be excluded. In addition, the property of a strong OV diffusion from surface to bulk is not only restricted to BTO [213]. Hence, other related systems (STO, TiO_2, etc.) might exhibit a comparable T- and p_{O_2}-dependence of the 2DEG at their surface under certain conditions. In further quantitative studies, by following the approach in this chapter, the volatile or non-volatile nature of these other TMO ought to be determined. These results, in total, then might lead to an universal picture of OV migration in TMO and reviews their implementation in room temperature applications.

CHAPTER 6

HYBRID SYSTEM Bi/$BaTiO_3$

The two material systems of interest in this thesis, namely the Bi film grown on the BTO substrate (discussed in Chapter 2) possess particular physical properties which make them attractive for future applications. BTO, on the one hand, is ferroelectric at room temperature [37] with further structural phase transitions at lower temperatures [103]. As other nominally d^0 TMO [22–24] BTO displays conductivity at its surface (see Chapter 5). On the other hand, Bi as a heavy element exhibits strong spin-orbit coupling which results in a spin-splitting of its electronic states [120], in particular, at its surface [132]. The combination of both materials might lead to a coupling of their individual properties as already shown theoretically [60]. Here, the preparation of the model system Bi/BTO is realized followed by a subsequent characterization of its surface crystal structure. The main focus of this chapter lies on the determination of the electronic structure of Bi/BTO via ARPES. Parts of the presented data has already been published in Ref. [218].

6.1 Surface structure

As shown in Section 4.1 the preparation of BTO according to Ref. [159] leads to a (2×1) reconstruction of the BTO surface, with a TiO_2 termination and a considerable small doping of the sample itself. In addition, it is expected that the polarization within the individual domains in the BTO substrate are oriented along the [0 0 1] direction according to Ref. [163]. The thin Bi films which are investigated in this chapter are evaporated on such a freshly prepared BTO substrate as presented in Subsection 3.8.2. In order to understand the electronic properties of the hybrid system or Bi/BTO it is

necessary to characterize the film growth and the actual film thickness. The next two subsections present the surface structure of the Bi/BTO system as studied via LEED and XPS.

6.1.1 Characterization by low energy electron diffraction (LEED)

In Figure 6.1 two representative LEED patterns of a Bi film with 8 ML thickness are shown:

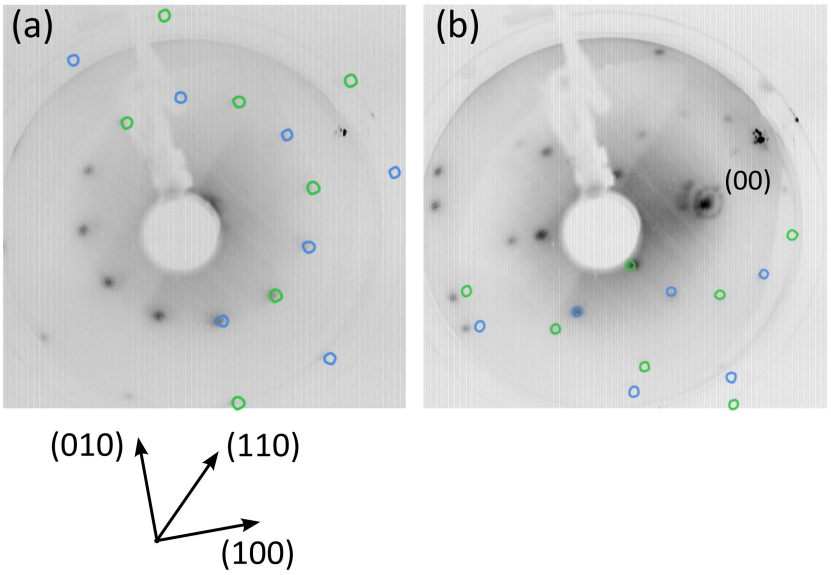

Figure 6.1: Two LEED patterns of the same 8 ML thick Bi film on BTO measured with a beam energy E_0 of 39.3 eV under normal incidence in (a) and with $E_0 = 58.2$ eV for a tilted measuring geometry in (b). The two different Bi domains are highlighted by blue and green circles.

The spots are directly compared to simulated LEED patterns generated by LEEDpat30 (colored circles). From the input parameters of the simulation the following characteristics of the Bi films can be deduced. The films consist of two hexagonal domains illustrated by green and blue circles which are 90° rotated with respect to each other. This results in an inner ring which consists of twelve spots and in additional high order spots which are displayed at Figure 6.1 (a) and (b), respectively. Variations between the simulated and measured spots, especially for the higher order spots, are due to enhanced radial distortions from the center to the edge of the screen in the LEED optics [219].

The hexagonal structure suggests that the films are oriented parallel to the hexagonal Bi(0001) plane which is equal to the rhombohedral Bi(111) plane (see Section 2.2) [122]. Note that the BTO substrate is four-fold symmetric in the case of a (1×1) as well as a (2×1) surface reconstruction. In the latter case the presence of two equivalent domains which are oriented along perpendicular directions ensures the

four-fold symmetry. The merging of a hexagonal film with a four-fold substrate results in a two-fold domain structure. As a consequence, the Bi films form two equivalent domains which are rotated by 90° with respect to each other. Both, the (1 × 1) and (2 × 1) surface reconstruction in BTO lead to the observed two-fold domain structure for the deposited Bi films. The film quality in the latter case, however, is considerable higher as the (2 × 1) reconstruction might induce a preference in the orientation of the deposited films.

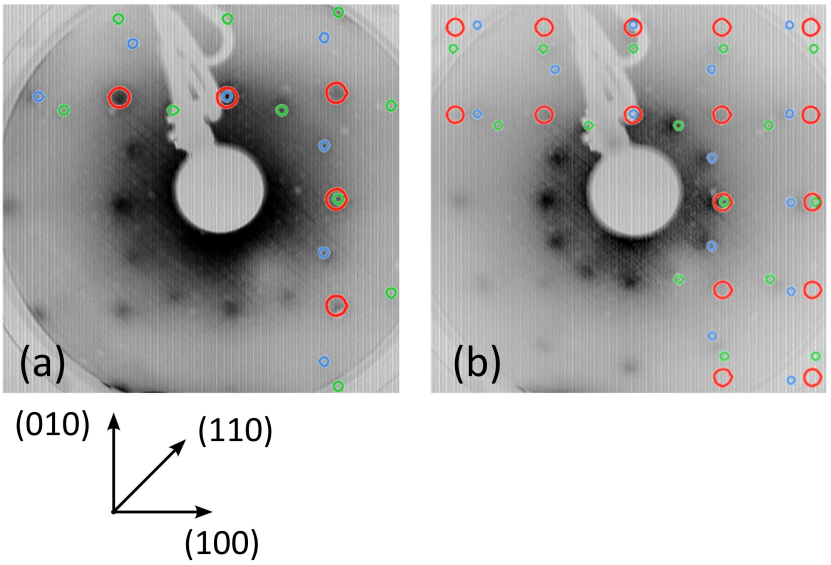

Figure 6.2: Two LEED patterns of the same 4 ML thick Bi film on BTO measured at $E_0 = 61.0$ eV in (a) and $E_0 = 100.7$ eV in (b) under normal incidence. The blue and green circles indicate the LEED pattern for the two different Bi domains and the red circles the LEED pattern of the BTO substrate.

Similar results have already been observed for Bi/Si(001). Thereby, the deposition of Bi on a nominally (2 × 1) reconstructed Si surface give rise to hexagonal Bi(0001) films which also exhibit a two-domain structure in the LEED pattern [220, 221].

In a Bi/BTO system with a rather low film thickness both the film and the substrate spots appear in LEED. Figure 6.2 illustrates the case for a 4 ML thick Bi film on BTO measured at two different beam energies. The Bi spots are indicated by blue and green circles where each color represents one of the respective film domains. The BTO substrate spots, on the other hand, are illustrated by red circles. On closer inspection, the position of the (10) and (01) spots for BTO(001) and Bi(0001) coincide along the [1 0 0] direction (green domain) and along [0 1 0] direction (blue domain), respectively. In the simulated LEED pattern (colored spots) the lattice constants of pure Bi and BTO are regarded. Their ratio is $a_{\mathrm{BTO}} / a_{\mathrm{Bi}} \approx 101.5\,\%$ along [1 0 0] and $8\,a_{\mathrm{BTO}} / 7\,a_{\mathrm{Bi}} \approx 100.4\,\%$ along [0 1 0] with respect to the green domain. By reversing the consideration for [1 0 0] and [0 1 0] direction the same results hold for the blue domain. The high lattice match suggests a film growth without built-in stress. This leads to

the assumption of an epitaxial film growth with a high crystalline quality of the films. In order to confirm the growth mode and the exact film thickness the Bi/BTO system was further characterized by XPS as discussed in the next section.

6.1.2 Characterization by X-ray PES (XPS)

To further characterize the film growth XPS measurements were performed. By means of these measurements also an accurate estimation of the film thickness is possible [173, 222]. In Figure 6.3 the intensity of the most prominent core-levels of substrate (Ba $3d$) and film (Bi $4f$) are given depending on the layer thickness (2 – 12 ML):

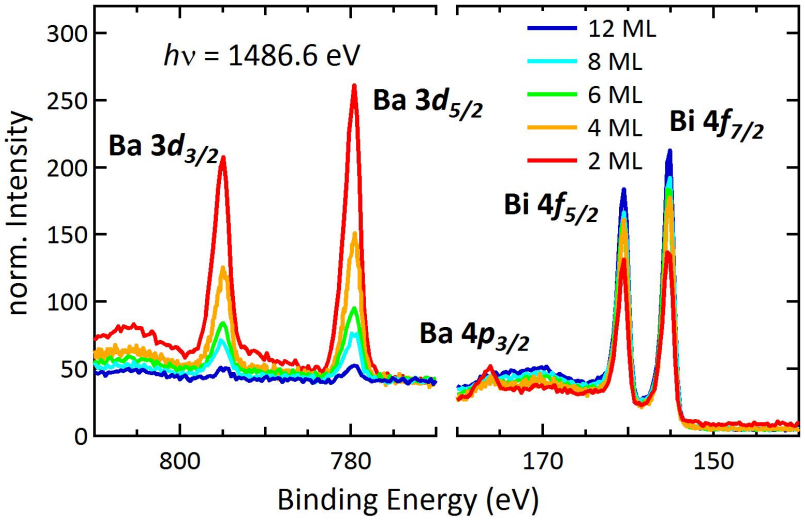

Figure 6.3: Intensity variation of the Ba $3d$ and Bi $4f$ core-levels in Bi/BTO as a function of film thickness measured with an Al-K_α source. All spectra are normalized to the background intensity.

The intensity of the Ba $3d$ peaks strongly decreases for higher thicknesses while the Bi $4f$ peak intensities increase and gradually saturate at 8 – 12 ML. A quantitative analysis is accessible by plotting the ratio of the Ba $3d$ and Bi $4f$ peak areas as a function of n_{eff}, where n_{eff} is the effective layer thickness taking into account the nominal film thickness n_{Bi} and the photoelectron take-off angle ϑ. In order to obtain the areas of the core-level a linear background is subtracted from the XPS spectra and the respective peaks are fitted by Voigt profiles.

In Figure 6.4 the dependency of the peak area ratio on n_{eff} is illustrated. One part of the data concerning the peak area ratio is extracted from Figure 6.3 for different layer thicknesses n_{Bi} (between 2 – 12 ML) and for normal emission. Additional data points stem from measurements varying the take-off angles ϑ between 0° and 60°. For the sake of clarity the data points which belong to a specific n_{Bi} are drawn with the same color and marker. The error bars are estimated from an uncertainty in the

fitting process. As a homogeneous film growth with constant thickness is assumed the experimental data is fitted to a corresponding model [173] which yields:

$$f(n_{\mathrm{eff}}) = \frac{s_{\mathrm{Ba}}}{s_{\mathrm{Bi}}} \cdot \frac{e^{-r n_{\mathrm{eff}}/\lambda_{\mathrm{Ba}}}}{(1 - e^{-r n_{\mathrm{eff}}/\lambda_{\mathrm{Bi}}})}; \quad n_{\mathrm{eff}} = n_{\mathrm{Bi}}/\cos\vartheta \tag{6.1}$$

The prefactors $s_{\mathrm{Ba}} = 12.5$ and $s_{\mathrm{Bi}} = 9.1$ are the atomic sensitivity factors [223, 224]. Photoelectrons which are excited from the Ba $3d_{5/2}$ and Bi $4f_{7/2}$ core-levels have a kinetic energy of 702.6 eV and 1327.2 eV, respectively. From these values the corresponding inelastic mean free paths (IMFP) can be deduced to $\lambda_{\mathrm{Ba}} = 15.6$ Å and $\lambda_{\mathrm{Bi}} = 25.0$ Å [225]. With respect to the lattice constant of Bi a_{Bi} the IMFP amount to $\lambda_{\mathrm{Ba}} = 3.99$ ML and $\lambda_{\mathrm{Bi}} = 6.35$ ML (1 ML = 3.94 Å [122]). The only free fitting parameter r depicts an artificial "error" factor. A deviation of r from unity implies a slight imperfection and non-uniformity in the Bi coverage. The proposed model fits the experimental data for a value of $r = 1.09$. This confirms the nominal film thickness assumed by the calibration of the evaporator and is also in line with the growth of homogeneous films with constant thickness. Other growth modes, however, lead to other dependencies of $f(n_{\mathrm{eff}})$. In the case of island formation on top of a flat surface, *e.g.*, $f(n_{\mathrm{eff}})$ would change linearly with respect to the film thickness [222].

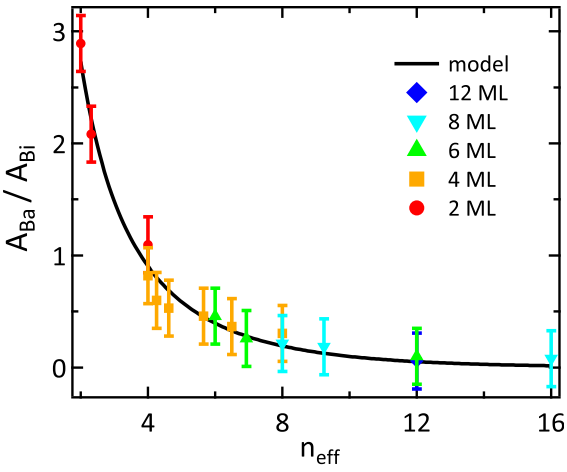

Figure 6.4: Quantitative analysis of the peak area ratio of the Ba $3d$ and Bi $4f$ core-levels in Bi/BTO by varying n_{eff}. The experimental data points are fitted to a model for homogeneous film growth with constant thickness (solid black line).

The validity of $f(n_{\mathrm{eff}})$ was confirmed in additional experiments, for instance, by comparing angle-integrated spectra of the Bi $5d$ core level and the O $2p$ valence band measured with He IIα excitation ($h\nu = 40.84$ eV). Figure 6.5 presents the spectra as a function of n_{eff}. Here, the layer thickness of the respective Bi films is between 4 –12 ML and the take-off angle ϑ for the 4 ML case is varied between 0° and 60°. The part of the spectra which is at higher kinetic energies (≥ 20 eV) was multiplied by a factor of 8 in order to better visualize the peak area changes. In the inset the peak area

ratio of the Bi 5d core level and the O 2p valence band is plotted as a function of n_{eff} and fitted according to $f(n_{\mathrm{eff}})$. As the atomic sensitivity factors of this energetic states are lacking, the cross sections have been used instead [175]. In general, the analysis of the peak area ratios exhibits the same trend as for the core-level data and the experimental data could be fitted with $f(n_{\mathrm{eff}})$. The "error" factor r, however, is considerable larger ($\approx 20\,\%$) due to the small number of data points, the uncertainties in evaluating the O 2p peak area and inconsistencies in the input parameters of $f(n_{\mathrm{eff}})$, specifically the sensitivity factors.

As shown in the characterization by LEED and XPS the Bi films grow epitaxially on BTO by forming a homogeneous and flat surface. The quality of the surface structure of hybrid Bi/BTO allows a detailed investigation of its electronic structure as presented in the following.

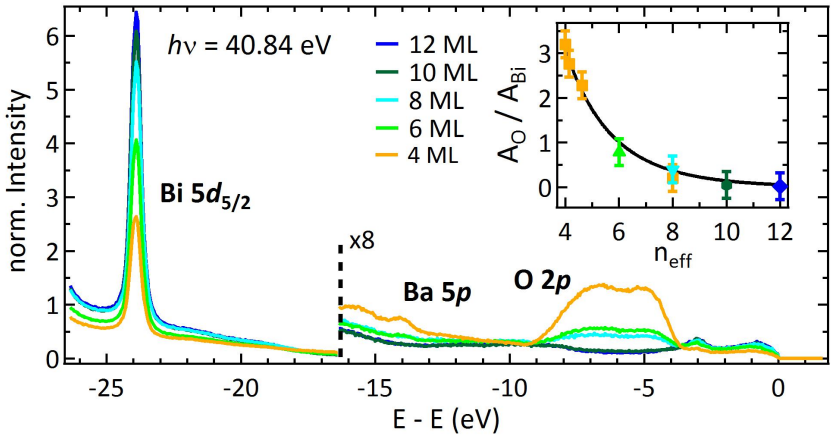

Figure 6.5: Determination of growth mode and layer thickness by the analysis of the O 2p valence band and the Bi 5d core level peak area ratios measured with He IIα excitation. All spectra are normalized to the background intensity.

6.2 Electronic structure

At first the electronic structure of Bi/BTO(001) with a certain film thickness of 8 ML is studied. All the measurements of this system were performed by He I$_\alpha$ excitation ($h\nu = 21.22$ eV) at a temperature of 60 K. The obtained results can be directly compared to the LEED pattern given in Figure 6.1.

Constant energy maps provide insight into the symmetry of the respective system (see Subsection 4.2.1). The most prominent of these maps in the case of Bi is its peculiar Fermi surface [226]. The related Fermi surface of the Bi/BTO(001) system is presented in Figure 6.6 (a). As in pure Bi or Bi/Si(111) [128, 226] the Fermi surface of

Bi/BTO(001) consists of an electron pocket near the $\bar{\Gamma}$-point and elongated hole and electron pockets along the $\bar{\Gamma}-\bar{M}$ direction. The shape of the electron pocket near the $\bar{\Gamma}$-point in Bi/BTO(001), though, resembles rather a ring than a hexagon. In addition, the number of the star-shaped lobes pointing towards the $\bar{M}/\bar{M}'$-point has changed from six to twelve in contrast to Bi or Bi/Si(111). These observations can be linked to an electronic picture of two superimposed but separated SBZ which are rotated by 90° with respect to each other (see Figure 6.6 (b)). The coexistence of two Bi domains on the surface of Bi/BTO(001), hence, is also reflected in its electronic structure. This is in strong accordance to the results observed in LEED.

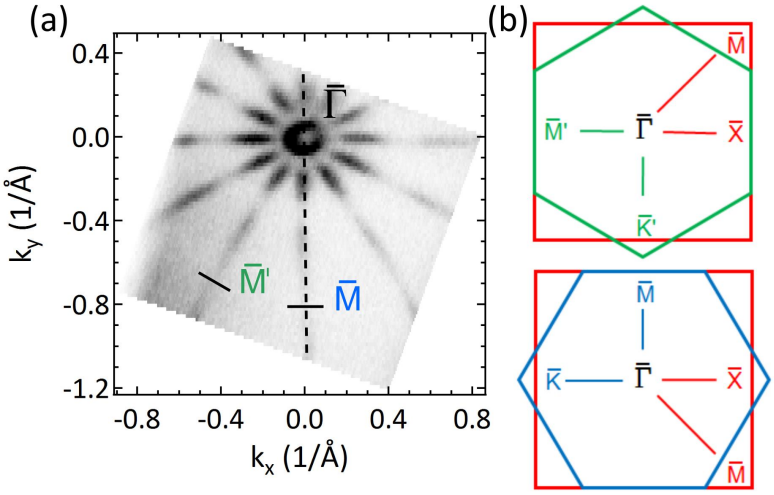

Figure 6.6: (a) Fermi surface of a 8 ML thick Bi(0001) film on BTO(001). The high-symmetry points $\bar{M}'$ and $\bar{M}$ (green and blue) correspond to the SBZ of the two different domains. (b) A schematic picture of both SBZ with respect to the substrate is shown.

The predominant SBZ of Bi (green and blue) and their orientation with respect to the SBZ of BTO (red) are illustrated in a schematic (see Figure 6.6 (b)). Since the lattice vectors of Bi(0001) and BTO(001) along one direction for one domain (and along the other direction for the other domain) almost match in real space (see previous section) the same holds for the corresponding reciprocal lattice vectors g_{Bi} of Bi along $\bar{\Gamma}-\bar{M}$ and g_{BTO} of BTO along $\bar{\Gamma}-\bar{X}$. Their ratio accounts to $g_{\mathrm{Bi}}/g_{\mathrm{BTO}} \approx 100.8\%$ so that the $\bar{M}$-point of Bi(0001) coincides with the $\bar{X}$-point of BTO(001).

In the schematic the high-symmetry direction $\bar{\Gamma}-\bar{M}$ of, *e.g.*, the blue domain overlaps with the $\bar{\Gamma}-\bar{K}'$ direction of the green domain and *vice versa*. This leads to the assumption that the electronic structure of Bi/BTO, in total, displays the electronic features of both high-symmetry directions. Therefore, a representative band structure as shown in Figure 6.7 is regarded. The band dispersion along the high-symmetry directions is extracted from the 3D data set along the black dotted line in Figure 6.6. Indeed, signatures of both high-symmetry directions appear in the spectra. The electronic branch α at the center of the SBZ corresponds to the inner ring of the Fermi surface and is present in both high-symmetry directions. Its continuation at

higher k-values can be assigned to the $\bar{\Gamma}-\bar{\mathrm{M}}$ direction of one particular domain (here blue) by comparison with previous studies on Bi [130, 132, 227]. In the same manner β is attributed to the $\bar{\Gamma}-\bar{\mathrm{M}}$ direction of the same domain (blue) and γ to the $\bar{\Gamma}-\bar{\mathrm{K}}'$ direction of the other domain (green). The strong intensity at E - $E_{\mathrm{F}} \approx 0.4$ eV stems from a surface resonance (SR) located in the bulk projection band [130, 227].

The anisotropic splitting of the surface states and the peculiar dispersion of the bands in Figure 6.7 result from the strong spin-orbit coupling in Bi. This has already been demonstrated in first-principle calculations considering either the electronic structure on the surface of Bi(0001) [132] or in thin Bi films [228]. In Figure 6.8 (b) the experimental data is directly compared to the corresponding calculation for a 10 ML thick Bi(0001) film extracted from Ref [228, 229]. In order to nicely resolve the distinct electronic features the band structure of Figure 6.7 was processed by a 2$^{\mathrm{nd}}$ derivative method [177]. The theoretical band structure is indicated by red dots and reproduces the experimental electronic structure for both high-symmetry directions. It is plotted along $\bar{\Gamma}-\bar{\mathrm{M}}$ for negative k-values and along $\bar{\Gamma}-\bar{\mathrm{K}}'$ direction for positive k-values.

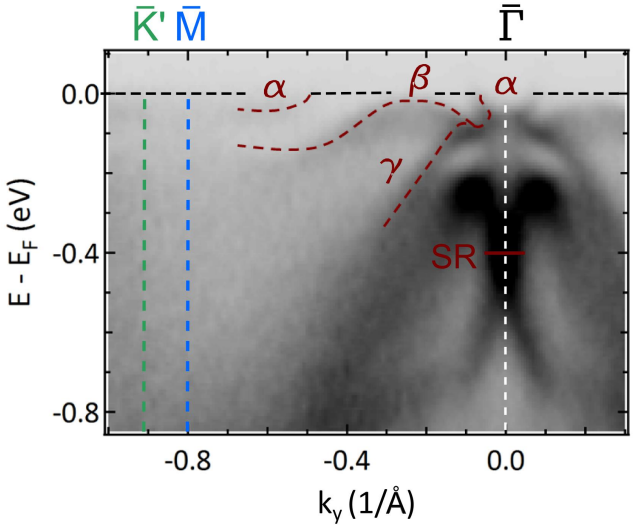

Figure 6.7: Band structure of a 8 ML thick Bi(0001) film on BTO(001). α, β and γ represent the spin-split surface states in $\bar{\Gamma}-\bar{\mathrm{M}}$ (α and γ) and in $\bar{\Gamma}-\bar{\mathrm{K}}'$ (α and γ) direction. SR is the surface resonance.

Strong spin-orbit coupling in Bi, moreover, leads to spin polarization among the electronic states. For instance, the bulk continuum states at binding energies up to ≈ 3 eV (including the SR) are Rashba spin split [230]. The most significant degree of spin polarization, however, occurs in the surface bands: α can be assigned to the spin-up branch whereas β and γ correspond to the spin-down branch [231] with respect to the in-plane spin quantization axis. In pure Bi(0001) or Bi/Si(111) this leads to a vortical spin structure as illustrated in the schematic Fermi surface (see Figure 6.8(a)). Next to the in-plane spin component oriented along $\bar{\Gamma}-\bar{\mathrm{M}}$ an out-of-plane component along $\bar{\Gamma}-\bar{\mathrm{K}}'$ is present [232]. In the case of hybrid Bi/BTO(001) with its two-domain structure both high-symmetry direction overlap so that also both spin components

should be available at the same time.

Although the electronic structure of Bi has been extensively studied still some questions remain unsolved until now. In general, Bi can be driven into a topological phase by doping it with Sb [111]. Whether a topological phase appears in a pure Bi system, for instance at a certain layer thickness, is still under debate. It is not completely solved if Bi itself can be regarded as a topological insulator, a non-trivial semimetal or just a trivial material [233, 234]. For a concrete characterization of Bi it is necessary to know the electronic structure in the vicinity of the $\bar{\text{M}}$-point. As the region of interest is embedded in the bulk projection band a determination of Bi with respect to its topological behavior is hardly possible.

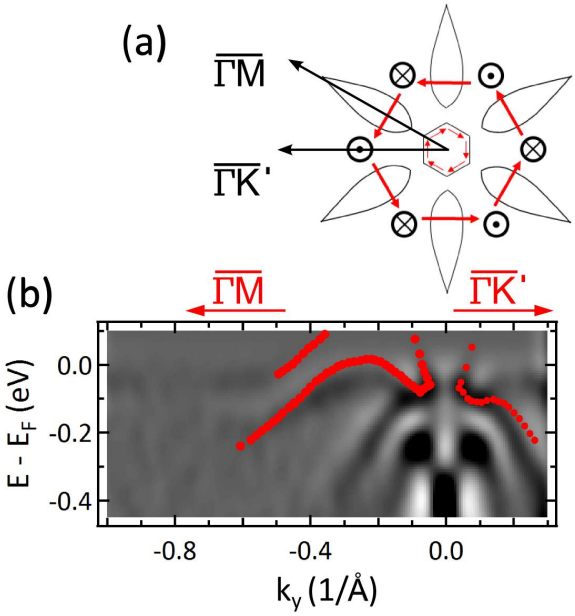

Figure 6.8: (a) Schematic Fermi surface of Bi(0001) with the in-plane [231] and out-of-plane [232] spin polarization of the spin-split surface states. (b) Direct comparison of the experimental and theoretical band structure of Bi along $\bar{\Gamma} - \bar{\text{M}}$ and $\bar{\Gamma} - \bar{\text{K}}'$. The electronic structure calculation is highlighted by red dots (taken from [228]) and agrees nicely with the experiment.

6.3 Thickness dependence

As seen the electronic structure of Bi/BTO(001) for a thickness of 8 ML resembles the one of pure Bi and Bi/Si(111) [128, 226]. A change in the coverage of the Bi films, however, might have an effect on its surface states and on the electronic properties of the whole system. This fact for instance is reflected in a semimetal-to-semiconductor transition for very high film thicknesses (≥ 180 ML) [235, 236]. For that instance, the band structures for thicknesses of 16 ML (a), 8 ML (b) and 4 ML (c) are displayed and compared in Figure 6.9.

The quality of the electronic bands strongly depends on the film thickness. In total, they get sharper for thicker Bi films. Nevertheless, at the low film thickness of 4 ML the bands are still nicely resolved. This is due to the absence of an additional Bi{012}

phase as observed in Bi/Si(111) for lower coverages than ≤ 6 ML [237]. In addition, the gap between the surface band and the SR becomes smaller as highlighted by the red solid and dotted lines as well as the red arrow. This observation seems to be in contrast to similar studies on Bi/Si(111) where the films are considered to be "freestanding" [128].

In order to determine the influence of the film thickness on the electronic structure in more detail, EDC at the $\bar{\Gamma}$-point and momentum distribution curves (MDC) at E_F are studied. The corresponding line spectra are presented in Figure 6.10 (a) and (b), respectively. In addition, the position of the top of the SR is plotted as a function of the film thickness (see Figure 6.10 (c)). Thereby, the data is extracted from the respective PES spectra in Figure 6.9 and compared to theoretical values adapted from Ref. [228].

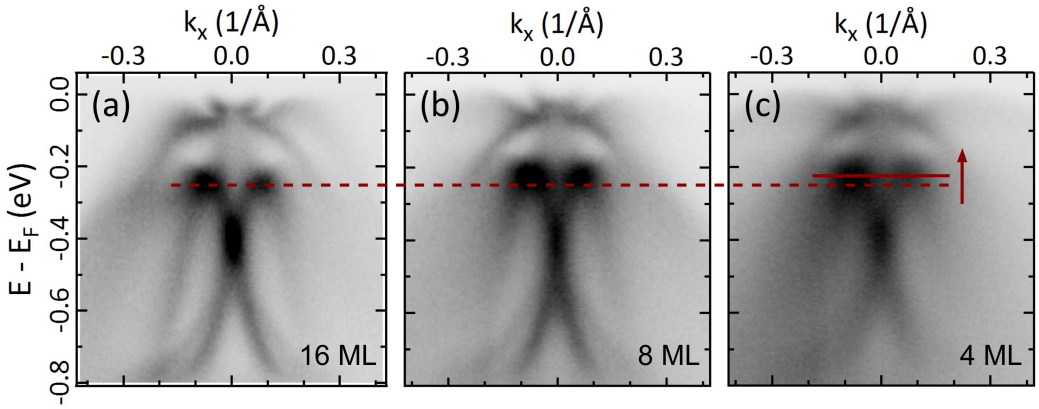

Figure 6.9: Band structure of Bi/BTO(001) for three different layer thicknesses of Bi: 16 ML in (a), 8 ML in (b) and 4 ML in (c), measured along the $\bar{\Gamma} - \bar{M}$ direction. The sample temperature was 60 K for 16 ML and 8 ML and 100 K for 4 ML. By reducing the Bi coverage the top of the SR shifts towards lower binding energies as indicated by the red arrow.

The EDC curves (see Figure 6.10 (a)) clearly display a shifting of the SR towards lower binding energies for thinner Bi films (black arrow). This has already been shown in the band structure of Bi/BTO (see Figure 6.9). In order to support this observation the energy position of the SR as a function of the film thickness is compared to the corresponding theoretical vales [228, 229] (see Figure 6.10 (c)). The theoretical data, thereby, is shifted towards higher energies (≈ -0.09 eV) with respect to the experimental ones to allow a direct comparison. Moreover, the inaccurate determination of the theoretical value from the respective graphs of Ref. [228] leads to rather large errors along the energy axis. Despite these uncertainties, the theoretical data supports the experimentally observed shift of the SR.

Next to its change in energy, also the PES intensity of the SR located at 0.4 eV varies for different Bi thicknesses (see Figure 6.10 (a)). In particular, the spectral weight is dramatically reduced upon lowering the Bi thickness. This effect can be explained by the character of the SR which is mainly bulk-like [228, 230].

However, not only bulk states, as the SR, vary with the Bi film thickness but also surface states. The surface band α near the $\bar{\Gamma}$-point, *e.g.*, also exhibits a clear thickness dependence. Its Fermi vector k_F shrinks for lower Bi coverages as indicated by black arrows (see Figure 6.10 (b)). These observations, in general, can be attributed to a quantum-size effect which leads to a huge variety of phenomena in Bi, concerning resistivity, magnetoresistance, etc. [235, 238–240].

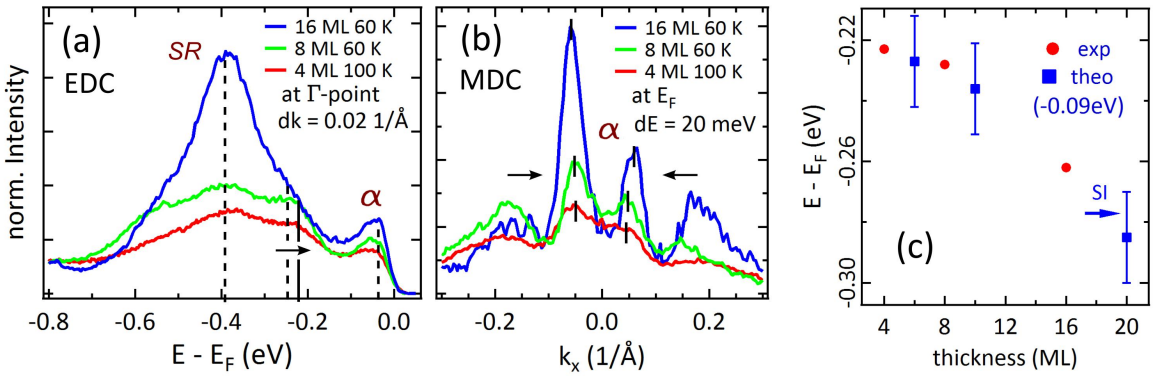

Figure 6.10: Thickness dependence of the extracted EDC (a) and MDC (b) curves of Bi/BTO(001) for different film thicknesses (16 ML, 8 ML and 4 ML). As in Figure 6.9 a shift of the SR for lower Bi thickness is clearly recognizable in the EDC curves in (a). Simultaneously, the intensity of the SR dramatically reduces. In the MDC curves, on the other side, a reduction of k_F of the electron-like surface state α for lower Bi coverage is observed in (b). The spectra in (a) and (b) are normalized to the background intensity. (c) The energy shift of the SR as a function of the Bi thickness, moreover, is quantitatively compared to the theoretical values from Ref. [228].

6.4 Interface state

At large film thicknesses the surface electronic structure of Bi/BTO(001) resembles the one of pure Bi(0001) or Bi/Si(111) [128, 130]. But Bi/BTO(001) exhibits also a significant thickness dependence in its band structure as already shown in the previous section.

The reduction in the film thickness, however, leads to another crucial observation in the electronic structure of Bi/BTO(001), in particular, along the k-points which connect the $\bar{\text{M}}$-points of both domains ($\bar{\text{M}} - \bar{\text{M}}'$ direction). Figure 6.11 displays ARPES

data in the form of waterfall plots of EDC for layer thicknesses of 16 ML in (a), 8 ML in (b) and 4 ML in (c) along this particular high-symmetry line. For higher layer thicknesses (16 ML and 8 ML) the electronic structure of Bi/BTO(001) displays no distinct differences to the one of pure Bi. Near the $\bar{\text{M}}$-points of the two different domains (blue and green) the bulk projection bands of Bi become visible [130, 227].

This is in contrast to the respective band structure of Bi/BTO(001) for a thickness of 4 ML. An additional band appears at the $\bar{\text{M}}$-point of the blue domain. This electronic feature exhibits a hole-like dispersion as highlighted by black bars and is absent in the case of the other domain.

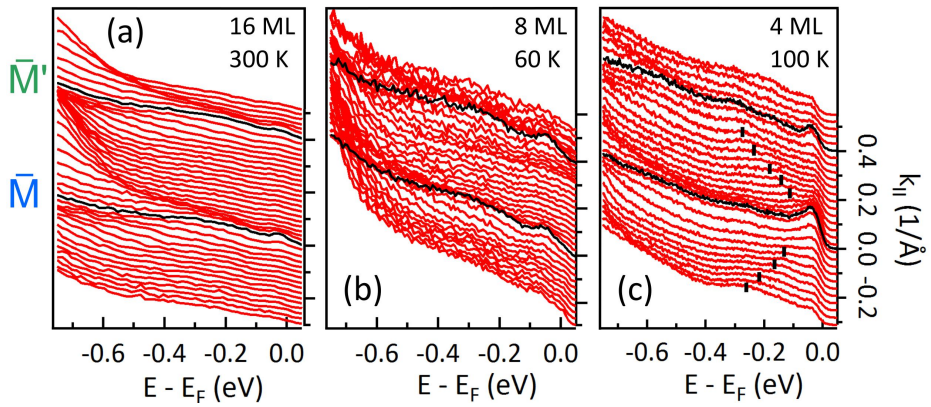

Figure 6.11: Comparison of the electronic structure of Bi/BTO(001) along $\bar{\text{M}} - \bar{\text{M}}'$ direction for systems with a thickness of 16 ML (a), 8 ML (b) and 4 ML (c). The ARPES data are shown as waterfall plots of EDC while the EDC directly at the $\bar{\text{M}}$-point (blue) or $\bar{\text{M}}'$-point (green) are drawn in black. (c) At the low coverage of 4 ML clear traces of an additional state at the $\bar{\text{M}}$-point (blue) are observed as indicated by black bars.

In order to clarify its origin constant-energy cuts at certain energies are investigated as displayed in Figure 6.12. The constant energy maps in Figure 6.12 (a), (b) and (c) correspond to energies of E_F, E_F - 50 meV and E_F - 100 meV, respectively. While in Figure 6.12 (b) the surface BZ of Bi(0001) for the two different domains is shown (blue and green), Figure 6.12 (c) depicts the high-symmetry points of BTO(001). The electronic feature observed in Figure 6.11 can be assigned to the additional spectral weight in the constant energy maps in Figure 6.12 (b) and (c) (also indicated by black arrows). It appears, thereby, only at certain $\bar{\text{M}}$-points of Bi(0001) and even for both domains (here only shown for the blue domain). For that reason the electronic band does not originate solely from Bi(0001). It rather can be allocated to distinct high-symmetry points of the substrate, in particular, to the $\bar{\text{X}}$-point of BTO(001) (black arrows at Figure 6.12 (c)). However, such a electronic feature is not predicted for the

clean BTO(001) surface [184]; nor is it expected for the electronic structure on the surface of Bi(0001) [228] also by including strain [241]. As this electronic state only becomes visible in the PES experiment at the low coverage of 4 ML it is assumed that it originates from the interface and is induced by the coupling between overlayer and substrate. In contrast, increasing the Bi coverage prevents to probe the interface of Bi/BTO(001) due to a limited escape depth of the excited photoelectrons [225].

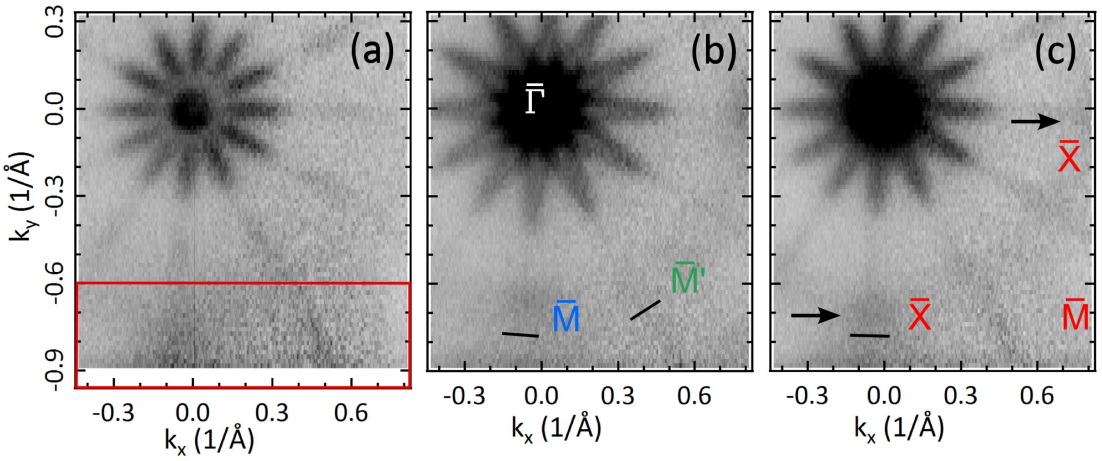

Figure 6.12: Position of the peculiar electronic band in k-space. CEM of 4 ML Bi/BTO(001) at E_F in (a), E_F - 50 meV in (b) and E_F - 100 meV in (c) measured at a temperature of 100 K. (b) The blue and green high-symmetry points correspond to the SBZ of Bi(0001) and (c) the red ones label the SBZ of BTO(001). At the $\bar{X}$-point of BTO additional spectral weight occurs (marked by the black arrows) which can be attributed to this electronic band. The red box is the area of interest in Figure 6.13.

This interface state is studied in more detail in close-up scans and band structure plots. In Figure 6.13 all the important properties of the interface state are displayed and summarized. On the one hand, the interface state is centered around the $\bar{X}$-point of BTO(001) as presented in the close-up scans at Figure 6.13 (a) - (c). The diameter of its paraboloid-like dispersion (in 3D) increases for higher E - E_F which prompts a hole character. In addition, it can be concluded that the top of the paraboloid lies above E_F due to a finite spectral weight at the Fermi map. The hole character of the interface state is further confirmed by cuts through the $\bar{X}$-point. The graphs at Figure 6.13 (d) and (e), thereby, represent the band structure of the raw data and the 2nd derivative plot along the $\bar{X} - \bar{M}$ direction, respectively. Both spectra have been extracted from the Fermi map along the red line (see Figure 6.13 (a)). Black and white dotted lines serve as a guide-to-the-eye and highlight the dispersion of the interface state. Additional cuts prove that the interface state exhibits an isotropic shape next to

its hole-like dispersion (not shown). This interface resembles the electronic state in a Al/BTO(001) heterostructure [196]. The ultrathin Aluminum (Al) toplayer reduces the BTO substrate and, thereby, generates 2D states at its surface. In addition, the defect state observed in Chapter 5 exhibits a similar dispersion but appears at the $\bar{\Gamma}$-points. In both cases the electronic state is attributed to the creation of OV at the surface.

The orbital character and the microscopic origin of the interface state in Bi/BTO, however, are still unclear. Its position in k-space suggests that it is derived from Ti $3d$ conduction band states which are located above E_F in the pure substrate [80]. Their occurrence in Bi/BTO might be explained by band bending (introduced in Subsection 2.1.6) which is induced by some kind of charge redistribution at the interface. Indeed, a small shifting (≈ 60 meV) of the core-levels and the valence band towards lower binding energies upon Bi deposition is observed. Figure 6.14 (b) and (c) depicts the valence band and the Ba $4d$ core-level of a pure BTO surface and of a Bi/BTO(001) system with a coverage of 2 ML and 1 ML, respectively. Similar results have been observed for the O $1s$ and the Ti $2p$ core-levels (not shown). The continuous shifting in energy of all these states confirms the band bending picture at the interface of Bi/BTO(001).

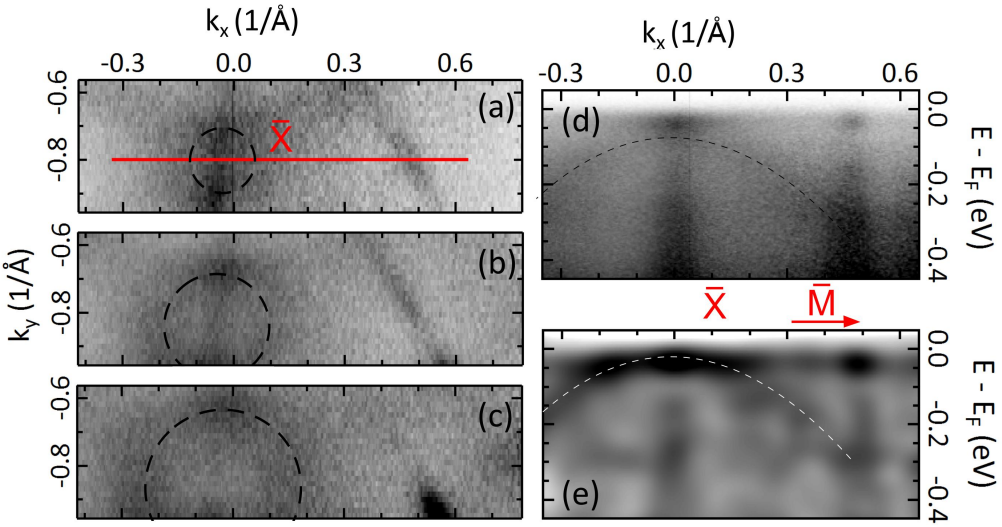

Figure 6.13: Interface state in Bi/BTO(001). (a) - (c) Close-up scans of the red box in Figure 6.12 (a) around the $\bar{X}$-point of BTO(001) for the different energies of E_F (a), E_F - 50 meV (b) and E_F - 100 meV (c). (d) - (e) Band structure and 2nd derivative plot along the red line shown in the Fermi map of (a). The dispersion of the interface state is emphasized by dotted lines in both graphs.

On the other hand, oxidation effects of the slightly more electronegative Bi can be excluded. This is shown at in Fig 6.14 (a) where the O $1s$ and Bi $4f$ core-levels do

not exhibit considerable spectral weight at their higher binding energy side (black circles), even by increasing the surface sensitivity in ARPES (higher take-off angle ϑ). In addition, the interface state can not be attributed to oxygen vacancies which would lead to a significant reduction of the surface. The Ti $2p_{3/2}$ core-level, however, is deficient in a strong Ti^{3+} contribution (blue box) [174]. In contrast, charge transfer at the interface of Bi/BTO(001) might induce the interface state. The accurate mechanism and microscopic origin which leads to the generation of the interface state in Bi/BTO(001) is still lacking.

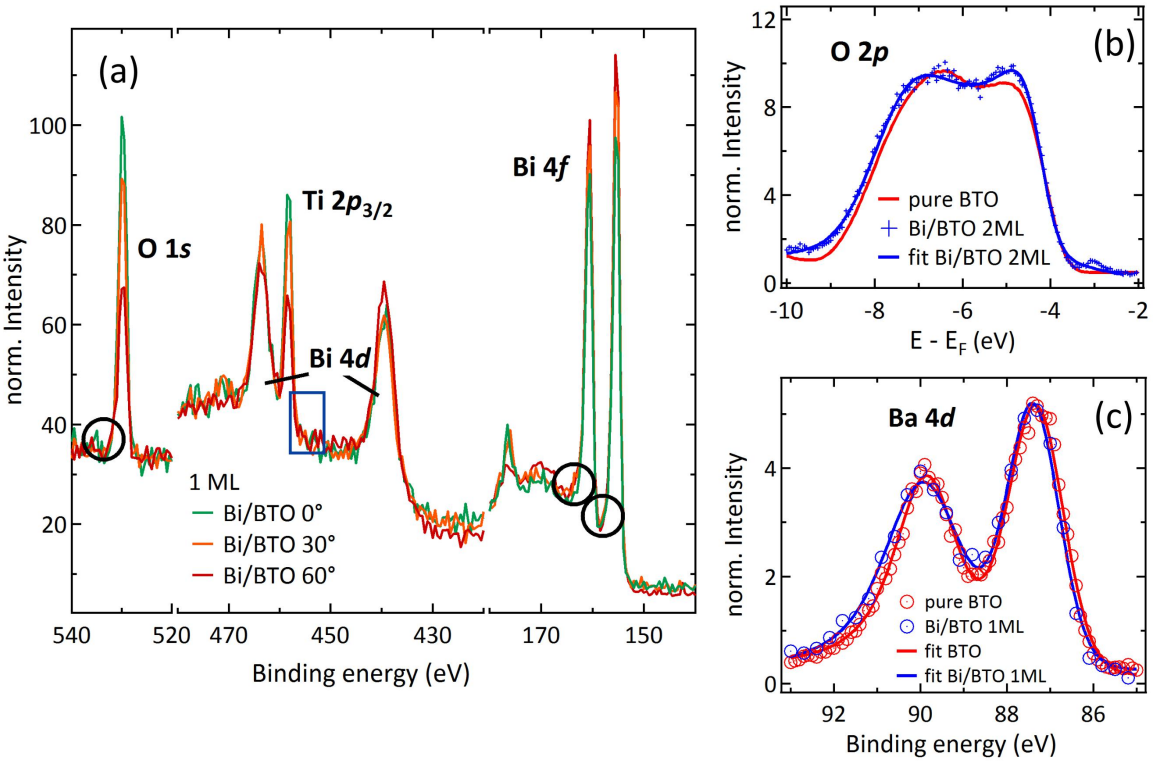

Figure 6.14: Origin of the interface state in Bi/BTO(001). (a) XPS spectra of Bi/BTO(001) with a coverage of 1 ML for different take-off angles $\vartheta = 0°$, 30° and 60°. No traces of oxidation become visible as the surface sensitivity (higher ϑ) in Bi/BTO(001) is increased. The black circles highlight the regions of interest. The valence band in (b) and the Ba 4*d* core-level in (c) consistently shift towards higher binding energies after the deposition of Bi on BTO. This is in line with band bending which results in a continuous energy shift for all electronic states. All spectra in (a - c) are normalized to the background intensity.

Theoretical calculation of the Bi/BTO(001) interface might solve this problem. The first-principle calculation of Bi on BTO(001), so far, describes the highly unrealistic

case of a commensurate interface structure [60, 242]. Therefore, a realistic theoretical modeling of the interface is required to reproduce the experimental electronic structure.

6.5 Outlook

Next to its interfacial state the ARPES data of Bi/BTO reveals large spin-split states at the surface. These states are located in the vicinity of a ferroelectric substrate which allows a possible manipulation of the Rashba-type spin-orbit states via ferroelectricity. The hybrid system Bi/BTO(001), hence, might be referred to some type of Rashba-ferroelectric heterostructure. For the Bi/BTO(001) system it has already been theoretically predicted that a switching of the ferroelectric polarization alters the spin-splitting of the surface states [60]. This calculation, however, only considers a single Bi layer on a BTO(001) substrate which leads to a marginal change in the spin-orbit splitting of 5 %.

Our ARPES experiments mainly have been performed at the low temperatures of $T = 60\,\mathrm{K}$ or 100 K. At these temperatures BTO is in the rhombohedral phase [103] and the ferroelectric polarization is directed along the [1 1 1] direction. As the lateral length scale for the ferroelectric domains in BTO is approximately in the order of $10 - 100\,\mu$m [163] PES experiments average over several different BTO domains. In addition, the PES spectra of Bi/BTO(001) contains signal of both Bi domains which are rotated by 90° with respect to each other. Due to these facts a possible change in the electronic structure of Bi/BTO by varying the ferroelectric polarization, *e.g.* by passing the structural phase transitions [103] could not be resolved in subsequent measurements.

Momentum-resolved photoemission electron microscopy (k-PEEM) measurements, however, enable to spatially resolve the electronic structure of Bi(0001) on different ferroelectric domains [243]. The use of an additional spin detector in this setup allows to get insight in the spin degree of freedom of the respective electronic state. Thus, a k-PEEM represents a powerful tool in order to study the impact of the ferroelectric polarization on the electronic properties of Bi-related states as *e.g.* spin-orbit coupling or other effects.

CHAPTER 7

CONCLUSION

Transition metal oxides (TMO) are a broadly studied class of materials due to the entanglement of spin, orbital and charge degrees of freedom on the microscopic level [67], and resulting collective phenomena such as superconductivity, magnetism, metallic 2DEG at the surface, etc. on the macroscopic level [19–23]. The consequent emergent phenomena are a result of correlation effects among the TMO-d electrons or of their hybridization with p electrons from the neighboring oxygen atoms [11]. In particular, the ferroelectricity in $BaTiO_3$ is proposed to arise from the p-d hybridization of conduction and valence band states [37, 72].

The hybridization strength in Ti $3d$ TMO, for instance, manifests itself in the satellite structure of the Ti $2p$ core-level spectra [88, 89]. In this thesis, the Ti $2p$ core-level spectrum of $BaTiO_3$ single crystals was studied by photoelectron spectroscopy and the satellite structure was qualitatively compared to the experimental and theoretical spectra of $SrTiO_3$ and TiO_2 [89]. The position of the satellite peaks suggest that $BaTiO_3$ exhibits a hybridization strength $pd\sigma$ which lies in between the values of $pd\sigma$ for TiO_2 and $SrTiO_3$. No crucial difference in the hybridization strength of $SrTiO_3$ and $BaTiO_3$ has been observed so that, solely on the basis of the core-level data, their distinct ferroelectric phase transition properties can not be explained [38, 74]. Nevertheless, the finding of the core-level spectra indicates a significant hybridization in both TMO which simultaneously is a prominent prerequisite for ferroelectricity, especially in the case of $BaTiO_3$ [37, 72].

Moreover, this thesis nicely displays the dispersion of the O $2p$ valence band by angle-resolved photoemission experiments carried out on $BaTiO_3$ single crystals. In a comprehensive analysis of the valence band structure, the O $2p$ spectra are in detail

compared to a band structure calculation whereby a good agreement is obtained [80]. Additional information about the hybridization strength in $BaTiO_3$ can be obtained by studying the density of states in the valence band. In general, p-d hybridization can be described by a charge transfer from the O sites to the Ti cation sites [71] and, hence, by a certain degree of covalency between the titanium and the oxygen atoms [181]. Therefore, photoelectron spectroscopy measurements on the O $2p$ valence band at photon energies below and above the Ti $3p \rightarrow 3d$ absorption edge [168] have been performed. The difference in spectral weight observed in both measurements reveals a finite Ti-O charge transfer in $BaTiO_3$, due to an increase of partial d density of states at the higher binding energy side of the O $2p$ valence band. This finding is in accordance to resonant photoemission experiments [168–170] and electronic structure calculations [179, 180]. In total, the core-level and the valence band photoemission experiments reveal that the one crucial requirement for ferroelectricity in the investigated $BaTiO_3$ bulk crystals is fulfilled due to a significant p-d hybridization [37, 72].

Ferroelectricity is not only prominent in single crystals but tends to persist in thin films [187]. However, it has been reported that the corresponding film thickness in $BaTiO_3$ considerably affects the critical transition temperature [214, 215, 244] and the properties of the ferroelectric domains [56]. Another restriction to the ferroelectric properties in $BaTiO_3$ is a critical electron concentration of $n \approx 10^{21}\,\mathrm{cm}^{-3}$ [155–157, 163, 245]. Similar to the observation in other Ti-based TMO, as *e.g.* $SrTiO_3$ [22, 23] and TiO_2(001) [24], $BaTiO_3$ is expected to display a 2DEG at the its surface. Indeed, signatures of metallic surface states have already been observed in bulk $BaTiO_3$(001) [185] and at the interface of Al/$BaTiO_3$(001) [196]. From these results, it might be anticipated that in a certain range of the electron concentration n, bulk ferroelectricity and surface conductivity coexist in $BaTiO_3$ single crystals and $BaTiO_3$ thin films.

Another part of the thesis, hence, is devoted to study the surface electronic structure of $BaTiO_3$(001) films depending on several parameters. The photoemission results support the occurrence of a 2DEG at the surface of $BaTiO_3$(001) also in the case of thin films. In addition, the formation of the 2DEG is clearly linked to the presence of oxygen defects by varying the partial oxygen pressure during the experiment. The oxygen vacancies induce a band bending at the surface and shift conduction band states below the Fermi level. The electronic states close to the Fermi level are assumed to be derived from Ti $3d$ states based on the photon energy and polarization dependence. However, our findings also show that the oxygen defects start to migrate from the surface into the bulk at the low onset temperatures of $T \approx 285\,\mathrm{K}$. Therefore, the 2DEG in $BaTiO_3$ is highly non-stable and volatile so that also the surface conductivity disappears at room temperature. This fact challenges the realization of room temperature application which are based on a conducting channel at the surface of $BaTiO_3$. A possible coupling of ferroelectricity to surface conductivity in $BaTiO_3$ at room temperature will probably

be even more difficult to accomplish.

Although, its long history in the field of solid state research, especially related to its ferroelectric behavior, $BaTiO_3$ has not been proposed to display magnetism (at bulk, surface, etc.). Recently, a surface ferromagnetism [217] has been suggested in $SrTiO_3$ which is a paraelectric structural isomorph of $BaTiO_3$. In this case, the ferromagnetism arises from a localized defect level in the band gap of $SrTiO_3$ [34] and the charge state of a localized electron at the lattice site of an oxygen vacancy can be associated to 1+. This fact is strongly correlated to the effective conductivity in bulk $SrTiO_3$ which scales with the partial oxygen pressure so that $\sigma \propto p_{O_2}^{-1/4}$ [97]. In the photoemission study on $BaTiO_3$ thin films performed in this thesis, however, a $p_{O_2}^{-1/6}$ scaling behavior of the measured spectral weight at the surface has been observed. The resulting charge state of 2+ for the oxygen vacancies excludes a local magnetic moment in $BaTiO_3$ thin films. Especially as no decoupled in-gap state could be detected in the photoemission experiment. Therefore, ferromagnetism and, in particular, its coupling to ferroelectricity is unlikely in pure $BaTiO_3$ thin films.

Proximity effects in the hybrid structures $Fe/BaTiO_3$, however, induce magnetoelectric coupling [51, 52]. There are further possibilities to manipulate physical properties via ferroelectricity, *e.g.* to control spin-polarized carriers by switching the electric polarization in $BaTiO_3$ [57]. The spin-orbit interaction is an essential physical property since it leads to a large variety of phenomena in the field of spintronics [63, 64]. Ferroelectricity might couple to the spin-orbit interaction and induce a breaking of inversion symmetry [63, 246]. A ferroelectric switching of the Rashba-type spin-orbit coupling has already been studied in $BaTiO_3$-based heterostructures [247] or in $Bi/BaTiO_3$ [60]. In the latter case, the Rashba splitting varies by 5 % considering a commensurable monolayer of Bi on $BaTiO_3$ [60].

The last part of this thesis addresses the interface electronic structure of the model system $Bi/BaTiO_3$. In the course of this study, the film growth of thin Bi layers on the $BaTiO_3$ single crystals has been realized and developed. The Bi films display a smooth and homogeneous surface but grow in two domains rotated by 90° with respect to each other. In the photoemission experiments, spin-split surface states of Bi are observed in the band gap of the ferroelectric $BaTiO_3$. In addition, it is demonstrated that the Bi film thickness affects the electronic properties of $Bi/BaTiO_3$. In the case of a rather high Bi film thickness ($\geq$ 10 monolayers), the electronic structure of the uppermost Bi layers adapt the one a theoretically semi-infinite Bi crystal [228] and resembles the band structure of Bi(0001) and Bi/Si(111). A decrease in the Bi film thickness is accompanied by a slight energy shift of the surface states and a minor change in the Fermi vector. At the low thickness of 4 ML, an additional interface state has been observed at the high-symmetry points of the substrate. This state resembles the electronic feature observed in $Al/BaTiO_3$ [196]. In general, these variations in

the electronic structure of Bi/$BaTiO_3$ can be attributed to an interaction between the Bi films and the $BaTiO_3$ substrate. Nevertheless, this coupling is rather too small in order to induce a change in the Rashba parameter of Bi. One possibility to enlarge the coupling in the Bi/$BaTiO_3$ system is either given by a different choice of substrate [241] or by enhancing the ferroelectricity of the $BaTiO_3$ substrate. In strained $BaTiO_3$ films, for instance, the remanent polarization increases by values up to 250 % [44].

The presented photoemission results may constitute a first step in the investigation of possible ferroelectric field effects on spin-orbit split electronic states. Furthermore, a basic understanding of the electronic structure at the interface of thin Bi films and the $BaTiO_3$ substrate is presented. However, there remain a lot of open questions which are directly related to the results of this thesis and which might be addressed to by other techniques. Transport and microscopic methods, for instance, can switch the ferroelectric polarization in $BaTiO_3$ which might result in a direct ferroelectric response in the electronic properties of Bi/$BaTiO_3$.

BIBLIOGRAPHY

[1] M. Asif Khan, A. Bhattarai, J. N. Kuznia, and D. T. Olson. "High electron mobility transistor based on a GaN-$Al_xGa_{1-x}N$ heterojunction". *Applied Physics Letters* **63** (1993), pp. 1214–1215.

[2] K. Von Klitzing. "The quantized Hall effect". *Reviews of Modern Physics* **58** (1986), p. 519.

[3] H. L. Stormer, D. C. Tsui, and A. C. Gossard. "The fractional quantum Hall effect". *Reviews of Modern Physics* **71** (1999), S298.

[4] R. Gaska, A. Osinsky, J. Yang, and M. S. Shur. "Self-heating in high-power AlGaN-GaN HFETs". *IEEE Electron Device Letters* **19** (1998), pp. 89–91.

[5] S. Aggarwal and R Ramesh. "Point defect chemistry of metal oxide heterostructures". *Annual Review of Materials Science* **28** (1998), pp. 463–499.

[6] S. Thiel, G. Hammerl, A Schmehl, C. Schneider, and J. Mannhart. "Tunable quasi-two-dimensional electron gases in oxide heterostructures". *Science* **313** (2006), pp. 1942–1945.

[7] J. Mannhart and D. G. Schlom. "Oxide interfaces—an opportunity for electronics". *Science* **327** (2010), pp. 1607–1611.

[8] P. Zubko, S. Gariglio, M. Gabay, P. Ghosez, and J.-M. Triscone. "Interface physics in complex oxide heterostructures". *Annu. Rev. Condens. Matter Phys.* **2** (2011), pp. 141–165.

[9] D. Xiao, W. Zhu, Y. Ran, N. Nagaosa, and S. Okamoto. "Interface engineering of quantum Hall effects in digital transition metal oxide heterostructures". *Nature Communications* **2** (2011).

[10] Y. Chen, N. Pryds, J. E. Kleibeuker, G. Koster, J. Sun, E. Stamate, B. Shen, G. Rijnders, and S. Linderoth. "Metallic and insulating interfaces of amorphous SrTiO3-based oxide heterostructures". *Nano Letters* **11** (2011), pp. 3774–3778.

[11] H. Y. Hwang, Y. Iwasa, M. Kawasaki, B. Keimer, N. Nagaosa, and Y. Tokura. "Emergent phenomena at oxide interfaces". *Nature Materials* **11** (2012), pp. 103–113.

[12] N. Tsuda, K. Nasu, A. Fujimori, and K. Siratori. *Electronic conduction in oxides*. Vol. 94. Springer Science & Business Media, 2013.

[13] K. Nomura, H. Ohta, A. Takagi, T. Kamiya, M. Hirano, and H. Hosono. "Room-temperature fabrication of transparent flexible thin-film transistors using amorphous oxide semiconductors". *Nature* **432** (2004), pp. 488–492.

[14] A. Ohtomo and H. Y. Hwang. "A high-mobility electron gas at the $LaAlO_3/SrTiO_3$ heterointerface". *Nature* **427** (2004), pp. 423–426.

[15] F. P. Netzer and A. Fortunelli. *Oxide Materials at the Two-Dimensional Limit*. Springer, 2016.

[16] A. Kalabukhov, R. Gunnarsson, J. Börjesson, E. Olsson, T. Claeson, and D. Winkler. "Effect of oxygen vacancies in the $SrTiO_3$ substrate on the electrical properties of the $LaAlO_3/SrTiO_3$ interface". *Physical Review B* **75** (2007), p. 121404.

[17] W. Siemons, G. Koster, H. Yamamoto, W. A. Harrison, G. Lucovsky, T. H. Geballe, D. H. A. Blank, and M. R. Beasley. "Origin of charge density at $LaAlO_3$ on $SrTiO_3$ heterointerfaces: possibility of intrinsic doping". *Physical Review Letters* **98** (2007), p. 196802.

[18] A. D. Caviglia, S. Gariglio, N. Reyren, D. Jaccard, T. Schneider, M. Gabay, S. Thiel, G. Hammerl, J. Mannhart, and J.-M. Triscone. "Electric field control of the $LaAlO_3/SrTiO_3$ interface ground state". *Nature* **456** (2008), pp. 624–627.

[19] N. Reyren, S. Thiel, A. D. Caviglia, L. F. Kourkoutis, G. Hammerl, C. Richter, C. W. Schneider, T. Kopp, A.-S. Rüetschi, D. Jaccard, M. Gabay, D. A. Muller, J.-M. Triscone, and J. Mannhart. "Superconducting interfaces between insulating oxides". *Science* **317** (2007), pp. 1196–1199.

[20] J. A. Bert, B. Kalisky, C. Bell, M. Kim, Y. Hikita, H. Y. Hwang, and K. A. Moler. "Direct imaging of the coexistence of ferromagnetism and superconductivity at the $LaAlO_3/SrTiO_3$ interface". *Nature Physics* **7** (2011), pp. 767–771.

[21] L. Li, C. Richter, J. Mannhart, and R. C. Ashoori. "Coexistence of magnetic order and two-dimensional superconductivity at $LaAlO_3/SrTiO_3$ interfaces". *Nature Physics* **7** (2011), pp. 762–766.

[22] W. Meevasana, P. D. C. King, R. H. He, S. K. Mo, M. Hashimoto, A. Tamai, P. Songsiriritthigul, F. Baumberger, and Z. X. Shen. "Creation and control of a two-dimensional electron liquid at the bare $SrTiO_3$ surface". *Nature Materials* **10** (2011), pp. 114–118.

[23] A. F. Santander-Syro, O. Copie, T. Kondo, F. Fortuna, S. Pailhes, R. Weht, X. G. Qiu, F. Bertran, A. Nicolaou, A. Taleb-Ibrahimi, P. Le Fèvre, G. Herranz, M. Bibes, N. Reyren, Y. Apertet, P. Lecoeur, A. Barthélémy, and M. J. Rozenberg. "Two-dimensional electron gas with universal subbands at the surface of $SrTiO_3$". *Nature* **469** (2011), pp. 189–193.

[24] S. Moser, L. Moreschini, J. Jaćimović, O. S. Barišić, H. Berger, A. Magrez, Y. J. Chang, K. Kim, A. Bostwick, E. Rotenberg, L. Forró, and M. Grioni. "Tunable polaronic conduction in anatase TiO_2". *Physical Review Letters* **110** (2013), p. 196403.

[25] P. D. C. King, R. H. He, T. Eknapakul, P. Buaphet, S.-K. Mo, Y. Kaneko, S. Harashima, Y. Hikita, M. S. Bahramy, C. Bell, Y. Hussain Z. Tokura, Z.-X. Shen, H. Y. Hwang, F. Baumberger, and W. Meevasana. "Subband structure of a two-dimensional electron gas formed at the polar surface of the strong spin-orbit perovskite $KTaO_3$". *Physical Review Letters* **108** (2012), p. 117602.

[26] A. F. Santander-Syro, C. Bareille, F. Fortuna, O. Copie, M. Gabay, F. Bertran, A. Taleb-Ibrahimi, P. Le Fèvre, G. Herranz, N. Reyren, M. Bibes, A. Barthélémy, P. Lecoeur, J. Guevara, and M. J. Rozenberg. "Orbital symmetry reconstruction and strong mass renormalization in the two-dimensional electron gas at the surface of $KTaO_3$". *Physical Review B* **86** (2012), p. 121107.

[27] P. D. C. King, S. M. Walker, A. Tamai, A. De La Torre, T. Eknapakul, P. Buaphet, S.-K. Mo, W. Meevasana, M. S. Bahramy, and F. Baumberger. "Quasiparticle dynamics and spin–orbital texture of the $SrTiO_3$ two-dimensional electron gas". *Nature Communications* **5** (2014).

[28] Y. Matsubara, K. S. Takahashi, M. S. Bahramy, Y. Kozuka, D. Maryenko, J. Falson, A. Tsukazaki, Y. Tokura, and M. Kawasaki. "Observation of the quantum Hall effect in δ-doped $SrTiO_3$". *Nature Communications* **7** (2016).

[29] Z. Wang, S. M. Walker, A. Tamai, Y. Wang, Z. Ristic, F. Y. Bruno, A. de la Torre, S. Riccò, N. C. Plumb, M. Shi, P. Hlawenka, J. Sánchez-Barriga, A. Varykhalov, T. K. Kim, M. Hoesch, P. D. C. King, W. Meevasana, U. Diebold, J. Mesot, B. Moritz, T. P. Devereaux, M. Radovic, and F. Baumberger. "Tailoring the nature

and strength of electron-phonon interactions in the $SrTiO_3$ (001) 2D electron liquid". *Nature Materials* (2016).

[30] F. Lechermann, H. O. Jeschke, A. J. Kim, S. Backes, and R. Valentí. "Electron dichotomy on the $SrTiO_3$ defect surface augmented by many-body effects". *Physical Review B* **93** (2016), p. 121103.

[31] M. Altmeyer, H. O. Jeschke, O. Hijano-Cubelos, C. Martins, F. Lechermann, K. Koepernik, A. F. Santander-Syro, M. J. Rozenberg, R. Valentí, and M. Gabay. "Magnetism, Spin Texture, and In-Gap States: Atomic Specialization at the Surface of Oxygen-Deficient $SrTiO_3$". *Physical Review Letters* **116** (2016), p. 157203.

[32] G. Herranz, M. Basletić, M. Bibes, C. Carrétéro, E. Tafra, E. Jacquet, K. Bouzehouane, C Deranlot, A. Hamzić, J.-M. Broto, A. Barthélémy, and A. Fert. "High mobility in $LaAlO_3/SrTiO_3$ heterostructures: origin, dimensionality, and perspectives". *Physical Review Letters* **98** (2007), p. 216803.

[33] A. Janotti, J. B. Varley, M. Choi, and C. G. Van de Walle. "Vacancies and small polarons in $SrTiO_3$". *Physical Review B* **90** (2014), p. 085202.

[34] C. Lin and A. A. Demkov. "Electron correlation in oxygen vacancy in $SrTiO_3$". *Physical Review Letters* **111** (2013), p. 217601.

[35] R. A. De Souza and M. Martin. "Using O^{18}/O^{16} exchange to probe an equilibrium space-charge layer at the surface of a crystalline oxide: method and application". *Physical Chemistry Chemical Physics* **10** (2008), pp. 2356–2367.

[36] R. A. De Souza, V. Metlenko, D. Park, and T. E. Weirich. "Behavior of oxygen vacancies in single-crystal $SrTiO_3$: equilibrium distribution and diffusion kinetics". *Physical Review B* **85** (2012), p. 174109.

[37] R. E. Cohen. "Origin of ferroelectricity in perovskite oxides". *Nature* **358** (1992), pp. 136–138.

[38] M. E. Lines and A. M. Glass. *Principles and applications of ferroelectrics and related materials*. Oxford university press, 1977.

[39] J. Fujioka, A. Doi, D. Okuyama, D. Morikawa, T. Arima, K. N. Okada, Y. Kaneko, T. Fukuda, H. Uchiyama, D. Ishikawa, K. Baron A. Q. R. Kato, M. Takata, and Y. Tokura. "Ferroelectric-like metallic state in electron doped $BaTiO_3$". *Scientific Reports* **5** (2015).

[40] T. Sluka, A. K. Tagantsev, P. Bednyakov, and N. Setter. "Free-electron gas at charged domain walls in insulating $BaTiO_3$". *Nature Communications* **4** (2013), p. 1808.

[41] D. G. Schlom, J. H. Haeni, J. Lettieri, C. D. Theis, W. Tian, J. C. Jiang, and X. Q. Pan. "Oxide nano-engineering using MBE". *Materials Science and Engineering: B* **87** (2001), pp. 282–291.

[42] C. H. Ahn, K. M. Rabe, and J.-M. Triscone. "Ferroelectricity at the nanoscale: local polarization in oxide thin films and heterostructures". *Science* **303** (2004), pp. 488–491.

[43] D. G. Schlom, L.-Q. Chen, C.-B. Eom, K. M. Rabe, S. K. Streiffer, and J.-M. Triscone. "Strain tuning of ferroelectric thin films". *Annu. Rev. Mater. Res.* **37** (2007), pp. 589–626.

[44] K. J. Choi, M. Biegalski, Y. L. Li, A. Sharan, J. Schubert, R. Uecker, P. Reiche, Y. B. Chen, X. Q. Pan, V. Gopalan, L.-Q. Chen, D. G. Schlom, and C. B. Eom. "Enhancement of ferroelectricity in strained $BaTiO_3$ thin films". *Science* **306** (2004), pp. 1005–1009.

[45] E. Y. Tsymbal and H. Kohlstedt. "Tunneling Across a Ferroelectric". *Science* **313** (2006), pp. 181–183.

[46] V. Garcia, S. Fusil, K. Bouzehouane, S. Enouz-Vedrenne, N. D. Mathur, A. Barthelemy, and M. Bibes. "Giant tunnel electroresistance for non-destructive readout of ferroelectric states". *Nature* **460** (2009), pp. 81–84.

[47] C. H. Ahn, J.-M. Triscone, N. Archibald, M. Decroux, R. H. Hammond, T. H. Geballe, Ø Fischer, and M. R. Beasley. "Ferroelectric field effect in epitaxial thin film oxide $SrCuO_2$/$Pb(Zr_{0.52}Ti_{0.48})O_3$ heterostructures". *Science* **269** (1995), p. 373.

[48] C. H. Ahn, A. Bhattacharya, M. Di Ventra, J. N. Eckstein, C. D. Frisbie, M. E. Gershenson, A. M. Goldman, I. H. Inoue, J. Mannhart, A. J. Millis, A. F. Morpurgo, D. Natelson, and J.-M. Triscone. "Electrostatic modification of novel materials". *Reviews of Modern Physics* **78** (2006), p. 1185.

[49] K. S. Takahashi, M. Gabay, D. Jaccard, K. Shibuya, T. Ohnishi, M. Lippmaa, and J.-M. Triscone. "Local switching of two-dimensional superconductivity using the ferroelectric field effect". *Nature* **441** (2006), pp. 195–198.

[50] P. Ponath, K. Fredrickson, A. B. Posadas, Y. Ren, X. Wu, R. K. Vasudevan, M. B. Okatan, S. Jesse, T. Aoki, M. R. McCartney, D. J. Smith, S. V. Kalinin, K. Lai, and A. A. Demkov. "Carrier density modulation in a germanium heterostructure by ferroelectric switching". *Nature Communications* **6** (2015).

[51] C.-G. Duan, S. S. Jaswal, and E. Y. Tsymbal. "Predicted magnetoelectric effect in Fe/$BaTiO_3$ multilayers: ferroelectric control of magnetism". *Physical Review Letters* **97** (2006), p. 047201.

[52] T. Cai, S. Ju, J. Lee, N. Sai, A. A. Demkov, Q. Niu, Z. Li, J. Shi, and E. Wang. "Magnetoelectric coupling and electric control of magnetization in ferromagnet/ferroelectric/normal-metal superlattices". *Physical Review B* **80** (2009), p. 140415.

[53] V. T. Tra, J.-W. Chen, P.-C. Huang, B.-C. Huang, Y. Cao, C.-H. Yeh, H.-J. Liu, E. A. Eliseev, A. N. Morozovska, J.-Y. Lin, Y.-C. Chen, M.-W. Chu, P.-W. Chiu, Y.-P. Chiu, L.-Q. Chen, C.-L. Wu, and Y.-H. Chu. "Ferroelectric control of the conduction at the $LaAlO_3$/$SrTiO_3$ heterointerface". *Advanced Materials* **25** (2013), pp. 3357–3364.

[54] A. Von Hippel. "Ferroelectricity, domain structure, and phase transitions of barium titanate". *Reviews of Modern Physics* **22** (1950), p. 221.

[55] G. Niu, S. Yin, G. Saint-Girons, B. Gautier, P. Lecoeur, V. Pillard, G. Hollinger, and B. Vilquin. "Epitaxy of $BaTiO_3$ thin film on Si (001) using a $SrTiO_3$ buffer layer for non-volatile memory application". *Microelectronic Engineering* **88** (2011), pp. 1232–1235.

[56] C. Dubourdieu, J. Bruley, T. M. Arruda, A. Posadas, J. Jordan-Sweet, M. M. Frank, E. Cartier, D. J. Frank, S. V. Kalinin, A. A. Demkov, and V. Narayanan. "Switching of ferroelectric polarization in epitaxial $BaTiO_3$ films on silicon without a conducting bottom electrode". *Nature Nanotechnology* **8** (2013), pp. 748–754.

[57] V. Garcia, M. Bibes, L. Bocher, S. Valencia, F. Kronast, A. Crassous, X. Moya, S. Enouz-Vedrenne, A. Gloter, D. Imhoff, C. Deranlot, N. D. Mathur, S. Fusil, K. Bouzehouane, and A. Barthélémy. "Ferroelectric control of spin polarization". *Science* **327** (2010), pp. 1106–1110.

[58] Y. A. Bychkov and E. I. Rashba. "Oscillatory effects and the magnetic susceptibility of carriers in inversion layers". *Journal of Physics C: Solid State Physics* **17** (1984), p. 6039.

[59] R. Winkler, S. J. Papadakis, E. P. De Poortere, and M. Shayegan. *Spin-Orbit Coupling in Two-Dimensional Electron and Hole Systems*. Vol. 41. Springer, 2003.

[60] H. Mirhosseini, I. V. Maznichenko, S. Abdelouahed, S. Ostanin, A. Ernst, I. Mertig, and J. Henk. "Toward a ferroelectric control of Rashba spin-orbit coupling: Bi on $BaTiO_3$ (001) from first principles". *Physical Review B* **81** (2010), p. 073406.

[61] D. Di Sante, P. Barone, R. Bertacco, and S. Picozzi. "Electric control of the giant Rashba effect in bulk GeTe". *Advanced Materials* **25** (2013), pp. 509–513.

[62] M. Kim, J. Im, A. J. Freeman, J. Ihm, and H. Jin. "Switchable S= 1/2 and J= 1/2 Rashba bands in ferroelectric halide perovskites". *Proceedings of the National Academy of Sciences* **111** (2014), pp. 6900–6904.

[63] A. Manchon, H. C. Koo, J. Nitta, S. M. Frolov, and R. A. Duine. "New perspectives for Rashba spin-orbit coupling". *Nature Materials* **14** (2015), pp. 871–882.

[64] A. Soumyanarayanan, N. Reyren, A. Fert, and C. Panagopoulos. "Emergent phenomena induced by spin–orbit coupling at surfaces and interfaces". *Nature* **539** (2016), pp. 509–517.

[65] S. Datta and B. Das. "Electronic analog of the electro-optic modulator". *Applied Physics Letters* **56** (1990), pp. 665–667.

[66] H. W. Eng, P. W. Barnes, B. M. Auer, and P. M. Woodward. "Investigations of the electronic structure of d^0 transition metal oxides belonging to the perovskite family". *Journal of Solid State Chemistry* **175** (2003), pp. 94–109.

[67] M. Imada, A. Fujimori, and Y. Tokura. "Metal-insulator transitions". *Reviews of Modern Physics* **70** (1998), p. 1039.

[68] Y. Tokura. *Colossal magnetoresistive oxides*. CRC Press, 2000.

[69] P. W. Anderson. "The Resonating Valence Bond State in La_2CuO_4 and Superconductivity". *Science* **235** (1987), pp. 1196–1198.

[70] Y. Tokura and N. Nagaosa. "Orbital physics in transition-metal oxides". *Science* **288** (2000), pp. 462–468.

[71] R. E. Cohen and H. Krakauer. “Lattice dynamics and origin of ferroelectricity in $BaTiO_3$: Linearized-augmented-plane-wave total-energy calculations”. *Physical Review B* **42** (1990), p. 6416.

[72] A. Filippetti and N. A. Hill. “Coexistence of magnetism and ferroelectricity in perovskites”. *Physical Review B* **65** (2002), p. 195120.

[73] I. B. Bersuker. *Electronic structure and properties of transition metal compounds: introduction to the theory*. John Wiley & Sons, 2010.

[74] I. B. Bersuker. “Recent development of the vibronic theory of ferroelectricity”. *Ferroelectrics* **164** (1995), pp. 75–100.

[75] K. M. Rabe, C. H. Ahn, and J.-M. Triscone. *Physics of ferroelectrics: a modern perspective*. Vol. 105. Springer Science & Business Media, 2007.

[76] L. F. Mattheiss. “Energy Bands for $KNiF_3$, $SrTiO_3$, $KMoO_3$, and $KTaO_3$”. *Physical Review B* **6** (1972), p. 4718.

[77] F. Bloch. “Über die Quantenmechanik der Elektronen in Kristallgittern”. *Zeitschrift für Physik* **52** (1929), pp. 555–600.

[78] J. C. Slater and G. F. Koster. “Simplified LCAO method for the periodic potential problem”. *Physical Review* **94** (1954), p. 1498.

[79] A. H. Kahn and A. J. Leyendecker. “Electronic energy bands in strontium titanate”. *Physical Review* **135** (1964), A1321.

[80] S. Piskunov, E. Heifets, R. I. Eglitis, and G. Borstel. “Bulk properties and electronic structure of $SrTiO_3$, $BaTiO_3$, $PbTiO_3$ perovskites: an ab initio HF/DFT study”. *Computational Materials Science* **29** (2004), pp. 165–178.

[81] D. I. Bilc, R. Orlando, R. Shaltaf, G.-M. Rignanese, J. Íñiguez, and P. Ghosez. “Hybrid exchange-correlation functional for accurate prediction of the electronic and structural properties of ferroelectric oxides”. *Physical Review B* **77** (2008), p. 165107.

[82] K. Van Benthem, C. Elsässer, and R. H. French. “Bulk electronic structure of $SrTiO_3$: Experiment and theory”. *Journal of Applied Physics* **90** (2001), pp. 6156–6164.

[83] D. Bagayoko, G. L. Zhao, J. D. Fan, and J. T. Wang. “Ab initio calculations of the electronic structure and optical properties of ferroelectric tetragonal”. *Journal of Physics: Condensed Matter* **10** (1998), p. 5645.

[84] J. Hubbard. “Electron correlations in narrow energy bands”. *Proceedings of the Royal Society of London A: Mathematical, Physical and Engineering Sciences*. Vol. 276. The Royal Society. 1963, pp. 238–257.

[85] J. Hubbard. “Electron correlations in narrow energy bands. III. An improved solution”. *Proceedings of the Royal Society of London A: Mathematical, Physical and Engineering Sciences*. Vol. 281. The Royal Society. 1964, pp. 401–419.

[86] T. Mizokawa and A. Fujimori. “Electronic structure and orbital ordering in perovskite-type 3d transition-metal oxides studied by Hartree-Fock band-structure calculations”. *Physical Review B* **54** (1996), p. 5368.

[87] J. Zaanen, G. A. Sawatzky, and J. W. Allen. “Band gaps and electronic structure of transition-metal compounds”. *Physical Review Letters* **55** (1985), p. 418.

[88] A. E. Bocquet, T. Mizokawa, T. Saitoh, H. Namatame, and A. Fujimori. “Electronic structure of 3d-transition-metal compounds by analysis of the 2p core-level photoemission spectra”. *Physical Review B* **46** (1992), p. 3771.

[89] A. E. Bocquet, T. Mizokawa, K. Morikawa, A. Fujimori, S. R. Barman, K. Maiti, D. D. Sarma, Y. Tokura, and M. Onoda. “Electronic structure of early 3d-transition-metal oxides by analysis of the 2p core-level photoemission spectra”. *Physical Review B* **53** (1996), p. 1161.

[90] P. W. Anderson. “Localized magnetic states in metals”. *Physical Review* **124** (1961), p. 41.

[91] C. Lin, C. Mitra, and A. A. Demkov. “Orbital ordering under reduced symmetry in transition metal perovskites: Oxygen vacancy in $SrTiO_3$”. *Physical Review B* **86** (2012), p. 161102.

[92] Y. Aiura, I. Hase, H. Bando, T. Yasue, T. Saitoh, and D. S. Dessau. “Photoemission study of the metallic state of lightly electron-doped $SrTiO_3$”. *Surface Science* **515** (2002), pp. 61–74.

[93] L. Dudy, M. Sing, P. Scheiderer, J. D. Denlinger, P. Schütz, J. Gabel, M. Buchwald, C. Schlueter, T.-L. Lee, and R. Claessen. “In Situ Control of Separate Electronic Phases on $SrTiO_3$ Surfaces by Oxygen Dosing”. *Advanced Materials* (2016).

[94] D. D. Cuong, B. Lee, K. M. Choi, H.-S. Ahn, S. Han, and J. Lee. “Oxygen vacancy clustering and electron localization in oxygen-deficient $SrTiO_3$: LDA+ U study”. *Physical Review Letters* **98** (2007), p. 115503.

[95] N. Bristowe, P. Littlewood, and E. Artacho. “Surface defects and conduction in polar oxide heterostructures”. *Physical Review B* **83** (2011), p. 205405.

[96] H. O. Jeschke, J. Shen, and R. Valentí. “Localized versus itinerant states created by multiple oxygen vacancies in $SrTiO_3$”. *New Journal of Physics* **17** (2015), p. 023034.

[97] R. A. De Souza, F. Gunkel, S. Hoffmann-Eifert, and R. Dittmann. “Finite-size versus interface-proximity effects in thin-film epitaxial $SrTiO_3$”. *Physical Review B* **89** (2014), p. 241401.

[98] G. Herranz, O. Copie, A. Gentils, E. Tafra, M. Basletić, F. Fortuna, K. Bouzehouane, S. Fusil, É. Jacquet, C. Carrétéro, M. Bibes, A. Hamzić, and A. Barthélémy. “Vacancy defect and carrier distributions in the high mobility electron gas formed at ion-irradiated $SrTiO_3$ surfaces”. *Journal of Applied Physics* **107** (2010), p. 103704.

[99] F. Gunkel, R. Waser, A. H. H. Ramadan, R. A. De Souza, S. Hoffmann-Eifert, and R. Dittmann. “Space charges and defect concentration profiles at complex oxide interfaces”. *Physical Review B* **93** (2016), p. 245431.

[100] B. Jalan, S. Stemmer, S. Mack, and S. J. Allen. “Two-dimensional electron gas in δ-doped $SrTiO_3$”. *Physical Review B* **82** (2010), p. 081103.

[101] G. Khalsa and A. H. MacDonald. “Theory of the $SrTiO_3$ surface state two-dimensional electron gas”. *Physical Review B* **86** (2012), p. 125121.

[102] I. B. Bersuker, N. N. Gorinchoi, and T. A. Fedorco. “Band structure and vibronic coupling related to ferroelectric properties of titanates of Ca, Sr and Ba”. *Ferroelectrics* **153** (1994), pp. 1–6.

[103] W. Zhong, D. Vanderbilt, and K. M. Rabe. “Phase Transitions in $BaTiO_3$ from First Principles”. *Physical Review Letters* **73** (1994), p. 1861.

[104] S. Miyake and R. Ueda. “On phase transformation of $BaTiO_3$”. *Journal of the Physical Society of Japan* **2** (1947), pp. 93–97.

[105] G. H. Kwei, A. C. Lawson, S. J. L. Billinge, and S. W. Cheong. “Structures of the ferroelectric phases of barium titanate”. *The Journal of Physical Chemistry* **97** (1993), pp. 2368–2377.

[106] T. Mitsui, S. Nomura, M. Adachi, J. Harada, T. Ikeda, E. Nakamura, E. Sawaguchi, T. Shigenari, Y. Shiozaki, I. Tatsuzaki, K. Toyoda, M. Adachi,

J. Harada, T. Shiosaki, K. Wakino, and T. Yamada. “Landolt-Börnstein Numerical Data and Functional Relationships in Science and Technology”. *Springer,* NS, III/**16** (1981).

[107] W. Cochran. “Crystal stability and the theory of ferroelectricity”. *Advances in Physics* **9** (1960), pp. 387–423.

[108] R. Comes, M. Lambert, and A. Guinier. “Désordre linéaire dans les cristaux (cas du silicium, du quartz, et des pérovskites ferroélectriques)”. *Acta Crystallographica Section A: Crystal Physics, Diffraction, Theoretical and General Crystallography* **26** (1970), pp. 244–254.

[109] B. Ravel, E. A. Stern, R. I. Vedrinskii, and V. Kraizman. “Local structure and the phase transitions of $BaTiO_3$”. *Ferroelectrics* **206** (1998), pp. 407–430.

[110] I. Levin, V. Krayzman, and J. C. Woicik. “Local structure in perovskite (Ba, Sr)TiO_3: Reverse Monte Carlo refinements from multiple measurement techniques”. *Physical Review B* **89** (2014), p. 024106.

[111] D. Hsieh, D. Qian, L. Wray, Y. Xia, Y. S. Hor, R. J. Cava, and M. Z. Hasan. “A topological Dirac insulator in a quantum spin Hall phase”. *Nature* **452** (2008), pp. 970–974.

[112] H. Zhang, C.-X. Liu, X.-L. Qi, X. Dai, Z. Fang, and S.-C. Zhang. “Topological insulators in Bi_2Se_3, Bi_2Te_3 and Sb_2Te_3 with a single Dirac cone on the surface”. *Nature Physics* **5** (2009), pp. 438–442.

[113] M. Z. Hasan and C. L. Kane. “Colloquium: topological insulators”. *Reviews of Modern Physics* **82** (2010), p. 3045.

[114] C. R. Ast, J. Henk, A. Ernst, L. Moreschini, M. C. Falub, D. Pacilé, P. Bruno, K. Kern, and M. Grioni. “Giant spin splitting through surface alloying”. *Physical Review Letters* **98** (2007), p. 186807.

[115] L. Moreschini, A. Bendounan, H. Bentmann, M. Assig, K. Kern, F. Reinert, J. Henk, C. R. Ast, and M. Grioni. “Influence of the substrate on the spin-orbit splitting in surface alloys on (111) noble-metal surfaces”. *Physical Review B* **80** (2009), p. 035438.

[116] H. Bentmann, T. Kuzumaki, G. Bihlmayer, S. Blügel, E. V. Chulkov, F. Reinert, and K. Sakamoto. “Spin orientation and sign of the Rashba splitting in Bi/Cu (111)”. *Physical Review B* **84** (2011), p. 115426.

[117] I. Gierz, T. Suzuki, E. Frantzeskakis, S. Pons, S. Ostanin, A. Ernst, J. Henk, M. Grioni, K. Kern, and C. R. Ast. "Silicon surface with giant spin splitting". *Physical Review Letters* **103** (2009), p. 046803.

[118] Y. A. Bychkov and E. I. Rashba. "Properties of a 2D electron gas with lifted spectral degeneracy". *JETP Lett.* **39** (1984), p. 78.

[119] C. E. Moore. *Atomic energy levels as derived from the analyses of optical spectra*. Vol. 1. US Dept. of Commerce, National Bureau of Standards, 1949.

[120] X. Gonze, J.-P. Michenaud, and J.-P. Vigneron. "First-principles study of As, Sb, and Bi electronic properties". *Physical Review B* **41** (1990), p. 11827.

[121] Y. Liu and R. E. Allen. "Electronic structure of the semimetals Bi and Sb". *Physical Review B* **52** (1995), p. 1566.

[122] P. Hofmann. "The surfaces of bismuth: Structural and electronic properties". *Progress in Surface Science* **81** (2006), pp. 191–245.

[123] H. Mönig, J. Sun, Y. M. Koroteev, G. Bihlmayer, J. Wells, E. V. Chulkov, K. Pohl, and P. Hofmann. "Structure of the (111) surface of bismuth: LEED analysis and first-principles calculations". *Physical Review B* **72** (2005), p. 085410.

[124] C. A. Hoffman, J. R. Meyer, F. J. Bartoli, A. Di Venere, X. J. Yi, C. L. Hou, H. C. Wang, J. B. Ketterson, and G. K. Wong. "Semimetal-to-semiconductor transition in bismuth thin films". *Physical Review B* **48** (1993), p. 11431.

[125] G. Jezequel, Y. Petroff, R. Pinchaux, and F. Yndurain. "Electronic structure of the Bi (111) surface". *Physical Review B* **33** (1986), p. 4352.

[126] F. Patthey, W.-D. Schneider, and H. Micklitz. "Photoemission study of the Bi (111) surface". *Physical Review B* **49** (1994), p. 11293.

[127] C. R. Ast and H. Höchst. "Fermi surface of Bi (111) measured by photoemission spectroscopy". *Physical Review Letters* **87** (2001), p. 177602.

[128] T. Hirahara, T. Nagao, I. Matsuda, G. Bihlmayer, E. V. Chulkov, Y. M. Koroteev, P. M. Echenique, M. Saito, and S. Hasegawa. "Role of spin-orbit coupling and hybridization effects in the electronic structure of ultrathin Bi films". *Physical Review Letters* **97** (2006), p. 146803.

[129] C. R. Ast and H. Höchst. "Two-dimensional band structure and self-energy of Bi (111) near the Γ point". *Physical Review B* **66** (2002), p. 125103.

[130] C. R. Ast and H. Höchst. “Electronic structure of a bismuth bilayer”. *Physical Review B* **67** (2003), p. 113102.

[131] T. Hirahara, I. Matsuda, S. Yamazaki, N. Miyata, S. Hasegawa, and T. Nagao. “Large surface-state conductivity in ultrathin Bi films”. *Applied Physics Letters* **91** (2007), pp. 202106–202106.

[132] Y. M. Koroteev, G. Bihlmayer, J. E. Gayone, E. V. Chulkov, S. Blügel, P. M. Echenique, and P. Hofmann. “Strong spin-orbit splitting on Bi surfaces”. *Physical Review Letters* **93** (2004), p. 046403.

[133] H. Hertz. “Ueber einen Einfluss des ultravioletten Lichtes auf die electrische Entladung”. *Annalen der Physik* **267** (1887), pp. 983–1000.

[134] A. Einstein. “Über einen die Erzeugung und Verwandlung des Lichtes betreffenden heuristischen Gesichtspunkt”. *Annalen der Physik* **322** (1905), pp. 132–148.

[135] S. Hüfner. *Photoelectron spectroscopy: principles and applications*. Springer Science & Business Media, 2013.

[136] A. Damascelli, Z. Hussain, and Z.-X. Shen. “Angle-resolved photoemission studies of the cuprate superconductors”. *Reviews of Modern Physics* **75** (2003), p. 473.

[137] K. Okada and A. Kotani. “Theory of core level X-ray photoemission and photoabsorption in Ti compounds”. *Journal of Electron Spectroscopy and Related Phenomena* **62** (1993), pp. 131–140.

[138] A. Fujimori, A. E. Bocquet, T. Saitoh, and T. Mizokawa. “Electronic structure of 3d transition metal compounds: systematic chemical trends and multiplet effects”. *Journal of Electron Spectroscopy and Related Phenomena* **62** (1993), pp. 141–152.

[139] F. M. F. De Groot, J. C. Fuggle, B. T. Thole, and G. A. Sawatzky. “L 2, 3 x-ray-absorption edges of d^0 compounds: K+, Ca 2+, Sc 3+, and Ti 4+ in O h (octahedral) symmetry”. *Physical Review B* **41** (1990), p. 928.

[140] K. E. Smith and V. E. Henrich. “Resonant photoemission in Ti_2O_3 and V_2O_3: Hybridization and localization of cation 3d orbitals”. *Physical Review B* **38** (1988), p. 9571.

[141] G. Berner, M. Sing, H. Fujiwara, A. Yasui, Y. Saitoh, A. Yamasaki, Y. Nishitani, A. Sekiyama, N. Pavlenko, T. Kopp, C. Richter, J. Mannhart, S. Suga, and R. Claessen. "Direct k-space mapping of the electronic structure in an oxide-oxide interface". *Physical Review Letters* **110** (2013), p. 247601.

[142] A. Damascelli. "Probing the electronic structure of complex systems by ARPES". *Physica Scripta* **2004** (2004), p. 61.

[143] C. N. Berglund and W. E. Spicer. "Photoemission studies of copper and silver: theory". *Physical Review* **136** (1964), A1030.

[144] C. N. Berglund and W. E. Spicer. "Photoemission studies of copper and silver: experiment". *Physical Review* **136** (1964), A1044.

[145] G. D. Mahan. "Excitons in metals: infinite hole mass". *Physical Review* **163** (1967), p. 612.

[146] P. J. Feibelman and D. E. Eastman. "Photoemission spectroscopy—correspondence between quantum theory and experimental phenomenology". *Physical Review B* **10** (1974), p. 4932.

[147] V. N. Strocov, H. I. Starnberg, P. O. Nilsson, H. E. Brauer, and L. J. Holleboom. "New method for absolute band structure determination by combining photoemission with very-low-energy electron diffraction: application to layered VSe_2". *Physical Review Letters* **79** (1997), p. 467.

[148] V. N. Strocov, R. Claessen, G. Nicolay, S. Hüfner, A. Kimura, A. Harasawa, S. Shin, A. Kakizaki, P. O. Nilsson, H. I. Starnberg, and P. Blaha. "Absolute band mapping by combined angle-dependent very-low-energy electron diffraction and photoemission: Application to Cu". *Physical Review Letters* **81** (1998), p. 4943.

[149] F. M. Michel-Calendini and G. Mesnard. "Band structure and optical properties of tetragonal BaTiO3". *Journal of Physics C: Solid State Physics* **6** (1973), p. 1709.

[150] Y. Haruyama, S. Kodaira, Y. Aiura, H. Bando, Y. Nishihara, T. Maruyama, Y. Sakisaka, and H. Kato. "Angle-resolved photoemission study of $SrTiO_3$ (100) and (110) surfaces". *Physical Review B* **53** (1996), p. 8032.

[151] M. P. Seah and W. A. Dench. "Quantitative electron spectroscopy of surfaces: a standard data base for electron inelastic mean free paths in solids". *Surface and Interface Analysis* **1** (1979), pp. 2–11.

[152] C. Mariani and G. Stefani. “Photoemission spectroscopy: fundamental aspects”. *Synchrotron Radiation*. Springer, 2015, pp. 275–317.

[153] R. Claessen. “Photoelectron spectroscopy: The joys and pitfalls of the photoelectric effect”. *Lecture Notes: School on UV and X-ray spectroscopies of correlated electron systems*. **SUCCESS-2014** (2014).

[154] S. Moser. “An experimentalist’s guide to the matrix element in angle resolved photoemission”. *Journal of Electron Spectroscopy and Related Phenomena* **214** (2017), p. 29.

[155] J. Hwang, T. Kolodiazhnyi, J. Yang, and M. Couillard. “Doping and temperature-dependent optical properties of oxygen-reduced $BaTiO_3$- δ”. *Physical Review B* **82** (2010), p. 214109.

[156] T. Kolodiazhnyi, M. Tachibana, H. Kawaji, J. Hwang, and E. Takayama-Muromachi. “Persistence of ferroelectricity in $BaTiO_3$ through the insulator-metal transition”. *Physical Review Letters* **104** (2010), p. 147602.

[157] Y. Wang, X. Liu, J. D. Burton, S. S. Jaswal, and E. Y. Tsymbal. “Ferroelectric instability under screened coulomb interactions”. *Physical Review Letters* **109** (2012), p. 247601.

[158] A. M. Kolpak, D. Li, R. Shao, A. M. Rappe, and D. A. Bonnell. “Evolution of the structure and thermodynamic stability of the $BaTiO_3$ (001) surface”. *Physical Review Letters* **101** (2008), p. 036102.

[159] H. L. Meyerheim, A. Ernst, K. Mohseni, I. V. Maznichenko, S. Ostanin, F. Klimenta, N. Jedrecy, W. Feng, I. Mertig, R. Felici, and J. Kirschner. “$BaTiO_3$ (001)-(2× 1): Surface Structure and Spin Density”. *Physical Review Letters* **108** (2012), p. 215502.

[160] J. M. P. Martirez, E. H. Morales, W. A. Saidi, D. A. Bonnell, and A. M. Rappe. “Atomic and Electronic Structure of the $BaTiO_3$ (001)(5× 5) R 26.6° Surface Reconstruction”. *Physical Review Letters* **109** (2012), p. 256802.

[161] P. Chen, Y. Xu, N. Wang, A. R. Oganov, and W. Duan. “Effects of ferroelectric polarization on surface phase diagram: Evolutionary algorithm study of the $BaTiO_3$ (001) surface”. *Physical Review B* **92** (2015), p. 085432.

[162] W. A. Saidi, J. M. P. Martirez, and A. M. Rappe. “Strong reciprocal interaction between polarization and surface stoichiometry in oxide ferroelectrics”. *Nano Letters* **14** (2014), pp. 6711–6717.

[163] J. E. Rault, J. Dionot, C. Mathieu, V. Feyer, C. M. Schneider, G. Geneste, and N. Barrett. "Polarization sensitive surface band structure of doped $BaTiO_3$ (001)". *Physical Review Letters* **111** (2013), p. 127602.

[164] Z. M. A. El-Fattah, P. Lutz, I. Piquero-Zulaica, J. Lobo-Checa, F. Schiller, H. Bentmann, J. E. Ortega, and F. Reinert. "Formation of the BiAg 2 surface alloy on lattice-mismatched interfaces". *Physical Review B* **94** (2016), p. 155447.

[165] X. Chen, S. Yang, J.-H. Kim, H.-D. Kim, J.-S. Kim, G. Rojas, R. Skomski, H. Lu, A. Bhattacharya, T. Santos, N. Guisinger, M. Bode, A. Gruverman, and A. Enders. "Ultrathin $BaTiO_3$ templates for multiferroic nanostructures". *New Journal of Physics* **13** (2011), p. 083037.

[166] F. L. Battye, H. Höchst, and A. Goldmann. "Photoelectron studies of the $BaTiO_3$ and $SrTiO_3$ valence states". *Solid State Communications* **19** (1976), pp. 269–271.

[167] R. Courths. "Ultraviolet photoelectron spectroscopy (UPS) and LEED studies of $BaTiO_3$ (001) and $SrTiO_3$ (100) surfaces". *physica status solidi (b)* **100** (1980), pp. 135–148.

[168] L. T. Hudson, R. L. Kurtz, S. W. Robey, D. Temple, and R. L. Stockbauer. "Photoelectron spectroscopic study of the valence and core-level electronic structure of $BaTiO_3$". *Physical Review B* **47** (1993), p. 1174.

[169] L. T. Hudson, R. L. Kurtz, S. W. Robey, D. Temple, and R. L. Stockbauer. "Surface core-level shifts of barium observed in photoemission of vacuum-fractured $BaTiO_3$ (100)". *Physical Review B* **47** (1993), p. 10832.

[170] S. W. Robey, L. T. Hudson, V. E. Henrich, C. Eylem, and B. Eichhorn. "Resonant photoelectron spectroscopy studies of $BaTiO_3$ and related mixed oxides". *Journal of Physics and Chemistry of Solids* **57** (1996), pp. 1385–1391.

[171] S. H. Wemple. "Polarization Fluctuations and the Optical-Absorption Edge in $BaTiO_3$". *Physical Review B* **2** (1970), p. 2679.

[172] M. Horn-von Hoegen. "Growth of semiconductor layers studied by spot profile analysing low energy electron diffraction-Part I". *Zeitschrift für Kristallographie* **214** (1999), pp. 591–629.

[173] D. Briggs and M. P. Seah. "Practical Surface Analysis by Auger and X-ray photoelectron spectroscopy". *D. Briggs, & M. P. Seah,(Editors), John Wiley & Sons, Chichester 1983, 533* (1983).

[174] M. Sing, G. Berner, K. Goß, A. Müller, A. Ruff, A. Wetscherek, S. Thiel, J. Mannhart, S. A. Pauli, C. W. Schneider, R. Willmott, M. Gorgoi, F. Schäfers, and R. Claessen. "Profiling the interface electron gas of $LaAlO_3/SrTiO_3$ heterostructures with hard X-ray photoelectron spectroscopy". *Physical Review Letters* **102** (2009), p. 176805.

[175] J. J. Yeh and I. Lindau. "Atomic subshell photoionization cross sections and asymmetry parameters: $1 \leq Z \leq 103$". *Atomic Data and Nuclear Data Tables* **32** (1985), pp. 1–155.

[176] F. Reinert and G. Nicolay. "Influence of the herringbone reconstruction on the surface electronic structure of Au (111)". *Applied Physics A: Materials Science & Processing* **78** (2004), pp. 817–821.

[177] F. L. Boariu. "The"Hidden-Order"phase transition of URu_2Si_2. Investigated by angle-resolved photoelectron spectroscopy". *PhD Thesis* (2014).

[178] M. Takizawa, K. Maekawa, H. Wadati, T. Yoshida, A. Fujimori, H. Kumigashira, and M. Oshima. "Angle-resolved photoemission study of Nb-doped $SrTiO_3$". *Physical Review B* **79** (2009), p. 113103.

[179] P. Pertosa, G. Hollinger, and F. M. Michel-Calendini. "Covalency effects in transition-metal perovskitelike compounds: Partial densities of p and d states and photoelectron valence-band spectra". *Physical Review B* **18** (1978), p. 5177.

[180] R. E. Cohen and H. Krakauer. "Electronic structure studies of the differences in ferroelectric behavior of $BaTiO_3$ and $PbTiO_3$". *Ferroelectrics* **136** (1992), pp. 65–83.

[181] S. Fatale, S. Moser, J. Miyawaki, Y. Harada, and M. Grioni. "Hybridization and electron-phonon coupling in ferroelectric $BaTiO_3$ probed by resonant inelastic x-ray scattering". *Physical Review B* **94** (2016), p. 195131.

[182] S. M. Walker, A. De La Torre, F. Y. Bruno, A. Tamai, T. K. Kim, M. Hoesch, M. Shi, M. S. Bahramy, P. D. C. King, and F. Baumberger. "Control of a Two-Dimensional Electron Gas on $SrTiO_3$ (111) by Atomic Oxygen". *Physical Review Letters* **113** (2014), p. 177601.

[183] J. Padilla and D. Vanderbilt. "Ab initio study of $BaTiO_3$ surfaces". *Physical Review B* **56** (1997), p. 1625.

[184] S. Piskunov, E. A. Kotomin, E. Heifets, J. Maier, R. I. Eglitis, and G. Borstel. "Hybrid DFT calculations of the atomic and electronic structure for ABO 3 perovskite (001) surfaces". *Surface Science* **575** (2005), pp. 75–88.

[185] Y. J. Chang. "Temperature-dependent Electronic Structure Change in Semiconducting $BaTiO_3$". *New Physics* **64** (2014), pp. 15–18.

[186] J. B. Torrance, P. Lacorre, C. Asavaroengchai, and R. M. Metzger. "Why are some oxides metallic, while most are insulating?" *Physica C: Superconductivity* **182** (1991), pp. 351–364.

[187] D. D. Fong, G. B. Stephenson, S. K. Streiffer, J. A. Eastman, O. Auciello, P. H. Fuoss, and C. Thompson. "Ferroelectricity in ultrathin perovskite films". *Science* **304** (2004), pp. 1650–1653.

[188] P. Lutz, S. Moser, V. Jovic, Y.-J. Chang, R. Koch, S. Ulstrup, J.-S. Oh, L. Moreschini, S. Fatale, M. Grioni, C. Jozwiak, A. Bostwick, E. Rotenberg, H. Bentmann, and F. Reinert, "Volatile 2D electron gas in ultra thin $BaTiO_3$ films", submitted for publication.

[189] A. Visinoiu, M. Alexe, H. N. Lee, D. N. Zakharov, A. Pignolet, D. Hesse, and U. Goesele. "Initial growth stages of epitaxial $BaTiO_3$ films on vicinal $SrTiO_3$ (001) substrate surfaces". *Journal of Applied Physics* **91** (2002), pp. 10157–10162.

[190] Y. S. Kim, D. H. Kim, J. D. Kim, Y. J. Chang, T. W. Noh, J. H. Kong, K. Char, Y. D. Park, S. D. Bu, J.-G. Yoon, and J.-S. Chung. "Critical thickness of ultrathin ferroelectric $BaTiO_3$ films". *Applied Physics Letters* **86** (2005), p. 102907.

[191] J. Shin, V. B. Nascimento, A. Y. Borisevich, E. W. Plummer, S. V. Kalinin, and A. P. Baddorf. "Polar distortion in ultrathin $BaTiO_3$ films studied by in situ LEED I- V". *Physical Review B* **77** (2008), p. 245437.

[192] C. Chen, J. Avila, E. Frantzeskakis, A. Levy, and M. C. Asensio. "Observation of a two-dimensional liquid of Frohlich polarons at the bare $SrTiO_3$ surface". *Nature Communications* **6** (2015).

[193] M. L. Knotek and P. J. Feibelman. "Ion desorption by core-hole Auger decay". *Physical Review Letters* **40** (1978), p. 964.

[194] M. Dauth, M. Graus, I. Schelter, M. Wießner, A. Schöll, F. Reinert, and S. Kümmel. "Perpendicular Emission, Dichroism, and Energy Dependence in

Angle-Resolved Photoemission: The Importance of The Final State". *Physical Review Letters* **117** (2016), p. 183001.

[195] N. C. Plumb, M. Salluzzo, E. Razzoli, M. Månsson, M. Falub, J. Krempasky, C. E. Matt, J. Chang, M. Schulte, J. Braun, H. Ebert, J. Minár, B. Delley, K.-J. Zhou, T. Schmitt, M. Shi, J. Mesot, L. Patthey, and M. Radović. "Mixed dimensionality of confined conducting electrons in the surface region of $SrTiO_3$". *Physical Review Letters* **113** (2014), p. 086801.

[196] T. C. Rödel, F. Fortuna, S. Sengupta, E. Frantzeskakis, P. L. Fèvre, F. Bertran, B. Mercey, S. Matzen, G. Agnus, T. Maroutian, P. Lecoeur, and A. F. Santander-Syro. "Universal Fabrication of 2D Electron Systems in Functional Oxides". *Advanced Materials* **28** (2016), pp. 1976–1980.

[197] F. De Groot, J. Fuggle, B. Thole, and G. Sawatzky. "2p x-ray absorption of 3d transition-metal compounds: An atomic multiplet description including the crystal field". *Physical Review B* **42** (1990), p. 5459.

[198] A. Chassé, S. Borek, K.-M. Schindler, M. Trautmann, M. Huth, F. Steudel, L. Makhova, J. Gräfe, and R. Denecke. "High-resolution x-ray absorption spectroscopy of $BaTiO_3$: Experiment and first-principles calculations". *Physical Review B* **84** (2011), p. 195135.

[199] J. Zhang, A. Visinoiu, F. Heyroth, F. Syrowatka, M. Alexe, D. Hesse, and H. S. Leipner. "High-resolution electron energy-loss spectroscopy of $BaTiO_3$/$SrTiO_3$ multilayers". *Physical Review B* **71** (2005), p. 064108.

[200] Y. Ishida, R. Eguchi, M. Matsunami, K. Horiba, M. Taguchi, A. Chainani, Y. Senba, H. Ohashi, H. Ohta, and S. Shin. "Coherent and incoherent excitations of electron-doped $SrTiO_3$". *Physical Review Letters* **100** (2008), p. 056401.

[201] Y. J. Chang, A. Bostwick, Y. S. Kim, K. Horn, and E. Rotenberg. "Structure and correlation effects in semiconducting $SrTiO_3$". *Physical Review B* **81** (2010), p. 235109.

[202] C. S. Fadley. "Photoelectron diffraction". *Physica Scripta* **1987** (1987), p. 39.

[203] T. Kolodiazhnyi. "Insulator-metal transition and anomalous sign reversal of the dominant charge carriers in perovskite $BaTiO_3$-δ". *Physical Review B* **78** (2008), p. 045107.

[204] P. Erhart and K. Albe. "Thermodynamics of mono-and di-vacancies in barium titanate". *Journal of Applied Physics* **102** (2007), p. 084111.

[205] M. Choi, F. Oba, and I. Tanaka. “Electronic and structural properties of the oxygen vacancy in $BaTiO_3$”. *Applied Physics Letters* **98** (2011), p. 172901.

[206] M. Kessel, R. A. De Souza, and M. Martin. “Oxygen diffusion in single crystal barium titanate”. *Physical Chemistry Chemical Physics* **17** (2015), pp. 12587–12597.

[207] T. Rödel, F. Fortuna, F. Bertran, M. Gabay, M. Rozenberg, A. Santander-Syro, and P. Le Fèvre. “Engineering two-dimensional electron gases at the (001) and (101) surfaces of TiO_2 anatase using light”. *Physical Review B* **92** (2015), p. 041106.

[208] F. Forster, A. Bendounan, J. Ziroff, and F. Reinert. “Systematic studies on surface modifications by ARUPS on Shockley-type surface states”. *Surface Science* **600** (2006), pp. 3870–3874.

[209] P. D. C. King, T. D. Veal, P. H. Jefferson, S. A. Hatfield, L. F. J. Piper, C. F. McConville, F. Fuchs, J. Furthmüller, F. Bechstedt, H. Lu, and W. J. Schaff. “Determination of the branch-point energy of InN: Chemical trends in common-cation and common-anion semiconductors”. *Physical Review B* **77** (2008), p. 045316.

[210] R. A. De Souza, C. Voisin, H. Schraknepper, M. Teusner, M. Kessel, P. Dufour, C. Tenailleau, and S. Guillemet-Fritsch. “Complex diffusion behavior of oxygen in nanocrystalline $BaTiO_3$ ceramics”. *Physical Chemistry Chemical Physics* **16** (2014), pp. 2568–2575.

[211] W. L. Warren, K. Vanheusden, D. Dimos, G. E. Pike, and B. A. Tuttle. “Oxygen vacancy motion in perovskite oxides”. *Journal of the American Ceramic Society* **79** (1996), pp. 536–538.

[212] J. A. Kilner and R. J. Brook. “A study of oxygen ion conductivity in doped non-stoichiometric oxides”. *Solid State Ionics* **6** (1982), pp. 237–252.

[213] P. Scheiber, M. Fidler, O. Dulub, M. Schmid, U. Diebold, W. Hou, U. Aschauer, and A. Selloni. “(Sub) Surface mobility of oxygen vacancies at the TiO_2 anatase (101) surface”. *Physical Review Letters* **109** (2012), p. 136103.

[214] N. Sai, A. M. Kolpak, and A. M. Rappe. “Ferroelectricity in ultrathin perovskite films”. *Physical Review B* **72** (2005), p. 020101.

[215] D. A. Tenne, P. Turner, J. D. Schmidt, M. Biegalski, Y. L. Li, L. Q. Chen, A. Soukiassian, S. Trolier-McKinstry, D. G. Schlom, X. X. Xi, D. D. Fong, P. H. Fuoss, J. A. Eastman, G. B. Stephenson, C. Thompson, and S. K. Streiffer.

"Ferroelectricity in ultrathin $BaTiO_3$ films: probing the size effect by ultraviolet Raman spectroscopy". *Physical Review Letters* **103** (2009), p. 177601.

[216] C. Lin and A. A. Demkov. "Consequences of oxygen-vacancy correlations at the $SrTiO_3$ interface". *Physical Review Letters* **113** (2014), p. 157602.

[217] T. Taniuchi, Y. Motoyui, K. Morozumi, T. C. Rödel, F. Fortuna, A. F. Santander-Syro, and S. Shin. "Imaging of room-temperature ferromagnetic nano-domains at the surface of a non-magnetic oxide". *Nature Communications* **7** (2016).

[218] P. Lutz, T. Figgemeier, Z. M. A. El-Fattah, H. Bentmann, and F. Reinert. "Large Spin Splitting and Interfacial States in a Bi/$BaTiO_3$(001) Rashba Ferroelectric Heterostructure". *Phys. Rev. Applied* **7** (4 2017), p. 044011.

[219] F. Sojka, M. Meissner, C. Zwick, R. Forker, and T. Fritz. "Determination and correction of distortions and systematic errors in low-energy electron diffraction". *Review of Scientific Instruments* **84** (2013), p. 015111.

[220] G. Jnawali, H. Hattab, B. Krenzer, and M. H. von Hoegen. "Lattice accommodation of epitaxial Bi (111) films on Si (001) studied with SPA-LEED and AFM". *Physical Review B* **74** (2006), p. 195340.

[221] C. Bobisch, A. Bannani, M. Matena, and R. Möller. "Ultrathin Bi films on Si (100)". *Nanotechnology* **18** (2007), p. 055606.

[222] J. A. Venables, G. D. T. Spiller, and M. Hanbucken. "Nucleation and growth of thin films". *Reports on Progress in Physics* **47** (1984), p. 399.

[223] J. Chastain, R. C. King, and J. F. Moulder. *Handbook of X-ray photoelectron spectroscopy: a reference book of standard spectra for identification and interpretation of XPS data*. Physical Electronics Eden Prairie, MN, 1995.

[224] C. D. Wagner, L. E. Davis, M. V. Zeller, J. A. Taylor, R. H. Raymond, and L. H. Gale. "Empirical atomic sensitivity factors for quantitative analysis by electron spectroscopy for chemical analysis". *Surface and Interface Analysis* **3** (1981), pp. 211–225.

[225] C. J. Powell and A. Jablonski. "NIST electron inelastic-mean-free-path database". *National Institute of Standarts and Technology, Gaithersburg* (2000).

[226] C. R. Ast and H. Höchst. "High-resolution photoemission mapping of the three-dimensional band structure of Bi (111)". *Physical Review B* **70** (2004), p. 245122.

[227] T. Hirahara, T. Nagao, I. Matsuda, G. Bihlmayer, E. V. Chulkov, Y. M. Koroteev, and S. Hasegawa. “Quantum well states in ultrathin Bi films: Angle-resolved photoemission spectroscopy and first-principles calculations study”. *Physical Review B* **75** (2007), p. 035422.

[228] Y. M. Koroteev, G. Bihlmayer, E. V. Chulkov, and S. Blügel. “First-principles investigation of structural and electronic properties of ultrathin Bi films”. *Physical Review B* **77** (2008), p. 045428.

[229] Here, the terminus “monolayer” (ML) is employed instead of “bilayer” in order to be consistent with the nomenclature used in the thesis so far. This definition is more unambiguous with respect to penetration depths and inelastic mean free paths (IMFP). In literature, however, a “bilayer” represents the buckled monolayer of Bi with its interlayer spacing.

[230] A. Kimura, E. E. Krasovskii, R. Nishimura, K. Miyamoto, T. Kadono, K. Kanomaru, E. V. Chulkov, G. Bihlmayer, K. Shimada, H. Namatame, and M. Taniguchi. “Strong Rashba-type spin polarization of the photocurrent from bulk continuum states: Experiment and theory for Bi (111)”. *Physical Review Letters* **105** (2010), p. 076804.

[231] T. Hirahara, K. Miyamoto, I. Matsuda, T. Kadono, A. Kimura, T. Nagao, G. Bihlmayer, E. V. Chulkov, S. Qiao, K. Shimada, H. Namatame, M. Taniguchi, and S. Hasegawa. “Direct observation of spin splitting in bismuth surface states”. *Physical Review B* **76** (2007), p. 153305.

[232] A. Takayama, T. Sato, S. Souma, and T. Takahashi. “Giant out-of-plane spin component and the asymmetry of spin polarization in surface Rashba states of bismuth thin film”. *Physical Review Letters* **106** (2011), p. 166401.

[233] Y. Ohtsubo, L. Perfetti, M. O. Goerbig, P. Le Fevre, F. Bertran, and A. Taleb-Ibrahimi. “Non-trivial surface-band dispersion on Bi (111)”. *New Journal of Physics* **15** (2013), p. 033041.

[234] S. Ito, B. Feng, M. Arita, A. Takayama, R.-Y. Liu, T. Someya, W.-C. Chen, T. Iimori, H. Namatame, M. Taniguchi, C.-M. Cheng, S.-J. Tang, F. Komori, K. Kobayashi, T.-C. Chiang, and I. Matsuda. “Proving nontrivial topology of pure bismuth by quantum confinement”. *Physical Review Letters* **117** (2016), p. 236402.

[235] V. B. Sandomirskii. “Quantum size effect in a semimetal film”. *Sov. Phys. JETP* **25** (1967), p. 101.

[236] T. Hirahara, T. Shirai, T. Hajiri, M. Matsunami, K. Tanaka, S. Kimura, S. Hasegawa, and K. Kobayashi. “Role of quantum and surface-state effects in the bulk fermi-level position of ultrathin Bi films”. *Physical Review Letters* **115** (2015), p. 106803.

[237] T. Nagao, J. T. Sadowski, M. Saito, S. Yaginuma, Y. Fujikawa, T. Kogure, T. Ohno, Y. Hasegawa, S. Hasegawa, and T. Sakurai. “Nanofilm Allotrope and Phase Transformation of Ultrathin Bi Film on Si (111)- 7×7”. *Physical Review Letters* **93** (2004), p. 105501.

[238] N. Garcia, Y. H. Kao, and M. Strongin. “Galvanomagnetic studies of bismuth films in the quantum-size-effect region”. *Physical Review B* **5** (1972), p. 2029.

[239] H. Asahi, T. Humoto, and A. Kawazu. “Quantum size effect in thin bismuth films”. *Physical Review B* **9** (1974), p. 3347.

[240] S. Murakami. “Quantum spin Hall effect and enhanced magnetic response by spin-orbit coupling”. *Physical Review Letters* **97** (2006), p. 236805.

[241] Z.-Q. Huang, F.-C. Chuang, C.-H. Hsu, Y.-T. Liu, H.-R. Chang, H. Lin, and A. Bansil. “Nontrivial topological electronic structures in a single Bi (111) bilayer on different substrates: A first-principles study”. *Physical Review B* **88** (2013), p. 165301.

[242] S. Abdelouahed and J. Henk. “Strong effect of substrate termination on Rashba spin-orbit splitting: Bi on $BaTiO_3$ (001) from first principles”. *Physical Review B* **82** (2010), p. 193411.

[243] C. Tusche, A. Krasyuk, and J. Kirschner. “Spin resolved bandstructure imaging with a high resolution momentum microscope”. *Ultramicroscopy* **159** (2015), pp. 520–529.

[244] J. Paul, T. Nishimatsu, Y. Kawazoe, and U. V. Waghmare. “Ferroelectric phase transitions in ultrathin films of $BaTiO_3$”. *Physical Review Letters* **99** (2007), p. 077601.

[245] Y. Iwazaki, T. Suzuki, Y. Mizuno, and S. Tsuneyuki. “Doping-induced phase transitions in ferroelectric $BaTiO_3$ from first-principles calculations”. *Physical Review B* **86** (2012), p. 214103.

[246] S. Picozzi. “Ferroelectric Rashba Semiconductors as a novel class of multifunctional materials”. *Frontiers in Physics* **2** (2014), p. 10.

[247] Z. Zhong, L. Si, Q. Zhang, W.-G. Yin, S. Yunoki, and K. Held. “Giant switchable Rashba effect in oxide heterostructures”. *Advanced Materials Interfaces* **2** (2015).

Publication list

- **P. Lutz**, S. Moser, V. Jovic, Y.-J. Chang, R. Koch, S. Ulstrup, J. S. Oh, L. Moreschini, S. Fatale, M. Grioni, C. Jozwiak, A. Bostwick, E. Rotenberg, H. Bentmann and F. Reinert. "Volatile 2D electron gas in ultra thin $BaTiO_3$ films." *submitted for publication*

- C.-H. Min, F. Goth, **P. Lutz**, H. Bentmann, B. Y. Kang, B. K. Cho, J. Werner, K.-S. Chen, F. Assaad and F. Reinert. "Matching DMFT calculations with photoemission spectra of heavy fermion insulators: universal properties of the near-gap spectra of SmB_6." *Sci. Rep.* **7** (2017), p. 11980.

- **P. Lutz**, T. Figgemeier, Z. M. Abd El-Fattah, H. Bentmann and F. Reinert. "Large Spin Splitting and Interfacial States in a Bi/$BaTiO_3$(001) Rashba Ferroelectric Heterostructure." *Phys. Rev. Applied* **7** (2017), p. 044011.

- K. Medjanik, O. Fedchenko, S. Chernov, D. Kutnyakhov, M. Ellguth, A. Oelsner, B. Schönhense, T. R. F. Peixoto, **P. Lutz**, C.-H. Min, F. Reinert, S. Däster, Y. Acremann, J. Viefhaus, W.Wurth, H. J. Elmers and G. Schönhense. "Direct 3D mapping of the Fermi surface and Fermi velocity." *Nat. Mater.* **16** (2017), p. 615.

- Z. M. Abd El-Fattah, **P. Lutz**, I. Piquero-Zulaica, J. Lobo-Checa, F. Schiller, H. Bentmann, J. E. Ortega and F. Reinert. "Formation of the $BiAg_2$ surface alloy on lattice-mismatched interfaces." *Phys. Rev. B* **94** (2016), p. 155447.

- **P. Lutz**, M. Thees, T. R. F. Peixoto, B. Y. Kang, B. K. Cho, C.-H. Min and F. Reinert. "Valence characterisation of the subsurface region in SmB_6." *Philos. Mag.* **96** (2016), p. 3307.

- H. Maaß, S. Schreyeck, S. Schatz, S. Fiedler, C. Seibel, **P. Lutz**, G. Karczewski, H. Bentmann, C. Gould, K. Brunner, L. W. Molenkamp and F. Reinert. "Electronic structure and morphology of epitaxial Bi_2Te_2Se topological insulator films." *J. Appl. Phys.* **116** (2014), p. 193708.

- C.-H. Min, **P. Lutz**, S. Fiedler, B. Y. Kang, B. K. Cho, H.-D. Kim, H. Bentmann and F. Reinert. “Importance of Charge Fluctuations for the Topological Phase in SmB_6.” *Phys. Rev. Lett.* **112** (2014), p. 226402.

- S. Fiedler, L. El-Kareh, S. V. Eremeev, O. E. Tereshchenko, C. Seibel, **P. Lutz**, K. A. Kokh, E. V. Chulkov, T. V. Kuznetsova, V. I. Grebennikov, H. Bentmann, M. Bode and F. Reinert. “Defect and structural imperfection effects on the electronic properties of BiTeI surfaces.” *New J. Phys.* **16** (2014), p. 075013.

- P. Olbrich, C. Zoth, **P. Lutz**, C. Drexler, V. V. Bel’kov, Ya V. Terent’ev, S. A. Tarasenko, A. N. Semenov, S. V. Ivanov, D. R. Yakovlev, T. Wojtowicz, U. Wurstbauer, D. Schuh and S. D. Ganichev. “Spin-polarized electric currents in diluted magnetic semiconductor heterostructures induced by terahertz and microwave radiation.” *Phys. Rev. B* **86** (2012), p. 085310.

- S. Stachel, P. Olbrich, C. Zoth, U. Hagner, T. Stangl, C. Karl, **P. Lutz**, V. V. Bel’kov, S. K. Clowes, T. Ashley, A. M. Gilbertson and S. D. Ganichev. “Interplay of spin and orbital magnetogyrotropic photogalvanic effects in InSb/(Al,In)Sb quantum well structures”. *Phys. Rev. B* **85** (2012), p. 045305.

- Ya V. Terent’ev, C. Zoth, V. V. Bel’kov, P. Olbrich, C. Drexler, V. Lechner, **P. Lutz**, M. S. Mukhin, S. A. Tarasenko, A. N. Semenov, V. A. Solov’ev, I. V. Sedova, G. V. Klimko, T. A. Komissarova, S. V. Ivanov and S. D. Ganichev. “Exchange interaction of electrons with Mn in hybrid AlSb/InAs/ZnMnTe structures.” *Appl. Phys. Lett.* **99** (2011), p. 072111.

Danksagung

Diese Dissertation, an sich, stellt zuerst einmal eine wissenschaftliche Arbeit dar, die sich in den Kontext anderer Arbeiten einreiht. Liest man jedoch zwischen den Zeilen, so ist sie viel mehr als nur ein Schriftstück, gespickt mit Messungen, Ergebnissen und Diskussionen. Sie ist ein Abbild meiner Zeit als Doktorand, mit den dazugehörigen Erlebnissen und Erfahrungen. Diese Zeit war, wie so vieles im Leben, geprägt von gewissen Höhen und Tiefen. Viele der dabei auftretenden Probleme hätte ich unmöglich alleine lösen können. Deshalb bin ich sehr dankbar für jeden, der mich im Laufe dieser Arbeit begleitet und mich ein gewisses Stück dabei unterstützt hat:

Allen voran möchte ich Prof. Friedrich Reinert (Friedel) danken, der all die erforderlichen logistischen Voraussetzungen für diese Doktorarbeit bereitgestellt hat. Zudem hat er mir, während meiner Arbeit, alle wissenschaftlichen Freiheiten eingeräumt und wo es nötig war, mich auch wieder auf die richtige Bahn zurückgeführt. Sein Vorschlag, an der Summer School in Les Houches teilzunehmen, hat mir in dem weiteren Verlauf meiner Dissertation enorm weitergeholfen; vor allem durch den dort erfahrenen wissenschaftlichen Austausch. An dieser Stelle möchte ich mich auch bei Dr. Olivier Copie bedanken. Er hat, zusammen mit Friedel, die Grundideen und Vorüberlegungen zu dieser Dissertation erarbeiteten. Mit seiner einschlägigen Erfahrung über Oxide konnte er mir, bei meinen anfänglichen Schwierigkeiten mit der Probenpräparation von Bariumtitanat, weiterhelfen. Da sich der Kontakt auf Email-Verkehr beschränkte konnte ich ihn bisher persönlich nie kennenlernen. Dieser fehlende Kontakt vor Ort wurde jedoch durch Dr. Mattia Mulazzi kompensiert. Er ist mir in der Anfangszeit oftmals helfend zur Seite gestanden. Vielen Dank auch dafür.

Ein großer Dank gebührt auch Dr. Hendrik Bentmann, der mich in die R4000-Kammer, wo ein Großteil meiner Arbeit entstand, eingelernt hat. Zudem hat er sich immer die Zeit genommen, um mit mir über meine Daten, Messergebnisse oder deren Interpretation zu diskutieren. Ein jedes dieser Treffen ließ mich wieder neuen Mut und Motivation für meine weitere Arbeit schöpfen. Gleichzeitig möchte ich mich bei Dr. Zakaria M. Abd El-Fattah bedanken, der mir bei der Charakterisierung und Präparation von Bismuthfilmen entscheidend weitergeholfen hat. Diese Unterstützung lieferte einen entscheidenden Beitrag an meinem wissenschaftlichen Output.

Ein weiterer großer Teil dieser Arbeit resultiert aus den Ergebnissen einer Messzeit am ALS (Berkeley) und der damit verbundenen Zusammenarbeit mit Dr. Simon Moser. Ich danke ihm, für sein Engagement und seine Mitarbeit bei der Vorbereitung, Durchführung und Nachbereitung dieser Messzeit. Dabei habe ich ihn auch als Person sehr zu schätzen gelernt. Außerdem halfen mir sein tieferes Verständnis für die verschiedenen Oxidsysteme und deren Eigenschaften in der Photoelektronenspektroskopie letztendlich bei der Auswertung und Interpretation meiner eigenen Daten. Ich danke auch der ganzen Gruppe um Dr. Eli Rotenberg am ALS (Berkeley), für die herzliche Aufnahme und Unterstützung vor Ort.

Weiterhin möchte ich mich bei Dr. Chul-Hee Min dafür bedanken, dass er mir durch meine Mitarbeit an seinem Forschungsthema eine neue Perspektive geschaffen hat. Von ihm habe ich auch vieles über wissenschaftliches Arbeiten gelernt, sei es die Datenauswertung mit Igor, das Schreiben von Messzeitanträgen oder die vielen aufschlussreichen Erfahrungen während der Messzeiten an sich. Diese enge Zusammenarbeit, vor allem bei den Messzeiten, hat dazu beigetragen, dass er mir während meiner Zeit in Würzburg ein guter Freund geworden ist.

Ich möchte mich auch bei all denjenigen gesondert bedanken, die mich in meiner oftmals frustrierenden Anfangszeit (in den ersten beiden Jahren) unterstützt haben. Zum einen bei Dr. Achim Schöll, der mich in seine Organikgruppe mitaufgenommen hat und in deren wöchentlichen Treffen ich die Schwierigkeiten und Fortschritte meiner Arbeit ansprechen konnte. Bei meinen damaligen Bürokollegen, Dr. Markus Scholz und Dr. Thanh-Nam Nguyen, die mir immer mit Rat und Tat zur Seite standen. Des Weiteren bei Sebastian Fiedler und bei Patrick Bayersdorfer, die mir als Laien, die Ultrahochvakuumtechnik und die Probenpräparation nähergebracht haben.

Ich danke auch meinen jetzigen Bürokollegen Martin Graus, Manuel Grimm und Christian Metzger für ein super Arbeitsklima innerhalb des Büros, Tim Figgemeier für die kollegiale und sehr angenehme Zusammenarbeit während seiner Bachelorarbeit, Max Ünzelmann und Henriette Maaß für die konstruktiven und hilfreichen Kritiken an meiner Dissertation, alle jetzigen und ehemaligen Kollegen der EP7 (ohne sie jetzt alle explizit zu nennen) für die unterhaltsame Zeit bei regelmäßigen außeruniversitären Aktivitäten, sowie generell allen Kollegen der EP7 und allen andern Mitarbeitern der Universität Würzburg, die mir das bestmögliche Umfeld und eine super Arbeitsatmosphäre für meine Doktorarbeit geschaffen haben.

Zuletzt möchte ich mich bei meiner Familie bedanken: Bei meinen Eltern Peter und Lidwina und bei meinen Schwestern Eva-Maria, Theresa und Anna-Lena, die mich bei meinen Entscheidungen immer unterstützt haben und auf deren Hilfe ich mich stets verlassen kann. Ganz besonders danke ich auch meiner Frau Sofia, die es immer wieder schafft, mich durch ihre lebhafte und liebenswerte Art mitzureißen, um mir dabei gleichzeitig ein Gefühl von Sicherheit und Rückhalt zu geben.